Investigating Finite Volume Time Domain Methods in Computational Electromagnetics

Vom Fachbereich Elektrotechnik und Informationstechnik
der Technischen Universität Darmstadt
zur Erlangung der Würde eines Doktor Ingenieurs (Dr.-Ing.)
genehmigte Dissertation von Chakrapani Bommaraju, M.Sc., aus Machilipatnam, Indien
September 2009 — Darmstadt — D 17

TECHNISCHE
UNIVERSITÄT
DARMSTADT

T E M F

Investigating Finite Volume Time Domain Methods in Computational Electromagnetics

Vom Fachbereich Elektrotechnik und Informationstechnik
der Technischen Universität Darmstadt
zur Erlangung der Würde eines Doktor Ingenieurs (Dr.-Ing.)
genehmigte Dissertation von Chakrapani Bommaraju, M.Sc., aus Machilipatnam, Indien

1. Referent : Prof. Dr.-Ing. Thomas Weiland
2. Korreferent: Prof. Dr. rer.nat. Karl-Jörg Langenberg

Tag der Einreichung: 07.07.2009
Tag der Prüfung : 25.09.2009

Darmstadt — D 17

Institut für Theorie Elektromagnetischer Felder
Fachbereich Elektrotechnik und Informationstechnik
Technische Universität Darmstadt

meiner Familie gewidmet

Abstract

In this work, the finite volume time domain semidiscrete formulation, discrete in the space and continuous in the time, is derived starting from the Maxwell's equations. This formulation is used to explain variations in finite volume time domain methods e.g., methods which differ in spatial approximation. The time marching schemes that can be employed to turn these semidiscrete formulations into discrete systems are presented.

For a given problem, numerical methods anticipate the convergence of the solutions towards the reference (analytical) solution as the grid is refined. But the convergence rate or order depends on the details of the computational domain. The convergence order for various finite volume time domain methods is presented in different scenarios e.g., a computational domain with curved surface and a singularity in the field due to the geometry.

It is a well known fact that the numerical solvers facilitate efficient design of passive microwave components by tendering the scattering parameters. Obtaining the scattering parameters using finite volume time methods is illustrated in this work along with the difficulties involved in the process. The solutions obtained for various applications e.g., a coaxial cable with a very high contrast of materials, are bidden against the solutions obtained from the finite integration technique and the finite element method.

The development cycle of a finite volume time domain solver is portrayed. Various modules are explained in detail along with assorted libraries employed in the solver. The computational cost, more specifically the floating point operations for various finite volume time domain methods are limned.

This work investigates the surmise of superior capabilities of finite volume time domain methods in the computational electromagnetics rigorously on both structured and unstructured grids.

Abstrakt

In dieser Arbeit wird eine Herleitung der semidiskreten Finite Volumen Methode im Zeitbereich – diskret im Raum und kontinuierlich in der Zeit – ausgehend von den Maxwell Gleichungen beschrieben. Diese Formulierung wird genutzt, um verschiedene Varianten von Finite Volumen Methoden im Zeitbereich, z.B. sich unterscheidende räumliche Approximationen, zu beschreiben. Es werden Zeitintegrationsverfahren untersucht, mit deren Hilfe die semidiskrete Formulierung in ein diskretes System überführt werden kann.

Für ein gegebenes Problem konvergiert die numerische Lösung für immer feinere Gitterschrittweiten gegen die exakte Referenzlösung. Jedoch hängt die Konvergenzordnung dabei von den Eigenschaften des Rechengebietes ab. In der Arbeit werden unterschiedliche Verfahren hinsichtlich ihrer Konvergenzordnung für verschiedene Probleme untersucht, z.B. für gekrümmte Oberflächen und einer Singularität im Feld.

Numerische Lösungsverfahren ermöglichen ein effizientes Design von passiven Mikrowellenkomponenten durch die Berechnung der Streuparameter. Wie die Streuparameter mittels Finiter Volumen Methoden im Zeitbereich berechnet werden können, sowie die dabei auftretenden Schwierigkeiten, wird in dieser Arbeit untersucht. Die dann berechneten Feldlösungen, z.B. ein Koaxialkabel bestehend aus unterschiedlichen Materialien, werden mit den Referenzlösungen verglichen, die mit Hilfe der Methode der Finiten Integration und der Methode der Finiten Elemente bestimmt worden sind.

Abschließend wird der Entwicklungszyklus eines Finiten Volumen Methode Lösers beschrieben. Die dabei nötigen verschiedenen Module und Bibliotheken werden eingehend erklärt. Der Rechenaufwand, insbesondere die Anzahl von Fließkommaoperationen, für verschiedene Finite Volumen Methoden wird angegeben.

In dieser Arbeit werden die mutmaßlich guten Eigenschaften von Finite Volumen Methode im Zeitbereich in “Computational Electromagnetics” untersucht – sowohl für strukturierte als auch für unstrukturierte Gitter.

Contents

1 Introduction

Computational electromagnetics gained its momentum ever since the Finite Element Method (FEM) [1] started being applied to solving the Maxwell's equations. Exploration of Yee's work [2] changed this scenario. The method proposed by Yee, later named as Finite Difference Time Domain (FDTD), got a huge following mainly due to its simplicity. It is written for the linear non–dispersive media and Cartesian grid. A few years later Weiland proposed [3] another volume discretization method, termed as Finite Integration Technique (FIT). FIT presents a closed theory, which can be applied to the full spectrum of electromagnetics. FIT on a Cartesian grid with appropriate choice of sampling points in the Time Domain (TD) is algebraically equivalent to FDTD. In other words, FIT is a more generalized form of FDTD.

All the above mentioned methods got refined and applied to various classes of problems [4–16] over the years and each of these methods enjoys its own set of advantages and disadvantages. FEM, more specifically, continuous FEM, has high flexibility in modeling the curved surfaces when employed on unstructured grids. But the TD formulation of the FEM results in a global implicit time marching scheme which requires global matrix inversion at each time step. This restricts FEM practically to Frequency Domain (FD) simulations. FD methods must solve an algebraic system of equations at all significant frequencies in the desired frequency range individually, making them more costly with increasing bandwidth. Fast frequency sweep algorithms can be employed in order to avoid calculating the solution at each and every frequency sample. However, these algorithms are memory intensive. When opted for parallel computing, FD methods require significant global operations.

For this reason numerical methods are cast in the TD for broadband simulations as they provide the desired broadband results in a single simulation run. FDTD and FIT are efficient for such analysis.To model the curved surfaces FIT uses conformal techniques e.g., "perfect boundary approximation". Unfortunately, this "conformality" comes at increased computational cost in the preprocessing stage.

The Discontinuous Galerkin FEM (DGFEM) [17] has also become another important numerical method in recent years. It provides a practical framework for the development of higher order accurate methods using structured or unstructured grids. The method is well suited for large scale TD computations in which high accuracy is required. An important distinction between the DGFEM and the continuous FEM is that in the case of the former the resulting equations are local to the generating element. In other words, the solution within each element is not reconstructed by looking at distant neighbors. Its compact formulation can be applied near boundaries without special treatment, which greatly increases the robustness and accuracy of any boundary condition implementation. However, DGFEM has more degrees of freedom and complexity than the same order continuous FEM, without any improvement in accuracy.

The need to simulate complicated physical interactions or geometries with an explicit time marching scheme that is at least second order accurate and not computationally intensive led to the development of Finite Volume Time Domain (FVTD) methods. Like the numerical methods mentioned above, FVTD methods are also grid based discretization methods; i.e., the computational domain is partitioned into subdomains to obtain the solutions to Maxwell's equations. FVTD is adopted by Shankar [18] from computational fluid dynamics. Shankar's scheme computes the flux on the grid cell interfaces and is the first scheme to use the characteristic principles in electromagnetics [19]. The use of characteristic principles in deriving numerical schemes for hyperbolic equations has been credited with sharply resolving discontinuities, reducing interference with physical diffusion, easier implementation of boundary conditions and, last but not least, lower phase speed errors [20–27].

FVTD methods combine the powerful attributes of the FEM (applicability on unstructured grids) with that of the FIT (accurate geometry modeling and explicit time update formulation). In addition, the FVTD method facilitates multi scaling in a natural way allowing very detailed modeling of electromagnetic structures [28–30]. Furthermore, the method also enables accurate modeling of structures with a high dielectric constant [31, 32] and curved geometries [33]. Recently, Sankaran [34–41] has formulated various absorbing boundary conditions for FVTD method. Numerous characteristics of Finite Volume Frequency Domain (FVFD) method were observed by Krohne [42–47]. The disadvantage of majority of FVTD methods can be attributed to artificial dissipation [48–50].

It would be difficult to compare the merits of the Cartesian grid schemes with those of the generalized grid schemes. Cartesian grid schemes are typically much less expensive than their general counterparts. To compare schemes one may have to weigh capability and complexity in addition to accuracy. Moreover, at present there is a growing consensus in the research community that second order schemes have insufficient accuracy and that higher order schemes are necessary. But as of yet little, if any, work has been published towards a higher order scheme on general grids with “greater accuracy per computational cost” than that of second order schemes. Several specialized methods have been developed to solve problems of varying nature and complexity [16]. In fact, no single method was found to be a perfect tool to handle all kinds of engineering problems. In many cases, the expertise of the user plays a crucial role in choosing the most appropriate method for a given problem [51].

Organization

In *Chapter 2*, *Fundamentals*, the finite volume time domain conceptualization is presented starting from the Maxwell’s equations. The semidiscrete formulation, discrete in the space and continuous in the time, is derived. This is followed by different variants of finite volume time domain formulation. The naming conventions used in this work are presented. After this, the boundary conditions are furnished. The time marching schemes that can be employed in order to turn these semidiscrete systems into fully discrete systems are portrayed. Casting these discrete systems in the global form i.e., the system matrix form is explained in detail. Later on the system matrix formulation is used to find the appropriate time marching scheme for a given finite volume method. Formulation of curl curl matrix and its applicability as an eigenmode solver is discussed. Impressing energy into the computation domain is explained, succeeded by the extraction of the scattering parameters.

The Lax equivalence theorem states that for a consistent numerical method with a well posed linear initial value problem, the method is convergent, if and only if, it is stable. This “convergent” property is examined in *Chapter 3*, *Convergence Analysis*. The convergence of the solutions obtained from various upwind flux finite volume time domain methods in different scenarios is presented and compared with the solutions from the finite integration technique and the finite element method.

Chapter 4, *Applications*, inspects the capabilities of finite volume time domain methods to model real world problems. Four applications are chosen e.g., a coaxial cable with a very high contrast of materials, to demonstrate the tractability of finite volume time domain methods. The results are bidden against the solutions obtained from the finite integration technique and the finite element method.

Chapter 5, *Implementation*, deals with the development of the finite volume time domain solver. Different modules of solver are furnished along with program flow at the concurrent stage. Various libraries used in the development are mentioned. The chapter notes the required floating point operations for several finite volume time domain methods.

In *Chapter 6*, *Conclusions*, the summary of work is presented.

2 Fundamentals

Abstract *– In this chapter, the finite volume time domain conceptualization is presented starting from the Maxwell's equations. The semidiscrete formulation, discrete in the space and continuous in the time, is derived. This is followed by different variants of finite volume time domain formulation. The naming conventions used in this work are presented. After this, the boundary conditions are furnished. The time marching schemes that can be employed in order to turn these semidiscrete systems into fully discrete systems are portrayed. Casting these discrete systems in the global form i.e., the system matrix form is explained in detail. Later on the system matrix formulation is used to find the appropriate time marching scheme for a given finite volume method. Formulation of curl curl matrix and its applicability as an eigenmode solver is discussed. Impressing energy into the computation domain is explained, succeeded by the extraction of the scattering parameters.*

2.1 Theory

The governing equations of electromagnetics can be written as [52]:

$$\nabla \times \vec{E} = -\frac{\partial \vec{B}}{\partial t} \tag{2.1}$$

$$\nabla \times \vec{H} = \frac{\partial \vec{D}}{\partial t} + \vec{J} \tag{2.2}$$

$$\nabla \cdot \vec{D} = \rho \tag{2.3}$$

$$\nabla \cdot \vec{B} = 0 \tag{2.4}$$

where $\vec{E}$, $\vec{H}$ represent the electric and magnetic field strengths; $\vec{D}$ and $\vec{B}$ represent the electric and magnetic flux densities; $\vec{J}$ and ρ represent the electric current density and the electric charge density, respectively. These equations are the mathematical representation of Faraday's law, Ampere's law, Gauss law, and Gauss law for magnetism. The relation between vector quantities $\vec{D}$, $\vec{E}$ and $\vec{B}$, $\vec{H}$ can be stated as follows [53]:

$$\vec{D} = \varepsilon \vec{E} + \vec{P} \tag{2.5}$$

$$\vec{B} = \mu \left(\vec{H} + \vec{M} \right) \tag{2.6}$$

where ε, μ, $\vec{P}$, $\vec{M}$ represent the permittivity, permeability, polarization and magnetization, respectively. For a homogeneous, isotropic, linear, non–dispersive, non–polarized and non–magnetized medium with no sources the governing equations can be simplified as:

$$\nabla \times \vec{E} = -\frac{\partial \vec{B}}{\partial t} \tag{2.7}$$

$$\nabla \times \vec{H} = \frac{\partial \vec{D}}{\partial t} \tag{2.8}$$

$$\nabla \cdot \vec{D} = 0 \tag{2.9}$$

$$\nabla \cdot \vec{B} = 0 \tag{2.10}$$

The constitutive equations which express the relation between the vector quantities in the above set of equations can be written as:

$$\vec{D} = \varepsilon \vec{E} \tag{2.11}$$

$$\vec{B} = \mu \vec{H} \tag{2.12}$$

Integrating the first two Maxwell's equations over a volume yields:

$$\int_V \left(\nabla \times \vec{E} \right) \mathrm{d}V = -\int_V \left(\frac{\partial \vec{B}}{\partial t} \right) \mathrm{d}V \tag{2.13}$$

$$\int_V \left(\nabla \times \vec{H} \right) \mathrm{d}V = +\int_V \left(\frac{\partial \vec{D}}{\partial t} \right) \mathrm{d}V \tag{2.14}$$

The curl theorem is invoked to convert the volume integrals of the vector fields into closed surface integrals. It relates the open volume integral of the curl of vector over a volume V to the closed surface integral of the vector over the surface S enclosing the volume V.

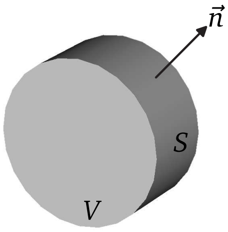

Figure 2.1: The curl theorem states that the integral of the curl of a vector field over a closed surface S is equal to the integral of this vector field throughout the volume V enclosed by the closed surface.

Applying the curl theorem [54], Equation 2.13 and Equation 2.14 can be written as:

$$\int_V \left(\frac{\partial \vec{D}}{\partial t} \right) \mathrm{d}V = +\oint_{\partial V} \left(\vec{n} \times \vec{H}^* \right) \mathrm{d}S \tag{2.15}$$

$$\int_V \left(\frac{\partial \vec{B}}{\partial t} \right) \mathrm{d}V = -\oint_{\partial V} \left(\vec{n} \times \vec{E}^* \right) \mathrm{d}S \tag{2.16}$$

where $\vec{E}^*$, $\vec{H}^*$, $\vec{n}$, $\mathrm{d}S$, and $\mathrm{d}V$ represent the boundary limits of electric and magnetic fields, normal vector to the surface, differential surface area and differential volume, respectively. As the permittivity and permeability are constant, one can write:

$$\frac{\partial \bar{E}}{\partial t} = +\left(\frac{1}{\varepsilon V} \right) \oint_{\partial V} \left(\vec{n} \times \vec{H}^* \right) dS \tag{2.17}$$

$$\frac{\partial \bar{H}}{\partial t} = -\left(\frac{1}{\mu V} \right) \oint_{\partial V} \left(\vec{n} \times \vec{E}^* \right) dS \tag{2.18}$$

where $\bar{E}$ and $\bar{H}$ represent the volume averaged fields as shown below:

$$\bar{E} = \frac{1}{V} \int_V \vec{E} \, dV \tag{2.19}$$

$$\bar{H} = \frac{1}{V} \int_V \vec{H} \, dV \tag{2.20}$$

Equation 2.17 and Equation 2.18 can be expressed as:

$$\frac{\partial U}{\partial t} = -\left(\frac{1}{V}\right) \oint_{\partial V} A(\vec{n}) \cdot U^* dS \tag{2.21}$$

where

$$\begin{aligned} U &= \frac{1}{V}\left(E_x\ E_y\ E_z\ H_x\ H_y\ H_z\right)' &(2.22)\\ U^* &= \left(E_x^*\ E_y^*\ E_z^*\ H_x^*\ H_y^*\ H_z^*\right)' &(2.23)\end{aligned}$$

The explicit form of matrix $A(\vec{n})$ is furnished in Appendix 1. The term $A(\vec{n}) \cdot U^*$ is coined as the "flux" at the center of the surface (explained in Section 2.3.2). The matrix $A(\vec{n})$ can be decomposed as:

$$\begin{aligned} A(\vec{n}) &= p\Lambda p^{-1} &(2.24)\\ &= p\left(\Lambda^+ + \Lambda^-\right)p^{-1} &(2.25)\\ &= p\Lambda^+ p^{-1} + p\Lambda^- p^{-1} &(2.26)\\ &= A^+(\vec{n}) + A^-(\vec{n}) &(2.27)\end{aligned}$$

The diagonal matrix formed by all the eigenvalues of the matrix $A(\vec{n})$ is represented as Λ whereas Λ^+ and Λ^- represent the diagonal matrices formed by the positive and negative eigenvalues of $A(\vec{n})$. The empirical form of matrices Λ and p are also given in Appendix 1. With these modifications, Equation 2.21 can be represented as:

$$\frac{\partial U}{\partial t} = -\left(\frac{1}{V}\right) \oint_{\partial V} \left(A^+(\vec{n}) + A^-(\vec{n})\right) \cdot U^* dS \tag{2.28}$$

Equation 2.21 and Equation 2.28 represent two different classes of finite volume systems, identified as central flux finite volume system and upwind flux finite volume system. These are explained in detail in the Section 2.3.2. In upwind flux finite volume system, the net flux density $(A(\vec{n}) \cdot U^*)$ is decomposed into outgoing $\left(A^+(\vec{n}) \cdot U^*\right)$ and incoming $\left(A^-(\vec{n}) \cdot U^*\right)$ flux densities. The relation between $A^+(\vec{n})$ and $A^-(\vec{n})$ can be stated as [6]:

$$A^-(\vec{n}) = -A^+(-\vec{n}) \tag{2.29}$$

2.2 Discretization

Consider a computational domain discretized into elementary volumes (cells), as shown in Figure 2.2(a) or Figure 2.2(b). In such a domain consider a cell identified by index i. Let the volume of this cell be v_i. This cell consists of m_i faces. Each of these m_i faces is represented as f_{ki}, where $k \in \{1, m_i\}$. If m_i equals 4 the unit cell is a tetrahedron and if m_i equals 6 the unit cell is a hexahedron. The area of each of these faces is represented as s_{ki}. The outward unit normal to each of these is represented as $\vec{n}_{ki}$. The field values in the cell center, $\left(x_i, y_i, z_i\right)$, be represented as u_i and the field values in the face centers, $\left(x_{ki}, y_{ki}, z_{ki}\right)$, be represented as u_{ki}. Let the permittivity and permeability of the material in this cell be constant and represented as ε_i and μ_i, respectively. The impedance and admittance of a plane wave in this cell are represented as η_i and y_i.

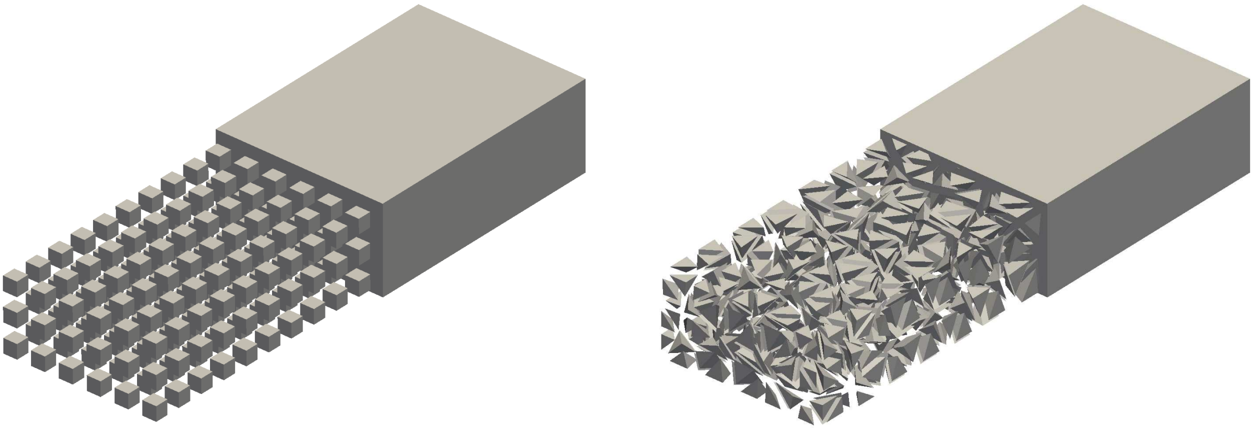

(a) Hexahedral mesh (b) Tetrahedral mesh

Figure 2.2: A computational domain partially discretized with hexahedral and tetrahedral meshes. The elementary volumes are shown only in the discretized portion of the domain. In this portion, the cells are shrunk for better visibility.

Let cell j be a neighbor to cell i. In other words, these two cells share a face, namely, f_{ki} or f_{lj}. The outward unit normal to this face (f_{ki}) becomes the inward unit normal of the face (f_{lj}). Figure 2.3(a) and Figure 2.3(b) depict the scenario.

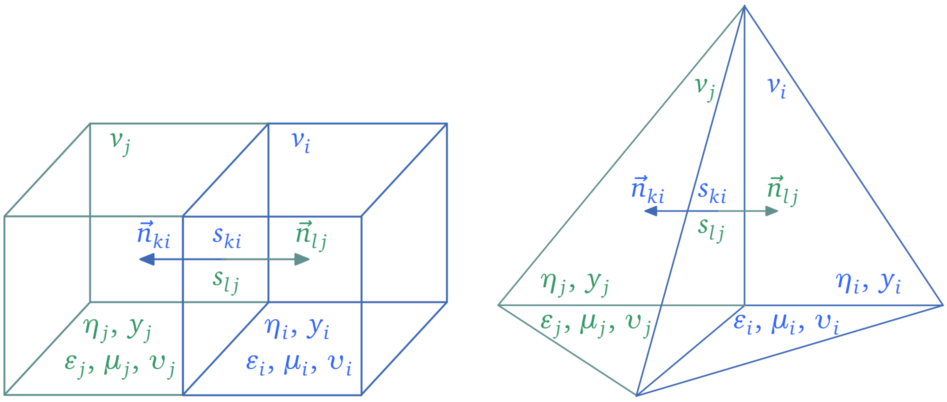

(a) Hexahedral mesh (b) Tetrahedral mesh

Figure 2.3: A reference cell along with its neighbor, with various geometric and physical parameters in each cell, in hexahedral and tetrahedral meshes.

2.3 Variations

Finite volume formulations can be broadly classified into three categories, namely, based on the location of field components, based on the flux approximation and based on the time marching schemes [6].

2.3.1 Location of Field Components

Based on the location of field components, finite volume formulations can be subdivided into cell center formulation, cell vertex formulation and cell staggered formulation.

2.3.1.1 Cell Center

In cell center formulation, the degrees of freedom are associated with barycenters of cells. A finite volume is formed by connecting the nodes of the cells. Figure 2.4(a) depicts the location of degrees of freedom in the cell center formulation. The boundary conditions are taken into account more naturally here.

2.3.1.2 Cell Vertex

In cell vertex formulation, the degrees of freedom are associated with nodes of cells. The finite volume is defined by connecting the barycenters of cells to which the node belongs, as shown in Figure 2.4(b). The extension to higher spatial orders is easier in this formulation.

2.3.1.3 Cell Staggered

As in FDTD, the field components are staggered [55] here. This formulation can be further classified as E–staggered and H–staggered [47]. In the case of E–staggered formulation, depicted in Figure 2.4(c), the electric field components are located at the face centers of cells and magnetic field components are at the barycenters of the cells. For H–staggered formulation the location of field components is interchanged. This is presented in Figure 2.4(d).

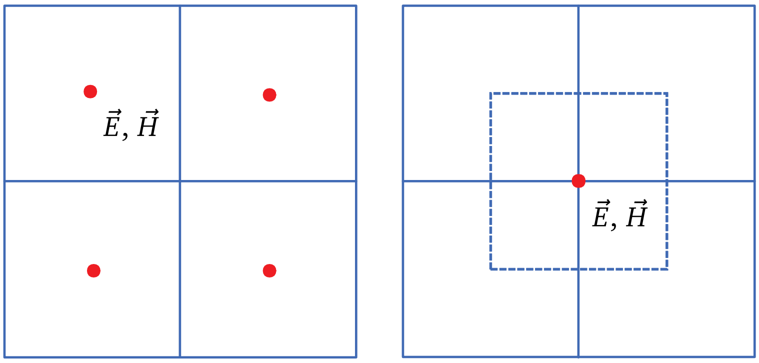

(a) Cell center (b) Cell vertex

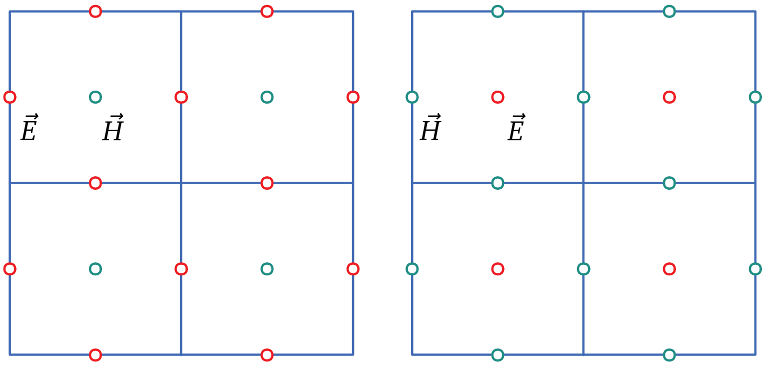

(c) E-staggered (d) H-staggered

Figure 2.4: Location of degrees of freedom in various finite volume formulations in a computational domain discretized with hexahedral mesh, 2D view.

2.3.2 Flux Approximation

Flux can be defined as the integral of a vector quantity over a finite surface. Mathematically one can express the same as:

$$\phi = \oint_S \vec{A} \cdot d\vec{S} = \oint_S \left(\vec{A} \cdot \vec{n}\right) dS \tag{2.30}$$

where ϕ, $\vec{A}$ and $\vec{n}$ represent the flux, the vector quantity and the unit outward normal to the surface. One can observe that the flux has contributions from normal components only.

The R.H.S. of Equation 2.21 and Equation 2.28 resemble to the above equation and so termed as “flux”, following the conventions. To be more precise “flux” should be coined “numerical flux” because of the presence of the tangential field components (curl of field quantities, mentioned in Equation 2.17 and Equation 2.18, yields tangential field components).

In Equation 2.21 and Equation 2.28, there are two sets of unknowns, namely, the field values at the barycenter of the cells and the field values on the cell interfaces. The relation between the field values in the cell centers and the limiting values on cell boundaries forms the basis for flux approximation.

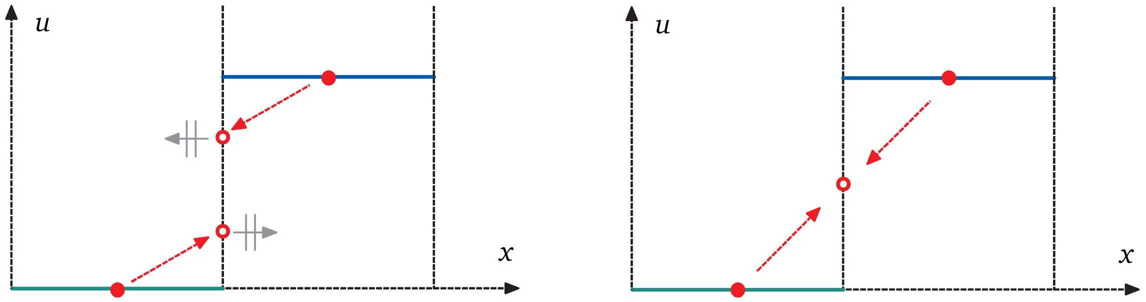

(a) Upwind flux (b) Central flux

Figure 2.5: Variations in flux approximation in 1D. Two cells are depicted, in blue and green, along with barycenter field values, denoted by filled red circles. The field values on the cell interfaces, red circle(s), can be obtained either by averaging or upwinding. These field values are used to establish flux approximation. In upwind flux formulation the fields move in either direction through cell interface.

For more clarity consider a 1D computational domain aligned to the x axis, as depicted in Figure 2.5. Two cells are depicted, one in green color and the other in blue color. The field values in each cell are depicted by filled red circles. The procedure of obtaining the field values on cell interfaces from the discontinuous field values on either side of the interface involves either averaging or upwinding as shown [24, 48, 49, 55, 56]. In upwind flux formulation the fields move in either direction through the cell interfaces, owing to the non–zero eigenvalues ($\pm v$) of matrix $A(\vec{n})$. On the other hand, the central flux formulation is based on the zero eigenvalues of the matrix $A(\vec{n})$. Finite volume formulations that differ in the way the fluxes are computed fall under this category.

2.3.2.1 Upwind Flux

The upwind fluxes can be computed by piecewise constant interpolation or piecewise linear interpolation of barycenter field values. In piecewise constant interpolation the face center values are the same as the barycenter field values.

$$u_{ki}^{-} = u_i \tag{2.31}$$

$$u_{ki}^{+} = u_j \tag{2.32}$$

For any given cell, for each of the faces, the field value inside the face is equal to the barycenter field value of that cell, and the field value outside the face is equal to the barycenter field value of the corresponding neighbor. This is depicted in Figure 2.6.

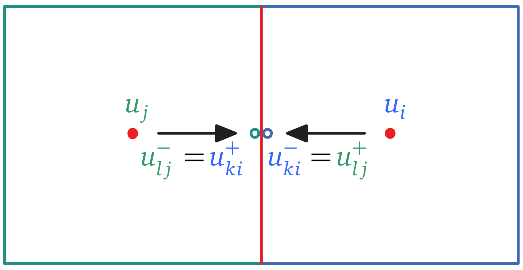

Figure 2.6: Piecewise constant interpolation of barycenter field values to obtain the face center values for a non-boundary cell, in a domain discretized with hexahedral mesh, 2D view.

The piecewise constant interpolation is a first order approximation, whereas the piecewise linear interpolation is a second order approximation. It can be represented as:

$$u_{ki}^{-} = u_i + \nabla u_i \cdot \mathrm{d}\vec{l}_{ki} \tag{2.33}$$

where ∇u_i represents the gradient of field values at the barycenter of the cell and $\mathrm{d}\vec{l}_{ki}$ is the position vector from barycenter to face center. Let ∇u_i be represented as shown below [57]:

$$\nabla u_i = s_i^{(x)} \vec{e}_x + s_i^{(y)} \vec{e}_y + s_i^{(z)} \vec{e}_z \tag{2.34}$$

where

$$\begin{pmatrix} s_i^{(x)} \\ s_i^{(y)} \\ s_i^{(z)} \end{pmatrix} = \begin{pmatrix} \sum\limits_{n_g} \delta x_{ij}^2 & \sum\limits_{n_g} \delta x_{ij} \delta y_{ij} & \sum\limits_{n_g} \delta x_{ij} \delta z_{ij} \\ \sum\limits_{n_g} \delta x_{ij} \delta y_{ij} & \sum\limits_{n_g} \delta y_{ij}^2 & \sum\limits_{n_g} \delta y_{ij} \delta z_{ij} \\ \sum\limits_{n_g} \delta x_{ij} \delta z_{ij} & \sum\limits_{n_g} \delta y_{ij} \delta z_{ij} & \sum\limits_{n_g} \delta z_{ij}^2 \end{pmatrix}^{-1} \begin{pmatrix} \sum\limits_{n_g} \delta u_{ij} \delta x_{ij} \\ \sum\limits_{n_g} \delta u_{ij} \delta y_{ij} \\ \sum\limits_{n_g} \delta u_{ij} \delta z_{ij} \end{pmatrix} \tag{2.35}$$

$$\delta u_{ij} = u_j - u_i \tag{2.36}$$

$$\delta x_{ij} = x_j - x_i \tag{2.37}$$

$$\delta y_{ij} = y_j - y_i \tag{2.38}$$

$$\delta z_{ij} = z_j - z_i \tag{2.39}$$

Note that j denotes one of the n_g cells contributing to the gradient, not necessarily the neighbor. Thus, Equation 2.34 can be written as:

$$u_{ki}^{-} = u_i + s_i^{(x)}\left(x_{ki} - x_i\right) + s_i^{(y)}\left(y_{ki} - y_i\right) + s_i^{(z)}\left(z_{ki} - z_i\right) \tag{2.40}$$

The gradient can be calculated by considering barycenter field values as shown above or by considering face center field values as shown below [6]:

$$\nabla u_i = \frac{1}{v_i}\sum_{k=1}^{m} s_{ki}u_{ki} \tag{2.41}$$

In the previous equation, u_{ki} represents the face center field value obtained as the weighted average of barycenter field values.

$$u_{ki} = \frac{w_j u_i + w_i u_j}{w_i + w_j} \tag{2.42}$$

The value of weight can be the volume of the cell or the nearest distance between the face center and cell center or the distance between the face center and cell center. In this work the distance between the face center and cell center is chosen as the weight. Hence, Equation 2.42 takes the form as below:

$$u_{ki} = \frac{\mathrm{d}l_{lj}u_i + \mathrm{d}l_{ki}u_j}{\mathrm{d}l_{ki} + \mathrm{d}l_{lj}} \tag{2.43}$$

2.3.2.2 Central Flux

In the central flux formulation, the face center field values on any face are equal to the average of the barycenter field values of the cells sharing that face.

$$u_{ki} = u_{lj} = \frac{u_i + u_j}{2} \tag{2.44}$$

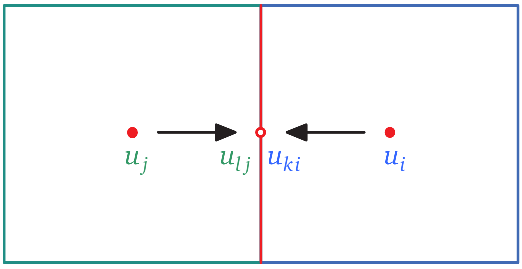

Figure 2.7: Averaging barycenter field values to obtain face center values for a non-boundary cell, in a domain discretized with hexahedral mesh, 2D view.

2.3.3 Time Marching

Only the L.H.S of Equation 2.21 or Equation 2.28 plays a role here. Runge–Kutta 1, Runge–Kutta 2, Heun 3, etc. are some of the time marching schemes that are examined. Consider a partial differential equation of the form

$$y' = f\left(x, y\right) \tag{2.45}$$

where y' represents the partial derivative with respect to time of the function $y = f\left(x, y\right)$. A function $y\left(x\right)$ is called a solution to the above equation if for all x,

$$y'\left(x\right) = f\left(x, y\left(x\right)\right) \tag{2.46}$$

The solution is determined when an initial value is prescribed as follows:

$$y\left(x_0\right) = y_0 \tag{2.47}$$

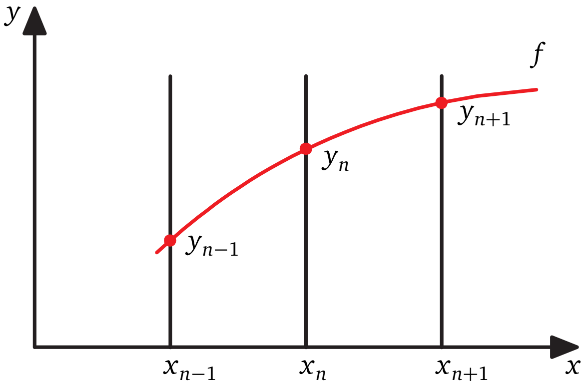

Figure 2.8: Numerical integration of a partial differential equation of the form $y' = f\left(x, y\right)$.

The solution to the aforementioned partial differential equation in Equation 2.45, can easily be obtained employing any of the Runge–Kutta methods. The family of explicit Runge–Kutta methods (s–stage) can be stated as:

$$y^{n+1} = y^n + (\Delta x) \sum_{i=1}^{s} b_i k_i \tag{2.48}$$

$$k_s = f\left(x_0 + c_s (\Delta x), y_0 + (\Delta x)\left(a_{s1} k_1 + \ldots + a_{s,s-1} k_{s-1}\right)\right) \tag{2.49}$$

The coefficients are displayed in Butcher's table [58–60], as below:

$$\begin{array}{c|ccccc} 0 & & & & & \\ c_2 & a_{21} & & & & \\ c_3 & a_{31} & a_{32} & & & \\ \vdots & \vdots & \vdots & \ddots & & \\ c_s & a_{s1} & a_{s2} & \cdots & a_{s,s-1} & \\ \hline & b_1 & b_2 & \cdots & b_{s-1} & b_s \end{array} \tag{2.50}$$

where s indicates the number of stages, and $a_{s,s-1}$, b_s, and c_s are real coefficients.

2.3.3.1 Runge–Kutta 1

$$\begin{array}{c|c} 0 & \\ \hline & 1 \end{array} \tag{2.51}$$

2.3.3.2 Runge–Kutta 2

$$\begin{array}{c|cc} 0 & & \\ 1/2 & 1/2 & \\ \hline & 0 & 1 \end{array} \tag{2.52}$$

2.3.3.3 Runge–Kutta 3

$$\begin{array}{c|cccc} 0 & & & & \\ 1/2 & 1/2 & & & \\ 1 & 0 & 1 & & \\ 1 & 0 & 0 & 1 & \\ \hline & 1/6 & 2/3 & 0 & 1/6 \end{array} \tag{2.53}$$

2.3.3.4 Runge–Kutta 4

$$\begin{array}{c|cccc} 0 & & & & \\ 1/2 & 1/2 & & & \\ 1/2 & 0 & 1/2 & & \\ 1 & 0 & 0 & 1 & \\ \hline & 1/6 & 2/6 & 2/6 & 1/6 \end{array} \tag{2.54}$$

2.3.3.5 Heun 3

$$\begin{array}{c|ccc} 0 & & & \\ 1/3 & 1/3 & & \\ 2/3 & 0 & 2/3 & \\ \hline & 1/4 & 0 & 3/4 \end{array} \tag{2.55}$$

2.4 Nomenclature

Figure 2.9 shows all the ingredients of finite volume formulation. The top layer of the figure shows the variations in the location of field components, the next two layers show the variations in flux approximation. The fourth and fifth layers depict the time marching schemes and meshes employed. The nomenclature used in this work is shown in the bottom layer of the diagram.

A FVTD method with upwind flux, first order spatial approximation and first order temporal approximation, on hexahedral mesh is named as FVTD UF 11 HEX.

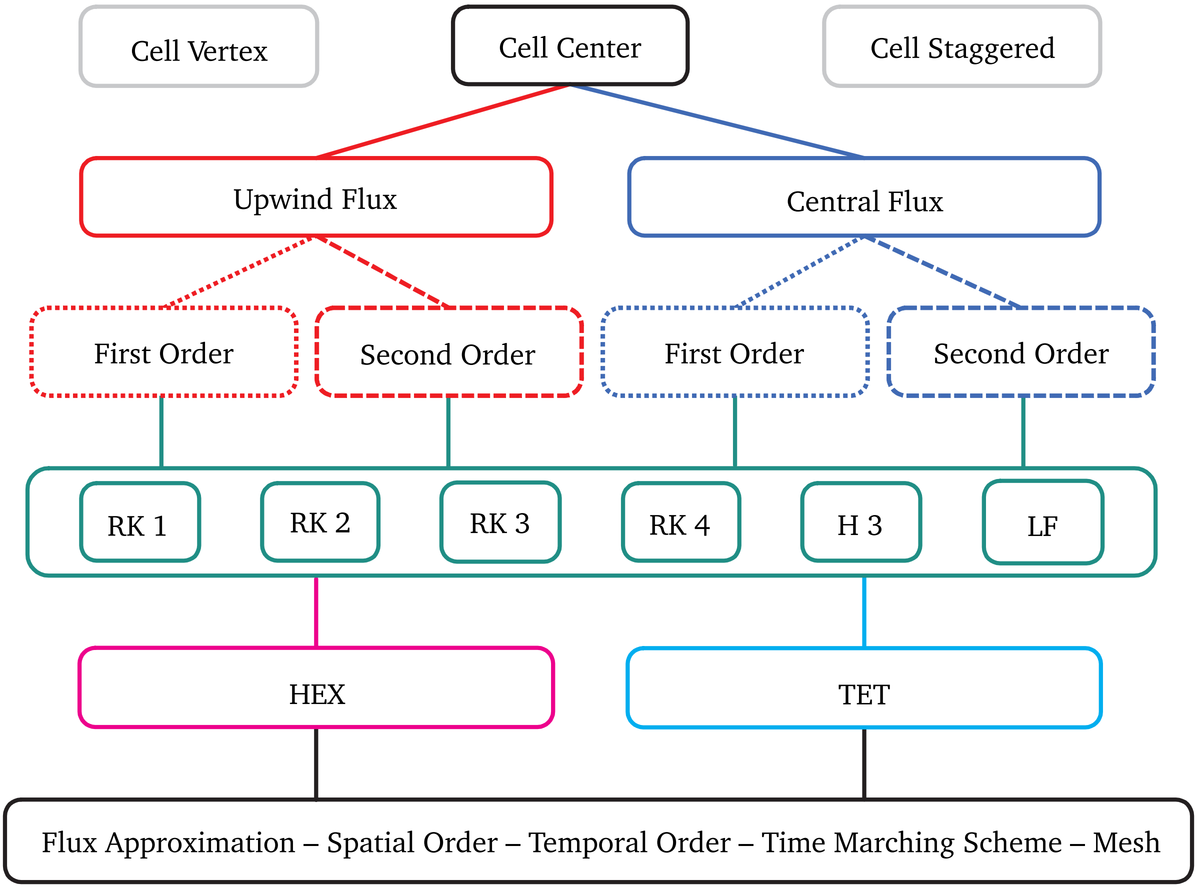

Figure 2.9: Nomenclature used for various finite volume methods. Each name consists of several parts indicating the type of flux approximation, spatial order, temporal order, time marching scheme, and mesh.

On similar grounds, a FVTD method with upwind flux, second order spatial approximation and first order temporal approximation, on hexahedral mesh should be named as FVTD UF 21 HEX. But the second order spatial approximation can be achieved either by using Gradient calculated from Cell Center field values (GCC) as described in Equation 2.34 or by using Gradient calculated from Face Center field values (GFC) as described in Equation 2.41. In such a case the FVTD method is renamed either as FVTD UF 21 GCC HEX or FVTD UF 21 GFC HEX in order to avoid the unclearness in naming.

A FVTD method with upwind flux, first order spatial approximation and third order temporal approximation, on tetrahedral mesh should be named as FVTD UF 13 TET. Again, there is ambiguity as third order temporal accuracy can be achieved using either Runge–Kutta 3 scheme or Heun 3 scheme. To avoid such indecipherable name an elaborated form is used such as FVTD UF 13 RK TET or FVTD UF 13 H TET.

Note that for the mentioned Butcher tables, Runge–Kutta 1 and Runge–Kutta 2 are nothing but forward Euler and modified Euler schemes, respectively. As the focus is on cell center methods, cell vertex and cell staggered formulations are already omitted from the graph. Later, all the above mentioned variations of cell center formulation are examined to find a stable method which is not computationally expensive.

2.5 Semidiscrete Formulation

Here the continuous forms of cell center finite volume systems, both upwind flux and central flux systems, are expressed in semidiscrete forms. These semidiscrete forms, discrete in the space and continuous in the time, are used to explain the spatial approximation of finite volume systems.

2.5.1 Cell Center Upwind Flux Semidiscrete Formulation

Omitting the details of derivation [6], the cell center upwind flux finite volume system represented in Equation 2.28, applied to i^{th} cell takes the form as below:

$$\begin{aligned}\frac{\partial u_i}{\partial t} &= -\frac{\alpha_i^{-1}}{v_i}\sum_{k=1}^{m_i} s_{ki}\left[\alpha_i t_{ki} A^+\left(\vec{n}_{ki}\right) u_{ki}^- + \alpha_j t_{lj} A^-\left(-\vec{n}_{ki}\right) u_{ki}^+\right] && (2.56)\\ &= -\frac{\alpha_i^{-1}}{v_i}\sum_{k=1}^{m_i}\left[\psi_{ki}^+ u_{ki}^- + \psi_{ki}^- u_{ki}^+\right] && (2.57)\\ &= \sum_{k=1}^{m_i}\left[\varphi_{ki}^+ u_{ki}^- + \varphi_{ki}^- u_{ki}^+\right] && (2.58)\\ &= \phi_i^+ + \phi_i^- && (2.59)\end{aligned}$$

where

$$\begin{aligned}\phi_i^+ &= \sum_{k=1}^{m_i}\varphi_{ki}^+ u_{ki}^- && (2.60)\\ \phi_i^- &= \sum_{k=1}^{m_i}\varphi_{ki}^- u_{ki}^+ && (2.61)\\ \varphi_{ki}^+ &= -\frac{\alpha_i^{-1}}{v_i}\psi_{ki}^+ = -\frac{\alpha_i^{-1}}{v_i} s_{ki}\alpha_i t_{ki} A^+\left(\vec{n}_{ki}\right) && (2.62)\\ \varphi_{ki}^- &= -\frac{\alpha_i^{-1}}{v_i}\psi_{ki}^- = -\frac{\alpha_i^{-1}}{v_i} s_{ki}\alpha_j t_{lj} A^-\left(-\vec{n}_{ki}\right) && (2.63)\\ \psi_{ki}^+ &= s_{ki}\alpha_i t_{ki} A^+\left(\vec{n}_{ki}\right) && (2.64)\\ \psi_{ki}^- &= s_{ki}\alpha_j t_{lj} A^-\left(-\vec{n}_{ki}\right) && (2.65)\end{aligned}$$

The matrices α_i (material matrix), t_{ki} (transmission matrix) and $A^+\left(\vec{n}_{ki}\right)$ are furnished in Appendix 1. The matrices α_j and t_{lj} can be written in an analogous way. The basic form of cell center upwind flux finite volume system is mentioned in Equation 2.56, whereas Equation 2.57, Equation 2.58 and Equation 2.59 express the same in various forms, which will be used in later sections.

2.5.2 Cell Center Central Flux Semidiscrete Formulation

The cell center finite volume system with central flux, applied to i^{th} cell, can be represented as:

$$\frac{\partial u_i}{\partial t} = -\frac{\alpha_i^{-1}}{v_i}\sum_{k=1}^{m_i} s_{ki}\left[\alpha_i t_{ki} B^+\left(\vec{n}_{ki}\right) u_{ki}^- + \alpha_j t_{lj} B^-\left(-\vec{n}_{ki}\right) u_{ki}^+\right] \qquad (2.66)$$

where substituting $\upsilon = 0$ in $A^+\left(\vec{n}_{ki}\right)$, and $A^-\left(-\vec{n}_{ki}\right)$ results in $B^+\left(\vec{n}_{ki}\right)$ and $B^-\left(-\vec{n}_{ki}\right)$, respectively.

2.5.3 Boundary Conditions

This section briefly explains about some of the boundary conditions in electromagnetics and how finite volume method handles those boundaries. The primary focus is on Perfect Electric Conductor (PEC) boundary condition, Perfect Magnetic Conductor (PMC) boundary condition and Open (Open) boundary condition. Appendix 1 furnishes the transmission matrices for these boundary conditions.

2.5.3.1 Perfect Electric Conductor Boundary Condition

In the case in which a cell encounters a perfect electric conductor, the tangential electric field on the cell face has to be zero. This leads to modification of outgoing and incoming fluxes through that face as below:

$$\psi_{ki}^{+} = s_{ki}\alpha_i t_{\mathrm{PEC}} A^{+}\left(\vec{n}_{ki}\right) \tag{2.67}$$
$$\psi_{ki}^{-} = 0 \tag{2.68}$$

2.5.3.2 Perfect Magnetic Conductor Boundary Condition

At PMC boundary, the tangential component of the magnetic field has to vanish, resulting in

$$\psi_{ki}^{+} = s_{ki}\alpha_i t_{\mathrm{PMC}} A^{+}\left(\vec{n}_{ki}\right) \tag{2.69}$$
$$\psi_{ki}^{-} = 0 \tag{2.70}$$

2.5.3.3 Open Boundary Condition

Open boundaries, also known as radiating boundaries or absorbing boundaries, are of special importance in dealing with various problems. These boundaries represent the radiation of electromagnetic waves into free space without any reflection. Numerically this is not possible in a broad frequency range at all angles of incidence. Nevertheless, the reflection can be minimized to a greater extent using several techniques like perfectly matched layer. In the case of FIT, these reflections are less than –120 dB, at all frequencies and at all angles of incidence. The perfectly matched layer model introduced by Berenger [61, 61–75], is extended for a cell center finite volume method in time domain recently [41]. However, this comes at an added cost and complexity.

Silver–Mueller ABC, on the other hand, is simple and inherent in the method. Mathematically it is represented as follows:

$$\psi_{ki}^{+} = s_{ki}\alpha_i t_{\mathrm{Open}} A^{+}\left(\vec{n}_{ki}\right) \tag{2.71}$$
$$\psi_{ki}^{-} = 0 \tag{2.72}$$

The above mentioned ABC is most efficient for normal incidence. There are several factors which influence the efficiency of radiating boundaries, like angle of incidence, discretization of domain in space, material present at the boundary, etc [41]. In order to contemplate on the method itself, this work does not use any radiating boundaries. The computational domain is simply extended such that there are no reflections from the boundaries during the simulation.

2.6 Discrete Formulation

Transforming the semidiscrete system into fully discrete system by opting an appropriate time marching scheme is furnished here. For a close inspection, choosing the time marching scheme is explained with the help of a 3D rectangular resonator with PEC walls on all sides and with dimensions 5 cm, 4 cm and

3 cm in x, y and z directions. Let this domain be discretized with hexahedral mesh such that there are 5 cells in x direction, 4 cells in y direction and 3 cells in z direction.

Consider a cell, say the i^{th} cell (black color), which is not located on the boundary of the computational domain, as shown in Figure 2.10(a). This cell shares its six faces, depicted in Figure 2.10(b), with six other cells, e.g., f_{1i} with j_1 and so on.

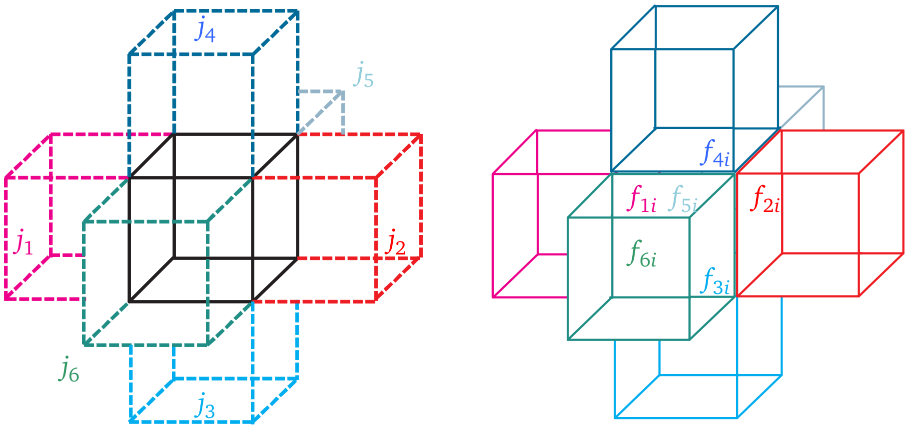

(a) Six neighbors. (b) Six faces.

Figure 2.10: A non–boundary cell in the computational domain discretized with hexahedral mesh, with six neighbors sharing the six faces.

2.6.1 System Matrix

Transforming the generalized cell center upwind flux finite volume semidiscrete formulation mentioned in Equation 2.58 to the hexahedral mesh yields:

$$\frac{\partial u_i}{\partial t} = \sum_{k=1}^{6}\left\{\varphi_{ki}^{+}u_{ki}^{-} + \varphi_{ki}^{-}u_{ki}^{+}\right\} \tag{2.73}$$

In Equation 2.73 one can observe that the unknowns are the field values at the cell centers and field values on faces. These field values on faces can be obtained from cell center field values either through piecewise constant interpolation or piecewise linear interpolation.

For the piecewise constant interpolation, the relation between the cell center field values and face center field values is expressed in Equation 2.31, and Equation 2.32. One can express Equation 2.73 as:

$$\frac{\partial u_i}{\partial t} = \begin{pmatrix} \sum_{k=1}^{6}\varphi_{ki}^{+} & \varphi_{1i}^{-} & \varphi_{2i}^{-} & \varphi_{3i}^{-} & \varphi_{4i}^{-} & \varphi_{5i}^{-} & \varphi_{6i}^{-} \end{pmatrix} \cdot \begin{pmatrix} u_i \\ u_{j_1} \\ u_{j_2} \\ u_{j_3} \\ u_{j_4} \\ u_{j_5} \\ u_{j_6} \end{pmatrix} \tag{2.74}$$

The above equation represents “local formulation” i.e., in each time step the field values in only one cell are updated. In order to find the updated values in the whole computational domain, the process is repeated for each cell. Equation 2.74 can be expressed in such a way that all field values in the computational domain will be updated at once in each time step. Such a formulation is called “global formulation” and is shown below.

$$\frac{\partial u}{\partial t} = \begin{pmatrix} \cdot & \cdots & & & & & & & & & & \cdots & \cdot \\ \vdots & \ddots & & & & & & & & & & & \vdots \\ & \varphi^-_{1i} & \sum\limits_{k=1}^{6} \varphi^+_{ki} & \varphi^-_{2i} & \cdots & \varphi^-_{3i} & \cdots & \varphi^-_{4i} & \cdots & \varphi^-_{5i} & \cdots & \varphi^-_{6i} & \\ & & & & & & & & & & & & \\ \vdots & & & & & & & & & & & & \vdots \\ & & & & & & & & & & & & \\ \vdots & \iddots & & & & & & & & & & \ddots & \vdots \\ \cdot & \cdots & & & & & & & & & & \cdots & \cdot \end{pmatrix} \cdot \begin{pmatrix} \vdots \\ u_{j_1} \\ u_i \\ u_{j_2} \\ \vdots \\ u_{j_3} \\ \vdots \\ u_{j_4} \\ \vdots \\ u_{j_5} \\ \vdots \\ u_{j_6} \\ \vdots \end{pmatrix} \tag{2.75}$$

The above equation has the form

$$\frac{\partial u}{\partial t} = Au \tag{2.76}$$

where A represents the system matrix, which has all mesh related information, and u represents the degrees of freedom in the computational domain.

Figure 2.11(a) and Figure 2.11(b) represent the system matrix constructed for the resonator mentioned before with first order upwind fluxes and central fluxes, respectively.

Constructing a system matrix for second order methods is not as direct as above, as the field values on faces for each cell are coupled with cell center values of neighbor cells. The following pages explain the construction of system matrix for the second order methods, where gradient is calculated from cell center values (GCC). Equation 2.73 can be expanded as:

$$\begin{aligned} \frac{\partial u_i}{\partial t} \quad = \quad & \sum_{k=1}^{2} \left\{ \varphi^+_{ki} u^-_{ki} \right\} + \sum_{k=3}^{4} \left\{ \varphi^+_{ki} u^-_{ki} \right\} + \sum_{k=5}^{6} \left\{ \varphi^+_{ki} u^-_{ki} \right\} + \\ & \sum_{k=1}^{2} \left\{ \varphi^-_{ki} u^+_{ki} \right\} + \sum_{k=3}^{4} \left\{ \varphi^-_{ki} u^+_{ki} \right\} + \sum_{k=5}^{6} \left\{ \varphi^-_{ki} u^+_{ki} \right\} \end{aligned} \tag{2.77}$$

Such an expression is justified as the gradient information used to obtain the field values on the faces f_{1i} and f_{2i}, f_{3i} and f_{4i}, f_{5i} and f_{6i} is unique. For the construction of gradient in x direction the information from immediate neighbors in x direction is enough on a hexahedral mesh. Hence Equation 2.35 reduces as below:

$$\begin{pmatrix} s_i^{(x)} \\ 0 \\ 0 \end{pmatrix} = \begin{pmatrix} \delta x^2_{ij_1} + \delta x^2_{ij_2} & 0 & 0 \\ 0 & 0 & 0 \\ 0 & 0 & 0 \end{pmatrix}^{-1} \begin{pmatrix} \delta u_{ij_1} \delta x_{ij_1} + \delta u_{ij_2} \delta x_{ij_2} \\ 0 \\ 0 \end{pmatrix} \tag{2.78}$$

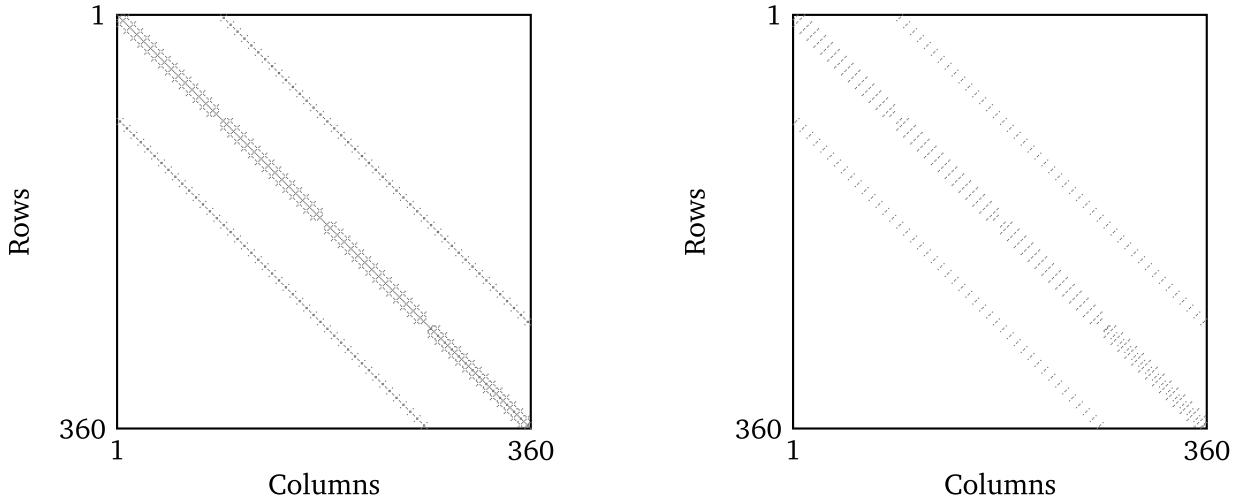

(a) First order upwind flux

(b) First order central flux

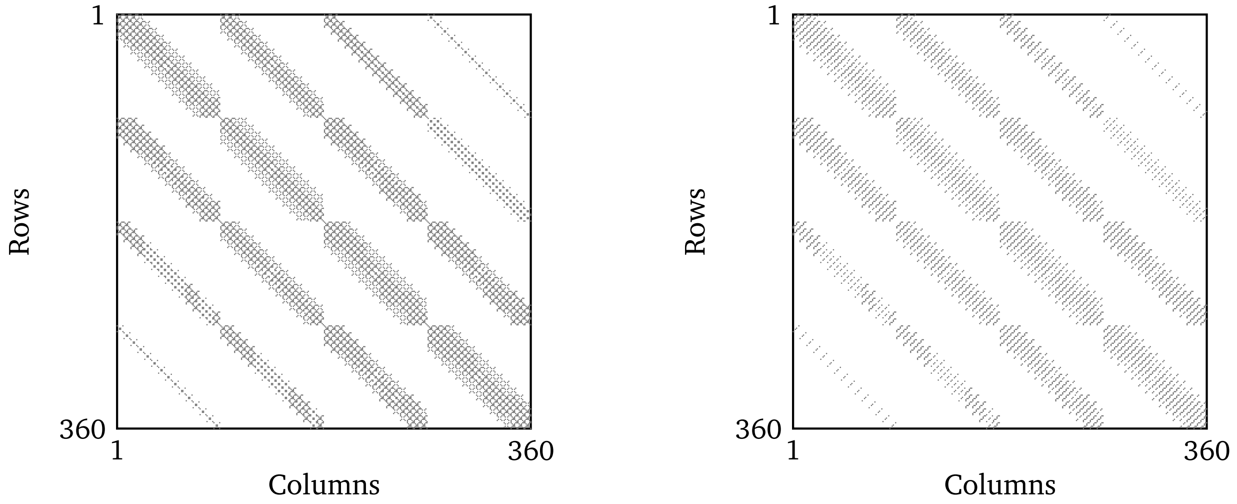

(c) Second order upwind flux

(d) Second order central flux

Figure 2.11: Sparsity patterns of system matrices of various finite volume formulations, obtained for the cube resonator discretized with hexahedral mesh. The total number of cells in the resonator is 60 and there are 6 degrees of freedom in each cell, making the total number of rows and columns in the system matrix equal to 360. Observe that the system matrices of central flux systems are sparser than their upwind flux counter parts. This is a direct result of annulling velocity (υ) in coefficient matrices to obtain the fluxes.

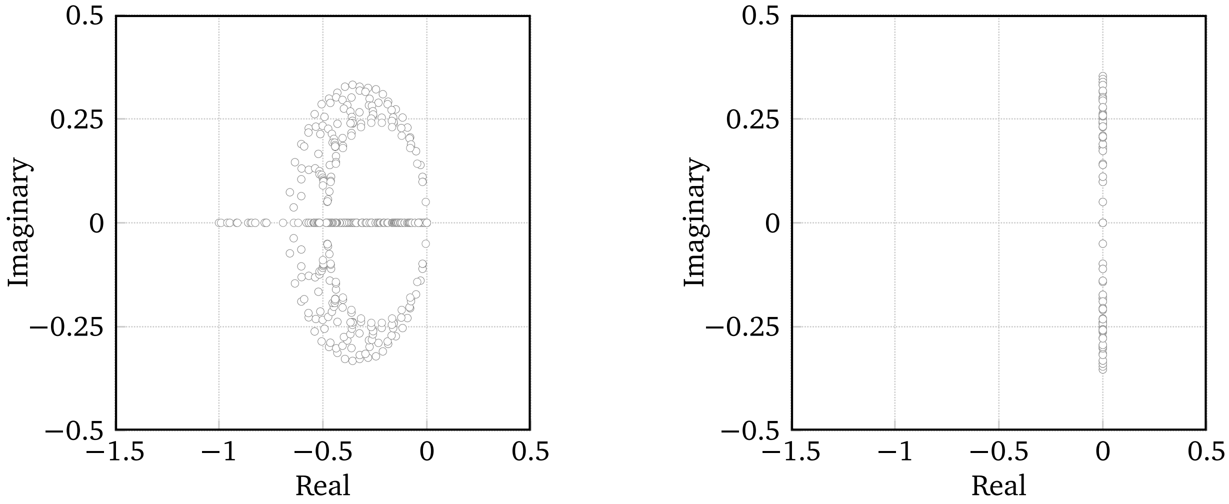

(a) First order upwind flux

(b) First order central flux

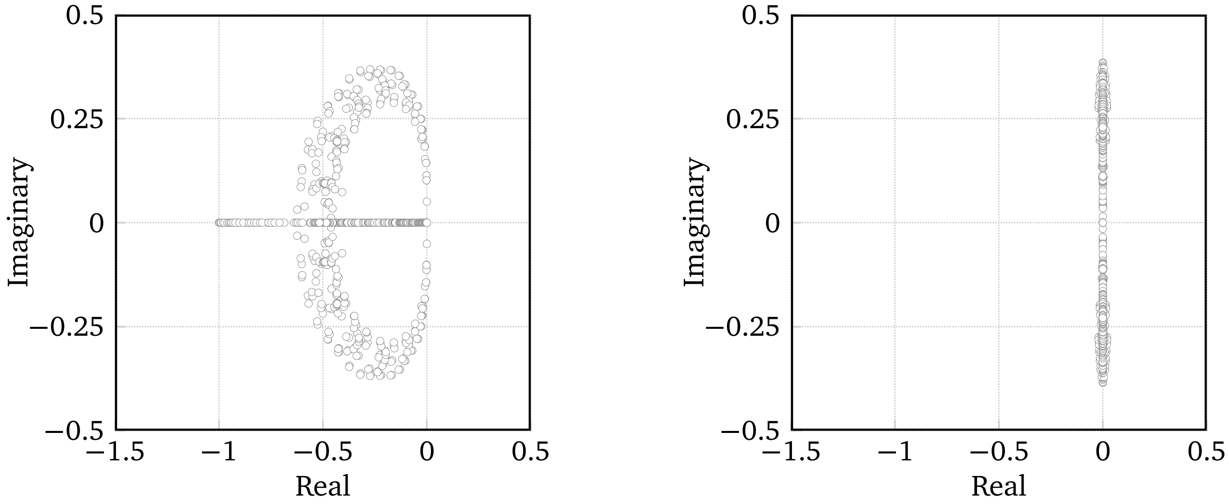

(c) Second order upwind flux

(d) Second order central flux

Figure 2.12: Eigenvalue distribution of various finite volume system matrices (normalized to maximum eigenvalue) obtained for the cube resonator discretized with hexahedral mesh. The eigenvalues, complex in nature, of upwind flux system matrices contains only non–positive real parts. On the other hand, the eigenvalues of central flux system matrices have both negative and positive real parts in addition to zeros. The first order central flux system has eigenvalues aligned along the imaginary axis whereas the distribution of eigenvalues for second order central system is symmetric along the imaginary axis.

This gradient value is used to obtain the field values on inside the faces f_{1i}, and f_{2i} as shown below:

$$u^-_{ki}\Big|_{k=1}^{k=2} = u_i + s_i^{(x)}\left(x_{ki}-x_i\right)\Big|_{k=1}^{k=2} \tag{2.79}$$

$$= u_i + \left(\delta x^2_{ij_1} + \delta x^2_{ij_2}\right)^{-1}\left(\delta u_{ij_1}\delta x_{ij_1} + \delta u_{ij_2}\delta x_{ij_2}\right)\left(x_{ki}-x_i\right)\Big|_{k=1}^{k=2} \tag{2.80}$$

$$= u_i\,\beta_{ki}\Big|_{k=1}^{k=2} + u_{j_1}\,\beta_{j_1}\Big|_{k=1}^{k=2} + u_{j_2}\,\beta_{j_2}\Big|_{k=1}^{k=2} \tag{2.81}$$

where

$$\beta_{ki}\Big|_{k=1}^{k=2} = 1 - \left(\delta x^2_{ij_1} + \delta x^2_{ij_2}\right)^{-1}\left(\delta x_{ij_1} + \delta x_{ij_2}\right)\left(x_{ki}-x_i\right)\Big|_{k=1}^{k=2} \tag{2.82}$$

$$\beta_{j_1}\Big|_{k=1}^{k=2} = \left(\delta x^2_{ij_1} + \delta x^2_{ij_2}\right)^{-1}\left(\delta x_{ij_1}\right)\left(x_{ki}-x_i\right)\Big|_{k=1}^{k=2} \tag{2.83}$$

$$\beta_{j_2}\Big|_{k=1}^{k=2} = \left(\delta x^2_{ij_1} + \delta x^2_{ij_2}\right)^{-1}\left(\delta x_{ij_2}\right)\left(x_{ki}-x_i\right)\Big|_{k=1}^{k=2} \tag{2.84}$$

Observe Equation 2.81 represents a decoupled system when compared to Equation 2.80 in terms of field values. Though not mentioned here, expressions for field values inside the faces f_{3i}, and f_{4i} can be obtained from gradient in y direction. Gradient in z direction yields field values inside the faces f_{5i}, and f_{6i}. One can write

$$\sum_{k=1}^{2}\left\{\varphi^+_{ki}u^-_{ki}\right\} = \left[\varphi^+_{ki}\beta_{ki}\right]\Big|_{k=1}^{k=2}u_i + \left[\varphi^+_{ki}\beta_{j_1}\right]\Big|_{k=1}^{k=2}u_{j_1} + \left[\varphi^+_{ki}\beta_{j_2}\right]\Big|_{k=1}^{k=2}u_{j_2} \tag{2.85}$$

$$\sum_{k=3}^{4}\left\{\varphi^+_{ki}u^-_{ki}\right\} = \left[\varphi^+_{ki}\beta_{ki}\right]\Big|_{k=3}^{k=4}u_i + \left[\varphi^+_{ki}\beta_{j_3}\right]\Big|_{k=3}^{k=4}u_{j_3} + \left[\varphi^+_{ki}\beta_{j_4}\right]\Big|_{k=3}^{k=4}u_{j_4} \tag{2.86}$$

$$\sum_{k=5}^{6}\left\{\varphi^+_{ki}u^-_{ki}\right\} = \left[\varphi^+_{ki}\beta_{ki}\right]\Big|_{k=5}^{k=6}u_i + \left[\varphi^+_{ki}\beta_{j_5}\right]\Big|_{k=5}^{k=6}u_{j_5} + \left[\varphi^+_{ki}\beta_{j_6}\right]\Big|_{k=5}^{k=6}u_{j_6} \tag{2.87}$$

The net outgoing flux, ψ^+_i, is the sum of outgoing fluxes through all the faces.

$$\phi^+_i = \sum_{k=1}^{6}\left\{\varphi^+_{ki}u^-_{ki}\right\} = \sum_{k=1}^{2}\left\{\varphi^+_{ki}u^-_{ki}\right\} + \sum_{k=3}^{4}\left\{\varphi^+_{ki}u^-_{ki}\right\} + \sum_{k=5}^{6}\left\{\varphi^+_{ki}u^-_{ki}\right\} \tag{2.88}$$

$$\begin{aligned} = & \left\{\left[\varphi^+_{ki}\beta_{ki}\right]\Big|_{k=1}^{k=2} + \left[\varphi^+_{ki}\beta_{ki}\right]\Big|_{k=3}^{k=4} + \left[\varphi^+_{ki}\beta_{ki}\right]\Big|_{k=5}^{k=6}\right\}u_i + \\ & \left[\varphi^+_{ki}\beta_{j_1}\right]\Big|_{k=1}^{k=2}u_{j_1} + \left[\varphi^+_{ki}\beta_{j_2}\right]\Big|_{k=1}^{k=2}u_{j_2} + \\ & \left[\varphi^+_{ki}\beta_{j_3}\right]\Big|_{k=3}^{k=4}u_{j_3} + \left[\varphi^+_{ki}\beta_{j_4}\right]\Big|_{k=3}^{k=4}u_{j_4} + \\ & \left[\varphi^+_{ki}\beta_{j_5}\right]\Big|_{k=5}^{k=6}u_{j_5} + \left[\varphi^+_{ki}\beta_{j_6}\right]\Big|_{k=5}^{k=6}u_{j_6} \end{aligned} \tag{2.89}$$

$$= \theta_i u_i + \theta_{j_1}u_{j_1} + \theta_{j_2}u_{j_2} + \theta_{j_3}u_{j_3} + \theta_{j_4}u_{j_4} + \theta_{j_5}u_{j_5} + \theta_{j_6}u_{j_6} \tag{2.90}$$

Similarly, the gradient in all neighbor cells should be calculated in order to obtain the values on the outside of each face of cell i.

Equation 2.59 can be written in the global form as:

$$\frac{\partial u}{\partial t} = \left(A^{+} + A^{-}\right) u \tag{2.91}$$

where A^{+} consists of mesh information related to outgoing fluxes and A^{-} consists of mesh information related to incoming fluxes.

$$A^{+}u = \begin{pmatrix} \cdot & \cdots & & & & & & & & & & \cdots & \cdot \\ \vdots & \ddots & & & & & & & & & & & \vdots \\ & \theta_{j1} & \theta_{i} & \theta_{j2} & \cdots & \theta_{j3} & \cdots & \theta_{j4} & \cdots & \theta_{j5} & \cdots & \theta_{j6} & \\ & & & & & & & & & & & & \\ \vdots & & & & & & & & & & & & \vdots \\ & & & & & & & & & & & & \\ \vdots & \iddots & & & & & & & & & & \ddots & \vdots \\ \cdot & \cdots & & & & & & & & & & \cdots & \cdot \end{pmatrix} \cdot \begin{pmatrix} \vdots \\ u_{j1} \\ u_{i} \\ u_{j2} \\ \vdots \\ u_{j3} \\ \vdots \\ u_{j4} \\ \vdots \\ u_{j5} \\ \vdots \\ u_{j6} \\ \vdots \end{pmatrix} \tag{2.92}$$

Figure 2.11(c), and Figure 2.11(d) represent the system matrix constructed with second order upwind fluxes and central fluxes, respectively. As expected these matrices are sparse. One can observe the central flux system matrices are a bit more sparse than the upwind flux system matrices, which is a direct result of substituting $\upsilon = 0$ in matrices $A^{+}(\vec{n})$ and $A^{-}(-\vec{n})$. On a Cartesian mesh, the computation of gradient is very efficient and easy. This process does not populate the system matrix much. But on a tetrahedral mesh, most of the times, it is not sufficient to consider only the neighbors for calculating the gradient. Sometimes it is necessary to consider neighbors of neighbors to obtain the gradient, which does populate the system matrix to a great extent. One can use the geometric properties of the mesh to pick the neighbors that contribute the most to the gradient [76].

Transforming Equation 2.76 into FD, one can obtain the eigenvalue formulation of the system. The normalized eigenvalue distribution of the aforementioned system matrices in the complex plane are depicted in Figure 2.12.

2.6.2 Iteration Matrix

By applying the time marching schemes mentioned in Section 2.3.3, the solution to generalized finite volume system given in Equation 2.76 can be represented as:

$$u^{n+1} = G u^{n} \tag{2.93}$$

where G is called the iteration matrix. G is a function of time step, Δt. The eigenvalue distribution of the iteration matrix depicts the stability of a scheme for some particular time step. Appendix 2 furnishes iteration matrices obtained using various time marching schemes like Runge–Kutta 1, Runge–Kutta 2, etc.

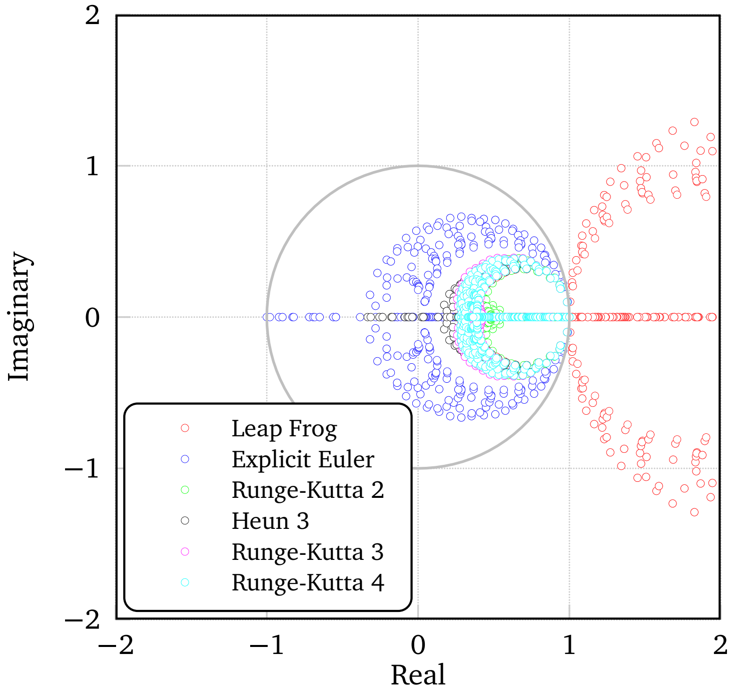

Figure 2.13: Eigenvalue distribution of first order upwind flux method iteration matrices obtained using various time marching schemes at the optimal time step value. The unit circle encloses the stable zone. The Leap Frog time marching scheme is not stable.

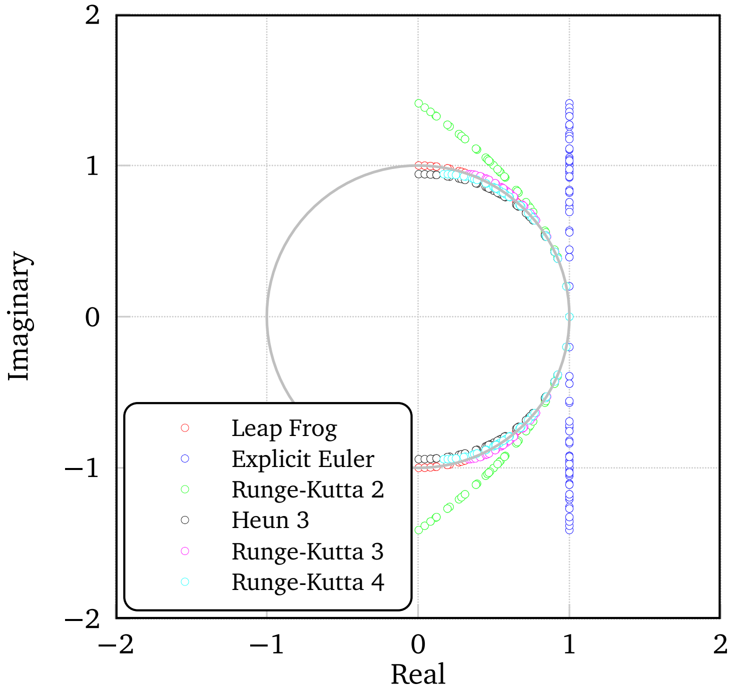

Figure 2.14: Eigenvalue distribution of first order central flux method iteration matrices obtained using various time marching schemes at the Courant limit. The unit circle encloses the stable zone. The Runge–Kutta 1, Runge–Kutta 2, Runge–Kutta 3 time marching schemes are not stable.

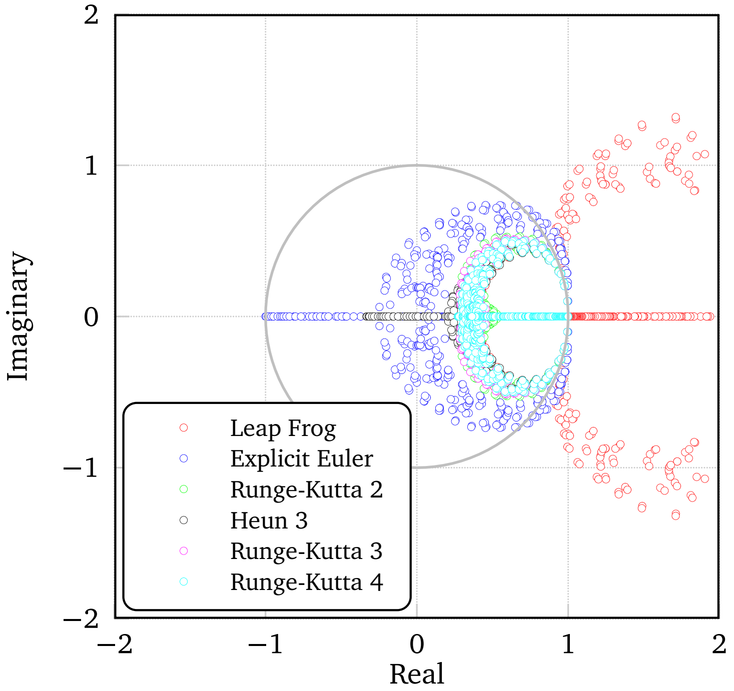

Figure 2.15: Eigenvalue distribution of second order upwind flux method iteration matrices obtained using various time marching schemes at the maximum possible time step. The unit circle encloses the stable zone. One can observe that the Leap Frog and Runge–Kutta 1 time marching schemes are not stable.

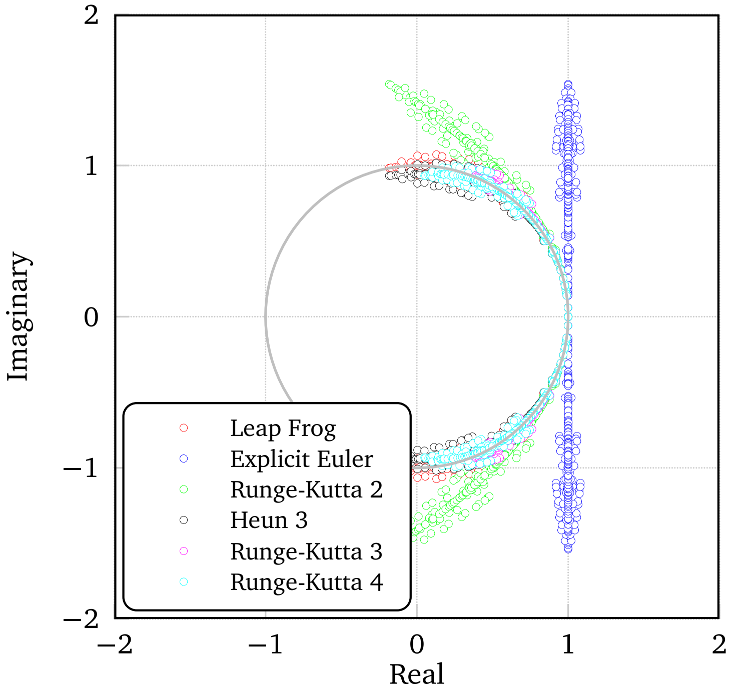

Figure 2.16: Eigenvalue distribution of second order central flux method iteration matrices obtained using various time marching schemes at the optimal time step value. The unit circle encloses the stable zone. One can observe that there is no time marching scheme that satisfies the stability condition.

Omitting the details of derivation, the stability limit obtained from Courant–Friedrichs–Lewy condition for Runge–Kutta 1 time marching scheme is [6, 77, 78]:

$$\Delta t \leq \min \left(\frac{1}{\upsilon_i} \frac{v_i}{\sum_{k=1}^{m_i} s_{ki}} \right) \tag{2.94}$$

The time step is chosen to be this limit for the first order flux approximations. For the second order flux approximations the Courant–Friedrichs–Lewy limit relaxes the time step to be twice this value with Runge–Kutta 2 time marching scheme.

Figure 2.13, Figure 2.14, Figure 2.15 and Figure 2.16 represent the eigenvalue distribution of the iteration matrices obtained with various time marching schemes for different flux approximations of cell center finite volume methods. The perimeter of the circle bounds the stable zone. One can observe from Figure 2.13 that the Leap Frog scheme is not stable, whereas all the rest of the schemes are stable for first order upwind flux system. For the first order central flux finite volume system mentioned in Figure 2.14, the Heun 3, the Runge–Kutta 4 and the Leap Frog are the stable schemes. Due to simplicity Leap Frog is generally used for first order central flux finite volume system. The Runge–Kutta 2, the Heun 3, the Runge–Kutta 3 and the Runge–Kutta 4 are stable schemes for second order upwind flux finite volume system.

There is no suitable time integrator found for second order central flux system. On the other hand, the first order central flux system has stable time integrators. However, first order central flux system has more dispersion [79] and neglected for further investigation.

For both first order and second order upwind flux systems there are multiple time marching schemes available. A higher order time marching scheme with a second order flux approximation does not guarantee more accurate results. Moreover, higher order time marching schemes induce additional computational cost. For these reasons the finite volume methods examined in this work are restricted to upwind flux systems, at most to second order. To be more precise, from here onwards, the first order upwind flux method with Runge-Kutta 1 time marching (FVTD 11) and the second order upwind flux methods (FVTD 22 GCC and FVTD 22 GFC) with Runge–Kutta 2 are considered on hexahedral and tetrahedral meshes. The following listing illustrates the same. Observe in the nomenclature the letters “UF”, representing “upwind flux” are dropped as all the methods considered from here onwards belong to the “UF” family.

FVTD 11 HEX : Finite volume time domain method, first order in space and time, on hexahedral mesh
FVTD 22 GCC HEX : Finite volume time domain method, second order in space and time, on hexahedral mesh (Gradient calculated from Cell Center values)
FVTD 22 GCC HEX : Finite volume time domain method, second order in space and time, on hexahedral mesh (Gradient calculated from Face Center values)
FVTD 11 TET : Finite volume time domain method, first order in space and time, on tetrahedral mesh
FVTD 22 GCC TET : Finite volume time domain method, second order in space and time, on tetrahedral mesh (Gradient calculated from Cell Center values)
FVTD 22 GFC TET : Finite volume time domain method, second order in space and time, on tetrahedral mesh (Gradient calculated from Face Center values)

Figure 2.17: Finite volume time domain methods examined from here onwards in this work. First order and second order (Gradient calculated from Cell Center values and Gradient calculated from Face Center values) methods on hexahedral and tetrahedral meshes are under investigation. Note that all of them are upwind flux formulations.

2.6.3 Curl Curl Matrix

Taking partial derivative of Equation 2.75, with respect to time and transforming into frequency domain, yields:

$$\left(A^2 + I\omega^2\right) u = 0 \tag{2.95}$$

The term, A^2, in parentheses in the above equation is called the curl curl matrix A_{cc}, ω being the eigenfrequency of the system, and u is the corresponding eigenvector. Generally, the curl curl matrix is used to obtain the eigenmodes of the system.

2.7 Sources

Impression of energy into a computational domain is a multi dimensional problem, space and time being the variables. In other words, every physical source has a spatial pattern or dimension and a temporal pattern.

2.7.1 Spatial Pattern

In FVTD the two major categories of sources are point sources and face sources. The cell center point sources and face center point sources fall into the first category, whereas ports or more specifically waveguide ports fall into the second category.

2.7.1.1 Point Sources

A source with infinitesimal spatial dimension can be considered as a point source. Point sources can be classified as hard point sources and soft point sources. A hard point source is nothing but imposing a field component with a time function in the computational domain, without considering the effect of neighbors i.e., without considering the effect of time marching field values. As time marching continues, eventually a reflected wave arrives back at the source point location and undergoes a non–physical reflection from the hard point source. On the other hand, soft point sources consider the effect of time marching field values and thus reduce the effect of these reflections.

The location of these point sources can be either at the barycenter of the cell or at the face center of the cell. Let $f(t)$ be the desired time function, then mathematically a hard point source at the barycenter can be described as Equation 2.96, whereas Equation 2.97 describes a soft source at the barycenter of the cell. Equation 2.98 and Equation 2.99 describe the hard and soft point sources, respectively, at the face center.

$$u_i^{n+1} = f(t) \tag{2.96}$$
$$u_i^{n+1} = f(t) + u_i^n \tag{2.97}$$

$$u_{ki}^{n+1} = f(t) \tag{2.98}$$
$$u_{ki}^{n+1} = f(t) + u_{ki}^n \tag{2.99}$$

2.7.1.2 Ports

Ports, more specifically waveguide ports, are the most common form of impressing energy into the computational domain. Ports imitate the extension of computational domain to infinity. In the time domain, extraction of the scattering parameters (S–parameters), which describe the electrical behavior of linear networks, is facilitated by observing the fields or waves in and out of the ports. Thus, ports play a great role in device characterization.

Consider a waveguide device (only a portion is shown) as shown in the Figure 2.18, with port dimensions $a = 6$ cm and $b = 3$ cm. Let this device be truncated with PEC boundary conditions in x and y directions. Let the port plane be discretized with a hexahedral mesh with 20 CPW at 3 GHz. Several port modes and cutoff frequencies are obtained using the curl curl matrix of the second order upwind flux method with gradient calculated form cell center values (FVTD 22 GCC HEX).

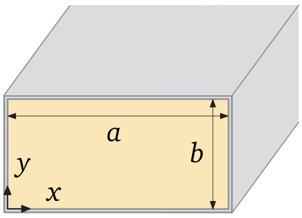

Figure 2.18: A portion of a waveguide device, with port plane highlighted. The waveguide is truncated with PEC boundary conditions in x and y directions. The port plane dimensions are $a = 6$ cm and $b = 3$ cm.

The electric field patterns of the fundamental mode, TE_{10} is portrayed in Figure 2.19(a). The mode patterns of the subsequent higher order modes are also presented in Figure 2.19(b), Figure 2.19(c), Figure 2.19(d). Note that only TE mode patterns are shown. These modes occur at different frequencies.

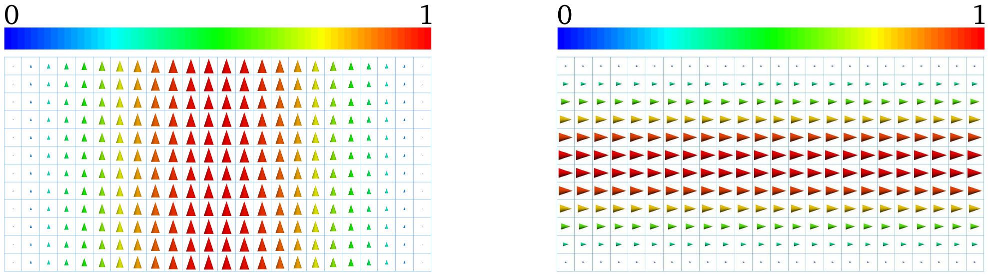

(a) Fundamental mode

(b) First higher order mode

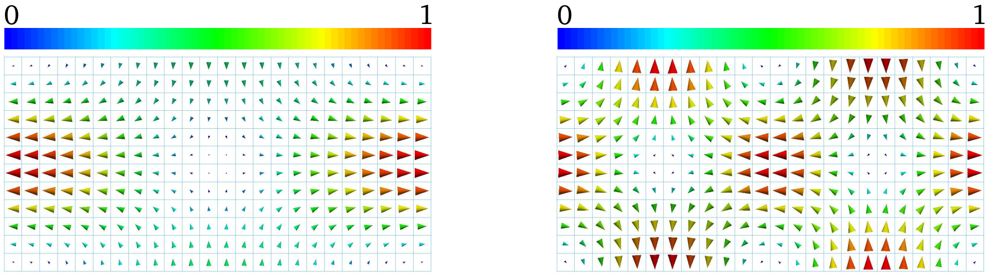

(c) Second higher order mode

(d) Third higher order mode

Figure 2.19: The electric field patterns of the fundamental mode and the next higher order modes obtained from second order upwind flux finite volume method with Gradient calculated from Cell Center values on hexahedral mesh (FVTD 22 GCC HEX) acting as an eigenmode solver when the port is discretized with hexahedral mesh with a spatial resolution of 20 CPW. Only TE mode patterns are shown.

In order to observe the efficiency of an eigenmode solver, a convergence study is made in terms of minimum error. The discretization is changed to 25 CPW from 20 CPW and the cutoff frequency of the fundamental mode is obtained again. This process is repeated till the spatial resolution reaches 50 CPW, in steps of 5 CPW. The cutoff frequency of the fundamental mode is also obtained using FIT for aforementioned spatial resolutions. The port plane is discretized with triangular mesh and again the cutoff frequency is obtained for various spatial resolutions ranging from 15 CPW to 30 CPW, in steps of 5 CPW.

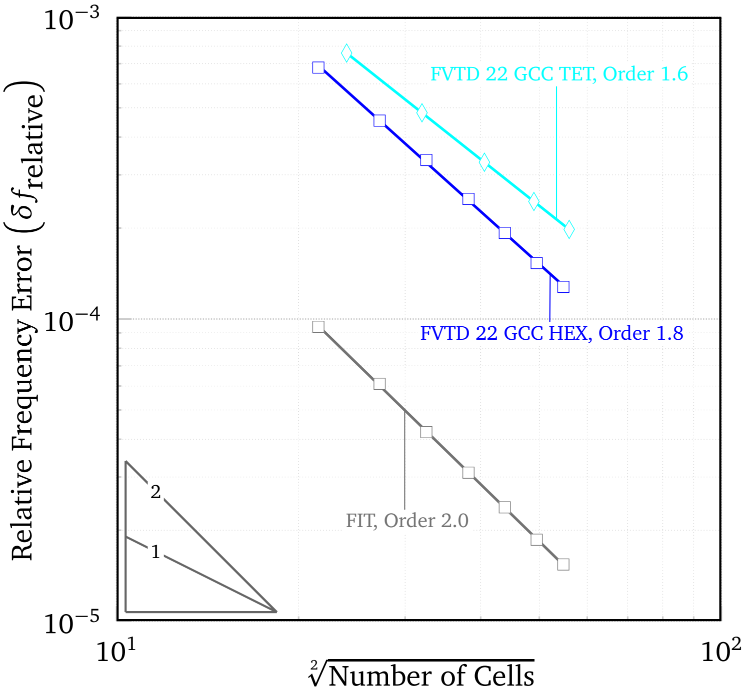

Figure 2.20: Convergence of error in the cutoff frequency for the fundamental mode at the port. FIT eigenmode solver on hexahedral mesh has minimum error when compared to eigenmode solvers based finite volume formulation, irrespective of the mesh. The diagonals of the right angle triangle indicate the reference orders.

Figure 2.20 depicts the convergence of relative frequency error, defined below, for second order upwind flux finite volume method with gradient calculated from cell center values (FVTD 22 GCC) on hexahedral and tetrahedral meshes along with FIT on hexahedral mesh. One can observe that the error is more in the case of finite volume methods when compared to FIT.

$$\delta f_{\text{relative}} = \frac{\left| f_{\text{analytical}} - f_{\text{numerical}} \right|}{f_{\text{analytical}}} \tag{2.100}$$

Any numerical method when employed as an eigenmode solver produces non–physical modes (ghost modes). In the case of FIT these modes can be detected using the “divergence free” property of discretized Maxwell’s equations [3, 80, 81]. However, this is not the case with upwind flux finite volume methods because upwinding does not conserve the charge [56, 79, 82]. However, one can use techniques such as “divergence cleaning” [48–50], but the approach is computationally intensive. For this reason, all the physical modes depicted in Figure 2.19 are picked up manually based on the mode pattern and the eigenfrequency.

2.7.2 Temporal Pattern

Figure 2.21 shows the dispersion curves at the port mentioned in Section 2.6.2. In general, only the modes with cutoff frequency below the highest frequency of the excitation signal are propagated without attenuation throughout the structure. If the frequency spectrum of the excitation signal is as shown in red solid line, only TE_{10} mode will propagate, if the frequency spectrum is as shown in red dashed line, TE_{10} and TE_{01} modes will propagate. Similarly, if the excitation signal spectrum is as shown in red dotted line, TE_{10}, TE_{01} and TE_{11} modes will propagate while TE_{21} mode cannot propagate. Thus, the temporal pattern of the excitation signal plays a major role in the impression of energy as it excites certain modes. The excitation function used in this work is broadband Gaussian pulse as it excites a lot of frequencies within the desired limits.

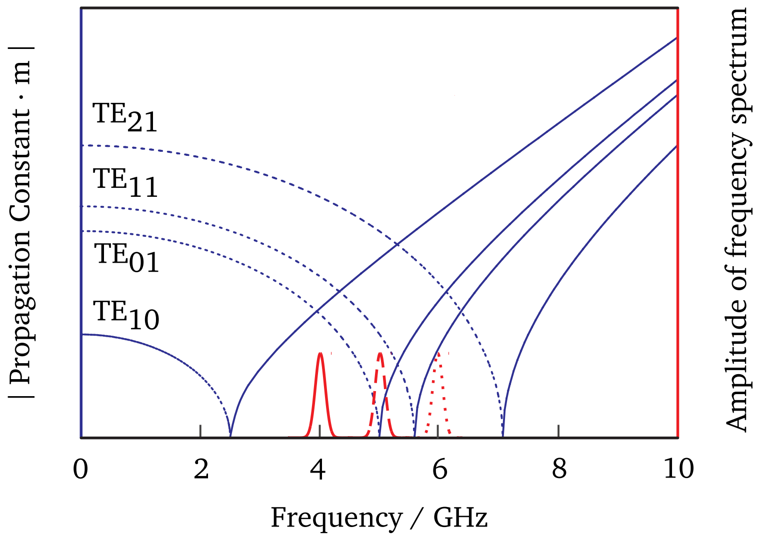

Figure 2.21: Dispersion curves of a rectangular waveguide. The cutoff frequencies are depicted. For any given mode, the propagation constant is real above the cutoff frequency and imaginary below the cutoff frequency.

2.7.2.1 Broadband Gaussian Pulse

A broadband Gaussian pulse can be expressed as:

$$f(t) = e^{-\left(t-t_0/\sigma\right)^2} \sin\left(2\pi f_0 t\right) \tag{2.101}$$

where f_0 is the center frequency, σ is a measure of the width of the pulse and t_0 the shift in time. Figure 2.22 presents a broadband Gaussian pulse with dominant spectrum between 2 GHz and 4 GHz in TD and FD. Though the frequency spectrum extends from $-\infty$ to $+\infty$, the dominant frequency spectrum is only a portion of it. The spectrum with amplitude of 10 % or more of maximum is considered as the dominant frequency spectrum in this work.

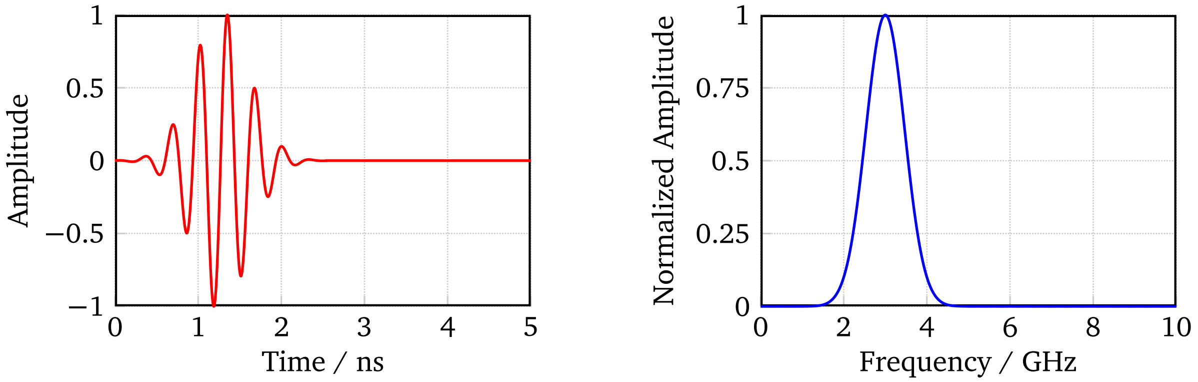

Figure 2.22: A broadband Gaussian pulse in time and frequency domains. The dominant frequency spectrum, the spectrum with amplitude of 10 % or more of the maximum amplitude, is between 2 GHz and 4 GHz.

2.8 Extraction of Scattering Parameters

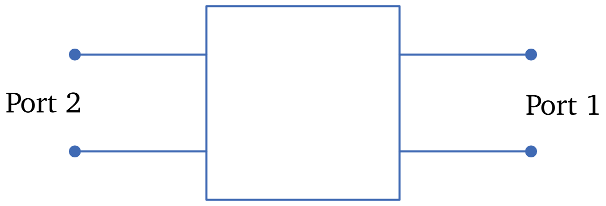

Figure 2.23: A two port network.

Without loss of generality consider a linear two port network as shown in Figure 2.23. Power, voltage, current and fields can be considered to be in the form of waves traveling in both directions through this network. This can be characterized by a set of simultaneous equations describing the exiting waves from each port in terms of incident waves at each port [83, 84]. These equations can be expressed in matrix form as below:

$$\begin{bmatrix} b_1 \\ b_2 \end{bmatrix} = \begin{bmatrix} S_{11} & S_{12} \\ S_{21} & S_{22} \end{bmatrix} \begin{bmatrix} a_1 \\ a_2 \end{bmatrix} \tag{2.102}$$

where a_1, b_1 represent the incoming (into the network) and outgoing (out of the network) waves at port 1 ($p1$) and a_2, b_2 represent the incoming and outgoing waves at port 2 ($p2$). The coefficients S_{11}, S_{12}, S_{21}, and S_{22} are called the scattering parameters (S–parameters). The matrix consisting of these parameters is called the scattering matrix. The external behavior of this linear network can be predicted without any regard for the contents of the network using scattering matrix. The S–parameters are complex parameters, as the transmitted and reflected waves can differ from incident waves either in amplitude, or in phase, or in both. The S–parameters are defined for a given frequency and system impedance, and vary as a function of frequency for any non–ideal network. The S–matrix for an N–port network contains N^2 coefficients, each one representing a possible input–output path[85]. The number of rows or columns in a scattering matrix is equal to the number of ports per mode.

2.8.1 Analytical Formulation

Consider a transverse plane in the waveguide as shown in Figure 2.24. The fields in such a plane are superposition of incoming and outgoing waves. Let $U(x, y, \omega)$ represent the total field in the transverse plane.

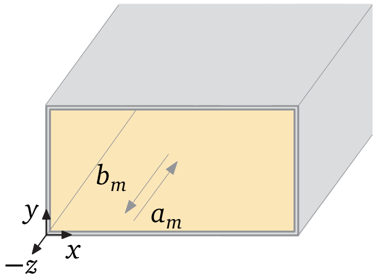

Figure 2.24: A portion of a waveguide device, with port plane highlighted. The waveguide is truncated with PEC boundary conditions in x and y directions. The amplitude of m^{th} mode in the field that is moving into the device is denoted by a_m whereas the amplitude of the m^{th} mode in the field that is moving out of the device is denoted by b_m.

The field in the transverse plane can be expressed as [86–93]:

$$U(x, y, \omega) = \sum_{m=1}^{\infty} \left(a_m(j\omega) U_m(x, y, \omega) e^{-\gamma_m(j\omega)z} + b_m(j\omega) U_m(x, y, \omega) e^{\gamma_m(j\omega)z} \right) \tag{2.103}$$

where $U_m(x, y, \omega)$, γ_m represent the mode pattern and the propagation constant of m^{th} eigenmode. The amplitudes of the m^{th} eigenmode in the fields that are entering and leaving the device at the port are denoted by a_m and b_m, respectively. Note $e^{-\gamma_m(j\omega)z}$ represents the wave traveling into the waveguide. In other words, the transverse field in the waveguide at any given frequency can be decomposed into different eigenmodes traveling in either direction. The S–parameters are defined as the ratio between these amplitudes, as shown below:

$$S(j\omega) = \frac{b_m(j\omega)}{a_m(j\omega)} \tag{2.104}$$

Expanding the transverse field into eigenmodes traveling in either direction and computing the amplitudes of these modes forms the basis for extracting the S–parameters. By exciting a broadband pulse in the time domain and performing a Fourier Transform (FT) on the sampled time domain data, it is possible to obtain S–parameters for a broad frequency range.

2.8.1.1 Orthogonality of Eigenmodes

Let $\vec{E}_a$, $\vec{E}_b$ represent the electric field distribution of modes a and b in FD. The orthogonality of the eigenmodes for a homogeneous port can be expressed as follows:

$$\int_S \left(\vec{E}_a \cdot \vec{E}_b \right) \mathrm{d}S \rightarrow \begin{cases} = 0, \ a \neq b \\ \neq 0, \ a = b \end{cases} \tag{2.105}$$

2.8.2 Numerical Formulation

In order to explain the extraction of S–parameters, step by step, consider an air filled parallel plate waveguide placed in the first octant of the coordinate system as shown in Figure 2.25(a), with dimensions 10 cm, 5 cm, and 50 cm in x, y, and z directions, respectively. This waveguide is truncated with PEC boundaries (represented in magenta color) in y direction, PMC boundaries (represented in cyan color)in x direction. There are two ports (represented in red color) located at the extreme ends in z direction. Let port 1, $p1$, be the excitation port and port 2, $p2$, be the observation port.

The computation of S–parameters requires the termination of waveguide ports with minimized reflection. This can be mimicked by "open" boundaries simulating infinitely long waveguides connected to the port planes. As mentioned in Section 2.5.3.3, Silver Muller ABC is very efficient for normal incidence. As the fundamental mode in a parallel plate waveguide is a TEM mode one can use these absorbing boundary conditions.

Let this domain be discretized with hexahedral mesh, with 10 CPW, such that $p1$ consists of K_{p1} faces and $p2$ consists of K_{p2} faces. In other words, $p1$ consists of K_{p1} cells and $p2$ consists of K_{p2} cells. In each of these cells, let face l represent the port face. Figure 2.25(b) portrays the cells belonging to each port.

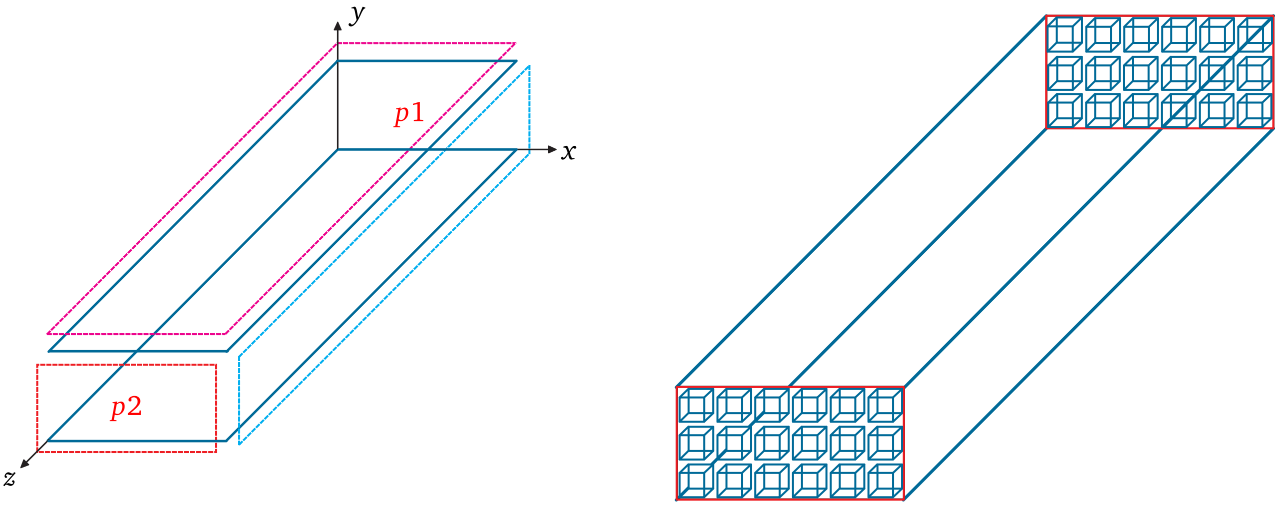

(a) Domain with boundaries

(b) Domain with visible port cells

Figure 2.25: A parallel plate waveguide with dimensions 10 cm, 5 cm, 50 cm in x, y and z directions. The waveguide is truncated by PEC boundaries (shown in magenta color) in y direction, PMC boundaries (depicted in cyan color) in x direction. The ports located at the extreme ends of waveguide are outlined in red color.

The cell center upwind finite volume system for each cell i in the domain, mentioned in Equation 2.57, can be modified at the excitation port as [94]:

$$\frac{\partial u_i}{\partial t} = \left[\sum_{k=1}^{m_i, k \neq l} \left[\varphi_{ki}^{+} u_{ki}^{-} + \varphi_{ki}^{-} u_{ki}^{+} \right] + \left[\varphi_{li}^{+} u_{li}^{-} + \varphi_{li}^{-} u_{li}^{+} \right] + \left[\varphi_{li}^{+} v_{li}^{-} + \varphi_{li}^{-} v_{li}^{+} \right] \right] \tag{2.106}$$

where v_{li}^{-}, and v_{li}^{+} represents the imposed field values. Let the fundamental mode be imposed at $p1$, represented as $u_{p1,m1}$. The mode pattern is depicted in Figure 2.26.

The fields expressions are as follows:

$$E_y = E_0 \tag{2.107}$$

$$H_x = -\frac{E_0}{\eta_0} \tag{2.108}$$

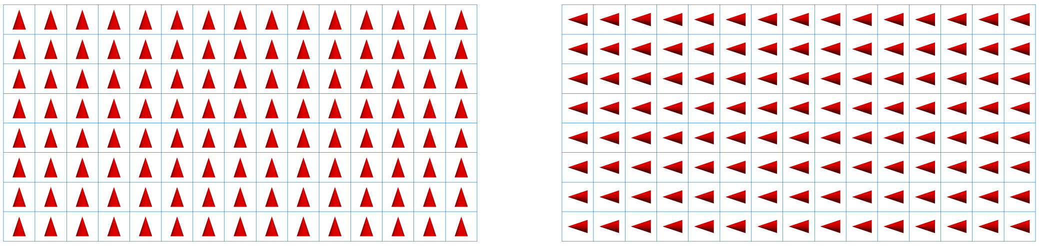

(a) Electric field pattern

(b) Magnetic field pattern

Figure 2.26: Imposed electric and magnetic field patterns of the fundamental mode (TEM) at the excitation port, when the domain is discretized with hexahedral mesh at a resolution of 10 CPW at 3 GHz.

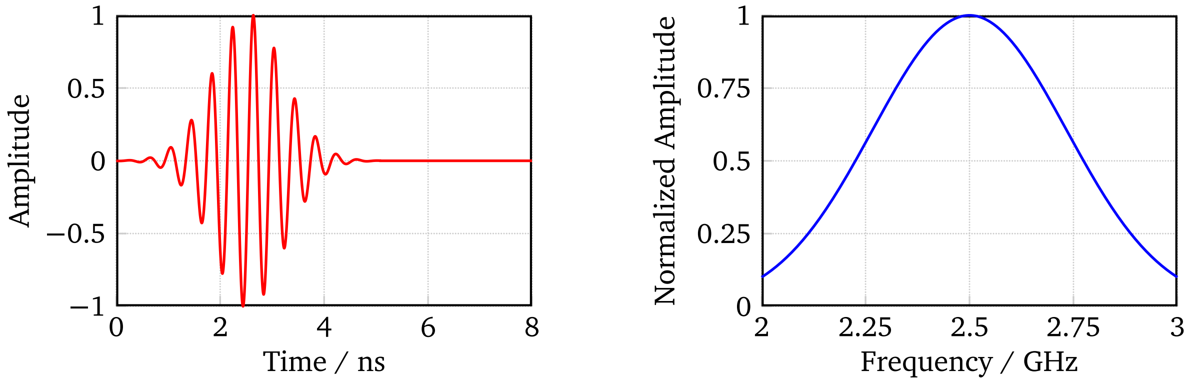

Figure 2.27: Time and frequency domain representations of parallel plate waveguide excitation. The dominant frequency spectrum is between 2 GHz and 3 GHz.

Though this mode can be excited with any temporal excitation pattern (as the cutoff frequency is zero) a broadband Gaussian pulse as shown in Figure 2.27 is used. For the sake of simplicity define

$$\overset{\frown}{\varphi}{}^{+}_{li} = \begin{pmatrix} \overset{\frown}{\varphi}{}^{e+}_{li} \\ \overset{\frown}{\varphi}{}^{h+}_{li} \end{pmatrix} = \varphi^{+}_{li} u^{-}_{li} \tag{2.109}$$

$$\overset{\frown}{\varphi}{}^{-}_{li} = \begin{pmatrix} \overset{\frown}{\varphi}{}^{e-}_{li} \\ \overset{\frown}{\varphi}{}^{h-}_{li} \end{pmatrix} = \varphi^{-}_{li} u^{+}_{li} \tag{2.110}$$

$$\overset{\smile}{\varphi}{}^{+}_{li} = \begin{pmatrix} \overset{\smile}{\varphi}{}^{e+}_{li} \\ \overset{\smile}{\varphi}{}^{h+}_{li} \end{pmatrix} = \varphi^{+}_{li} v^{-}_{li} \tag{2.111}$$

$$\overset{\smile}{\varphi}{}^{-}_{li} = \begin{pmatrix} \overset{\smile}{\varphi}{}^{e-}_{li} \\ \overset{\smile}{\varphi}{}^{h-}_{li} \end{pmatrix} = \varphi^{-}_{li} v^{+}_{li} \tag{2.112}$$

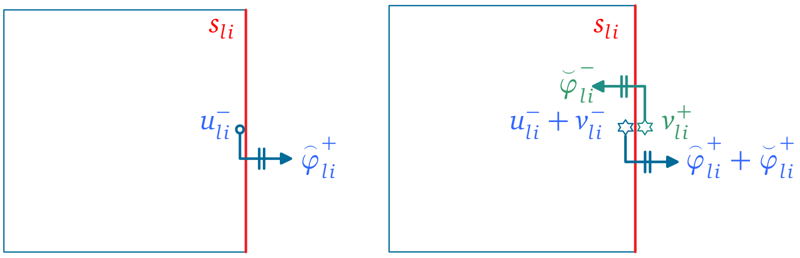

(a) After stimulation. (b) During stimulation.

Figure 2.28: Exchange of fluxes at the excitation port during and after stimulation. During the stimulation in addition to the fluxes arising from upwind field values there are also fluxes originating from the imposed field values.

The value of $\overset{\frown}{\varphi}_{li}^{-}$ is zero as the field values outside the port faces, u_{li}^{+}, are zero. To extract the scattering parameters, one can utilize the fluxes mentioned in Equation 2.109 to Equation 2.112. In order to obtain the amplitude of a particular mode, the orthogonality relation expressed in Equation 2.105 is used, as the discrete solutions of this eigenvalue problem fulfill the orthogonality properties of continuous waveguide modes. The amplitude of mode 1, $m1$, in the distribution of field at $p1$ and $p2$ in each time step is as follows:

$$a_{p1,m1}(t) = \sum_{l=1}^{K_{p1}} \left(\breve{\varphi}_{li}^{e-} \right) \cdot v_{p1,m1,li} \tag{2.113}$$

$$b_{p1,m1}(t) = \sum_{l=1}^{K_{p1}} \left(\breve{\varphi}_{li}^{e+} + \overset{\frown}{\varphi}_{li}^{e+} \right) \cdot v_{p1,m1,li} \tag{2.114}$$

$$b_{p2,m1}(t) = \sum_{l=1}^{K_{p2}} \left(\overset{\frown}{\varphi}_{li}^{e+} \right) \cdot v_{p2,m1,li} \tag{2.115}$$

Transforming these quantities into frequency domain, the S–parameters can be obtained as mentioned below:

$$S_{11,m1,m1}(\omega) = b_{p1,m1}(\omega) \Big/ a_{p1,m1}(\omega) \tag{2.116}$$

$$S_{21,m1,m1}(\omega) = b_{p2,m1}(\omega) \Big/ a_{p1,m1}(\omega) \tag{2.117}$$

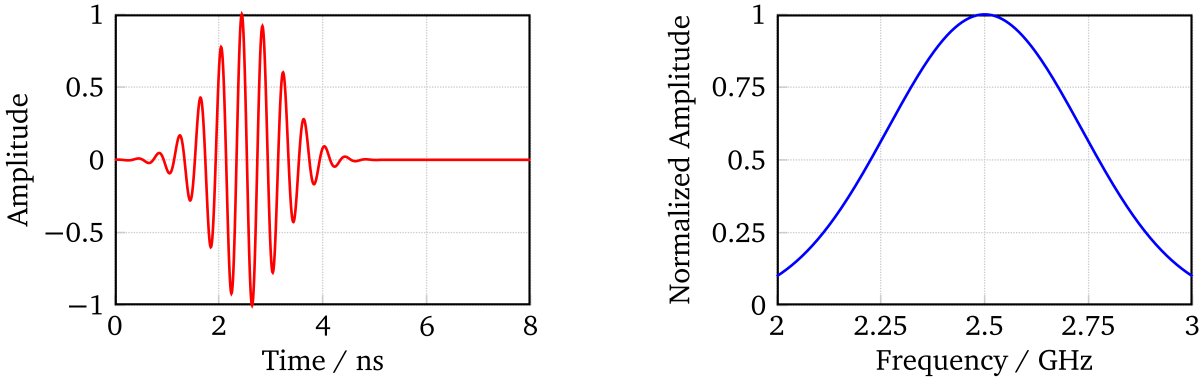

Figure 2.29: Time and frequency domain representations of fields coming into the domain (traveling in $+z$ direction) at the excitation port. Observe the amplitude of these is equal to that of the excitation signal, as the modulated fundamental mode has the amplitude of unity.

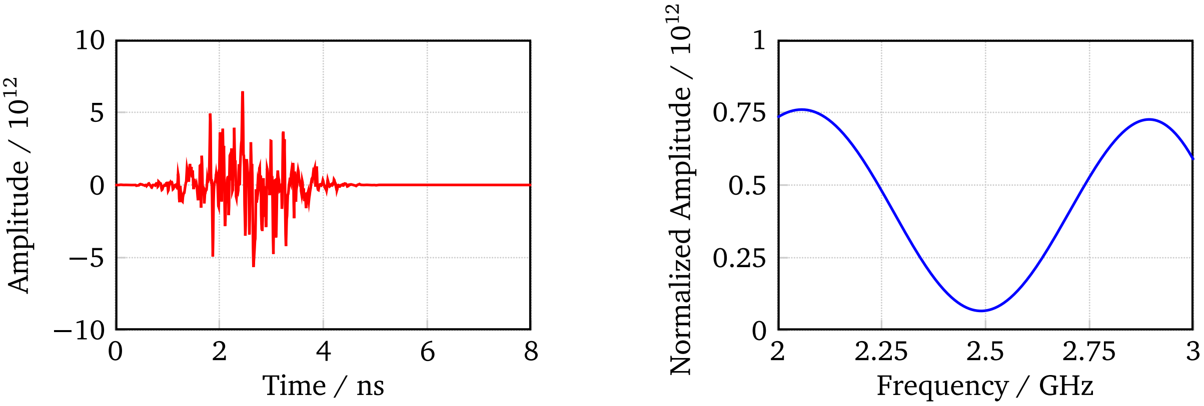

Figure 2.30: Time and frequency domain representations of fields going out of the excitation port i.e., back scattered due to varying reasons such as coarse mesh, etc. The reflection can be considered as ideal as the amplitude is infinitesimal.

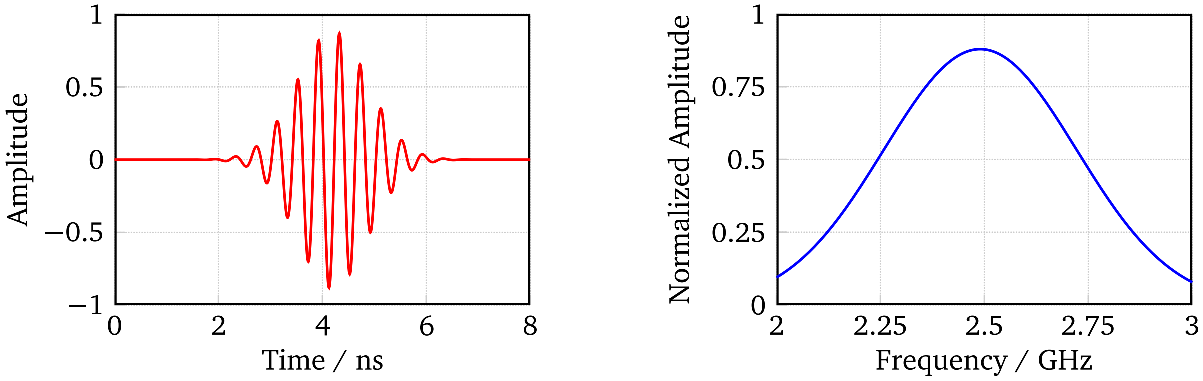

Figure 2.31: Time and frequency domain representations of fields going out of the observation port. Observe the decay in amplitude when compared to the excitation signal. The decay in amplitude is expected as the simulation is carried out with upwind flux FVTD method.

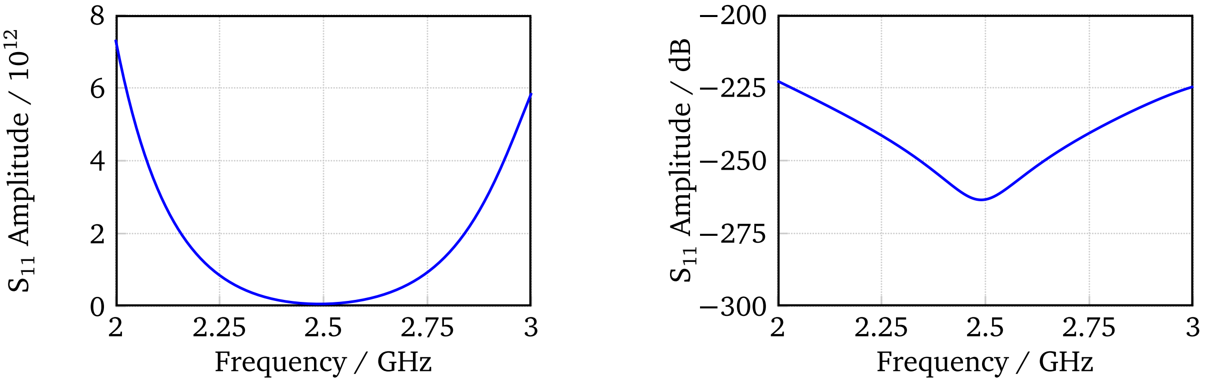

Figure 2.32: The scattering parameter S_{11} obtained using the second order upwind flux method with Gradient calculated using Cell Center values on hexahedral mesh in linear and log (dB) scales. The amplitude of S_{11} can be considered as zero.

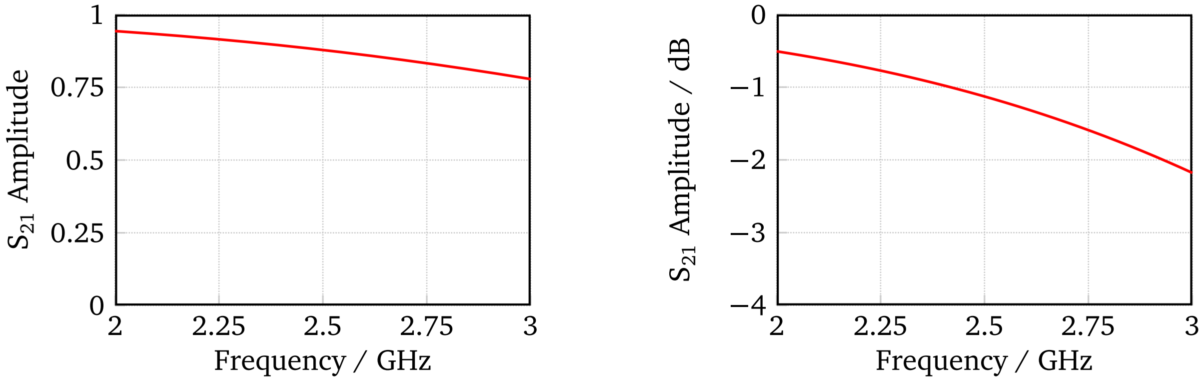

Figure 2.33: The scattering parameter S_{21} obtained using the second order upwind flux method with Gradient calculated using Cell Center values on hexahedral mesh in linear and log (dB) scales. The decay in the amplitude of the S_{21} is not uniform over the entire frequency range.

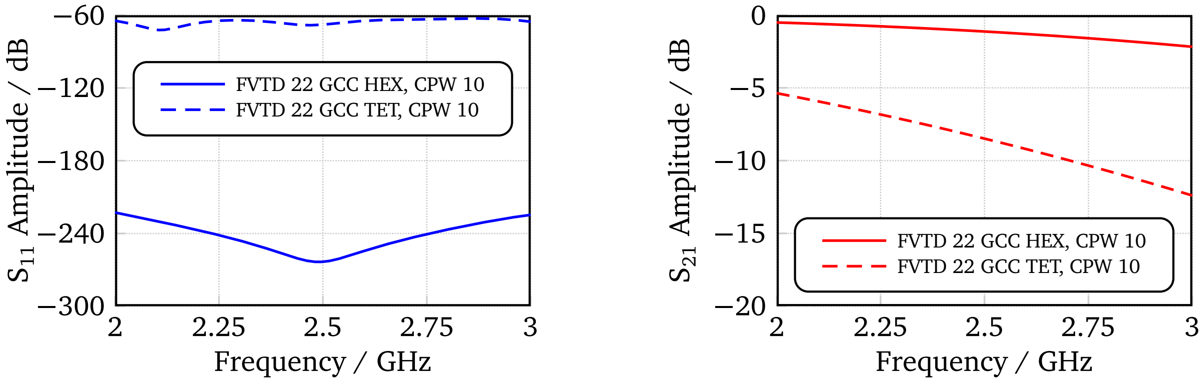

Figure 2.34: The S-parameters obtained using the second order upwind flux method with Gradient calculated using Cell Center values on hexahedral and tetrahedral meshes. The imposed mode fits better to the mesh and the precision of gradient is high in the case of hexahedral mesh yielding more accurate S-parameters.

The S–parameters are depicted in Figure 2.32 and Figure 2.33. One can observe the amplitude of S_{11} is as low as −225 dB from Figure 2.32(b). The deviation of S_{21} from the expected value, 0 dB, is visible in Figure 2.33(b). This is a direct consequence of the dissipative property of upwinding.

In Figure 2.34 a comparison between the S–parameters obtained using hexahedral mesh and tetrahedral mesh (discretized with 10 CPW) is presented. One can observe the reflection coefficient is significant when using tetrahedral mesh. This is a direct outcome of the mode not fitting to the mesh. Also the transmission coefficient, S_{21} deviates more from the expected value of 0 dB. This is obvious as the computed gradient is less accurate than that of the hexahedral mesh.

The extraction of S–parameters in a multimode environment can be done in a similar approach. The following equations show the S–parameter the extraction for different stimulations:

$$S_{11,m2,m1}(\omega) = b_{p1,m2}(\omega) \big/ a_{p1,m1}(\omega) \tag{2.118}$$

$$S_{21,m2,m1}(\omega) = b_{p2,m2}(\omega) \big/ a_{p1,m1}(\omega) \tag{2.119}$$

$$S_{11,m1,m2}(\omega) = b_{p1,m1}(\omega) \big/ a_{p1,m2}(\omega) \tag{2.120}$$

$$S_{21,m1,m2}(\omega) = b_{p2,m1}(\omega) \big/ a_{p1,m2}(\omega) \tag{2.121}$$

3 Convergence Analysis

Abstract *– The Lax equivalence theorem states that for a consistent numerical method with a well posed linear initial value problem, the method is convergent, if and only if, it is stable. This "convergent" property is examined here. The convergence of the solutions obtained from various upwind flux finite volume time domain methods in different scenarios is presented and compared with the solutions from the finite integration technique and the finite element method.*

Four resonators, filled with Vacuum, are considered such that each one belongs to one of the following categories:

(1) simple geometry
(2) complex geometry
(3) simple geometry with singularity
(4) complex geometry with singularity

The convergence of the solutions obtained from upwind flux FVTD methods in terms of resonant frequency and amplitude are observed for each of these models. The results are compared with that of FIT and FEM. In order to observe the convergence a reference solution is necessary. For most of the models mentioned above, the reference solution is not known e.g., resonator with complex geometry and singularity.

Obtaining the Reference Solution: The computational domain is discretized with a coarse hexahedral mesh and the resonant frequency of the fundamental mode is obtained from CST MWS eigenmode solver. The mesh is refined and the resonant frequency of the fundamental mode is obtained again. This process is repeated till the difference between any two consecutive resonant frequencies (normalized) falls below 1 per mil. The resonant frequency obtained with finer mesh is considered as the reference solution from CST MWS eigenmode solver.

The domain is discretized with a coarse tetrahedral mesh and the resonant frequency is obtained from FEM with first order edge elements. Similar procedure as mentioned above is employed to find reference solution from FEM eigenmode solver.

The resonant frequencies obtained from CST MWS eigenmode solver and FEM eigenmode solver are compared. If the difference between them lies around 1 per mil, then the resonant frequency from CST MWS eigenmode solver is considered as the reference solution. For most of the cases this reference solution is obtained if the domain is discretized with 150 CPW or more.

3.1 Simple Geometry

Consider a box resonator truncated with PEC walls on all the sides with dimensions 3 m, 2 m, and 1 m in x, y, and z directions, respectively as depicted in Figure 3.1(a). The fundamental mode in this resonator is TM_{110} mode, with resonant frequency approximately at 90.07 MHz. The field expressions for $\mathrm{TM}_{\mathrm{mnp}}$ modes in such a resonator with dimensions a, b, and c in x, y, and z directions are as follows [53]:

$$E_x(x,y,z) = \frac{-1}{\gamma^2+k^2}\frac{m\pi}{a}\frac{p\pi}{c}E_0\cos\left(\frac{m\pi}{a}x\right)\sin\left(\frac{n\pi}{b}y\right)\sin\left(\frac{p\pi}{c}z\right) \tag{3.1}$$

$$E_y(x,y,z) = \frac{-1}{\gamma^2+k^2}\frac{n\pi}{b}\frac{p\pi}{c}E_0\sin\left(\frac{m\pi}{a}x\right)\cos\left(\frac{n\pi}{b}y\right)\sin\left(\frac{p\pi}{c}z\right) \tag{3.2}$$

$$E_z(x,y,z) = E_0\sin\left(\frac{m\pi}{a}x\right)\sin\left(\frac{n\pi}{b}y\right)\cos\left(\frac{p\pi}{c}z\right) \tag{3.3}$$

$$H_x(x,y,z) = \frac{j\omega\varepsilon}{\gamma^2+k^2}\frac{n\pi}{b}E_0 \sin\left(\frac{m\pi}{a}x\right)\cos\left(\frac{n\pi}{b}y\right)\cos\left(\frac{p\pi}{c}z\right) \tag{3.4}$$

$$H_y(x,y,z) = \frac{-j\omega\varepsilon}{\gamma^2+k^2}\frac{m\pi}{a}E_0 \cos\left(\frac{m\pi}{a}x\right)\sin\left(\frac{n\pi}{b}y\right)\cos\left(\frac{p\pi}{c}z\right) \tag{3.5}$$

$$H_z(x,y,z) = 0 \tag{3.6}$$

The number of half cycles in x, y, and z directions are represented as m, n, and p, respectively. The propagation constant and wave number are denoted as γ and k, ω being the resonant angular frequency. The amplitude of electric field is denoted by E_0.

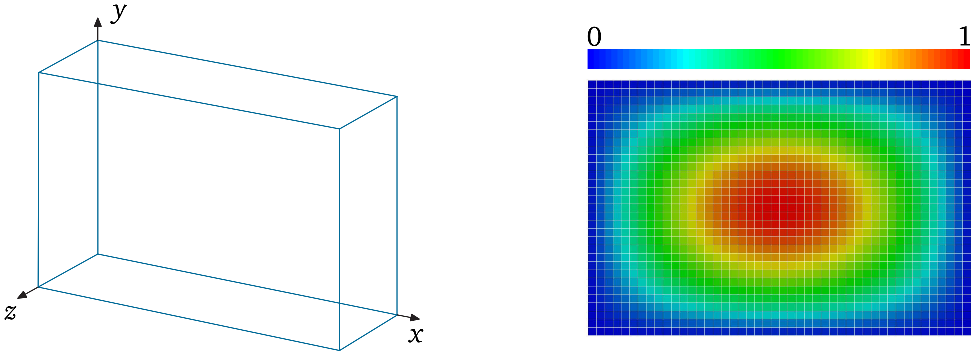

(a) Outline view of the physical model.

(b) Imposed electric field of the fundamental mode on the plane at $z = 0.5$ m.

Figure 3.1: The outline view of a Vacuum filled box resonator, truncated with PEC boundaries on all sides, with dimensions 3 m, 2 m, and 1 m in x, y and z directions, respectively. The resonator is discretized with hexahedral mesh at a spatial resolution of 15 CPW and the electric field pattern of the fundamental mode is imposed on the plane, $z = 0.5$ m, at the center of the medium.

This resonator is discretized with hexahedral mesh such that there are at least 15 CPW at 92 MHz. The 3D field pattern of the fundamental mode is taken as the initial condition and is imposed on the mesh. Figure 3.1(b) depicts the imposed electric field pattern in the resonator on the xy plane at $z = 0.5$ m. This mode is allowed to oscillate freely in time using first and second order FVTD methods. The time step is chosen to be the optimal value for all the methods i.e., the Courant number is kept to be 1.0. The field components are recorded at the center of the computational domain for 5 cycles of oscillation. The total energy in the domain is also observed during these cycles.

Figure 3.2 depicts the monitored electric field component, E_z, using first and second order FVTD methods. This is used to obtain the resonant frequency and dissipation coefficient through curve fitting. It has the form of an exponentially decaying oscillation as mentioned below:

$$f(t) = a_0 e^{-\alpha t}\sin(\omega t + \delta) \tag{3.7}$$

where a_0 represents the initial amplitude, α represents the dissipation coefficient, ω represents the angular frequency and δ represents the phase offset. The electric energy in the domain is also depicted in Figure 3.3. One can also observe the artificial dissipation of the energy. First order method has much more artificial dissipation compared to the second order methods.

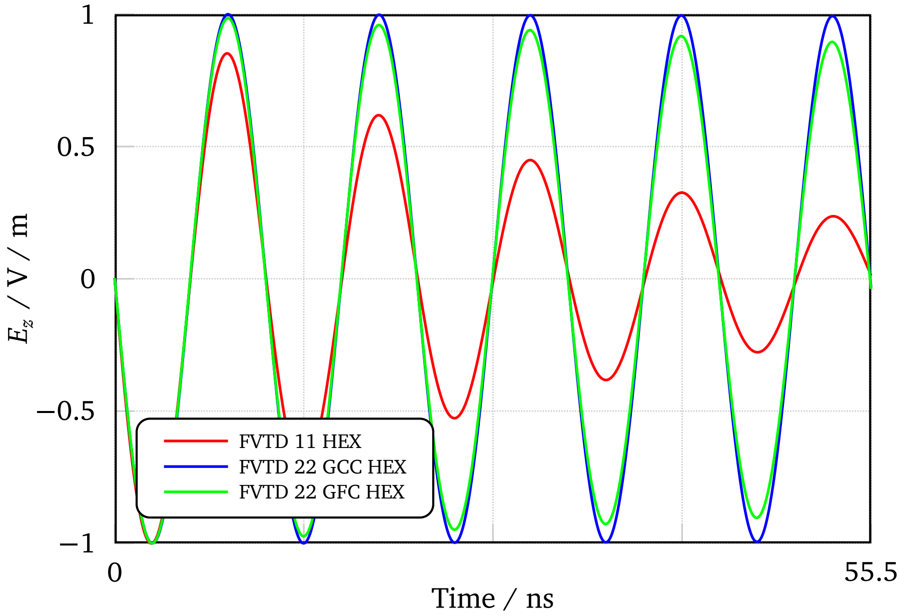

Figure 3.2: The fundamental mode is imposed as the initial condition and allowed to oscillate freely for 5 cycles. The electric field component E_z at the center of the box resonator is depicted using first and second order FVTD methods (Gradient calculated from Cell Center values and Gradient calculated from Face Center values) on hexahedral mesh.

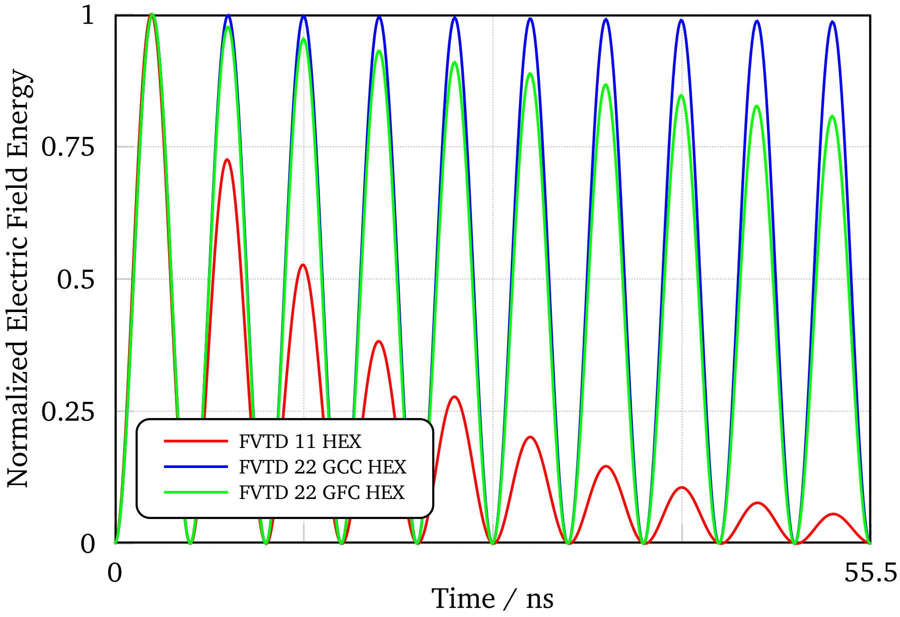

Figure 3.3: The observed electric field energy in the box resonator. The decay in the electric field energy is clearly visible for all the three methods. It is maximum in the case of first order method. Second order FVTD method (Gradient calculated from Cell Center values) has minimum decay due to the high accuracy of gradient.

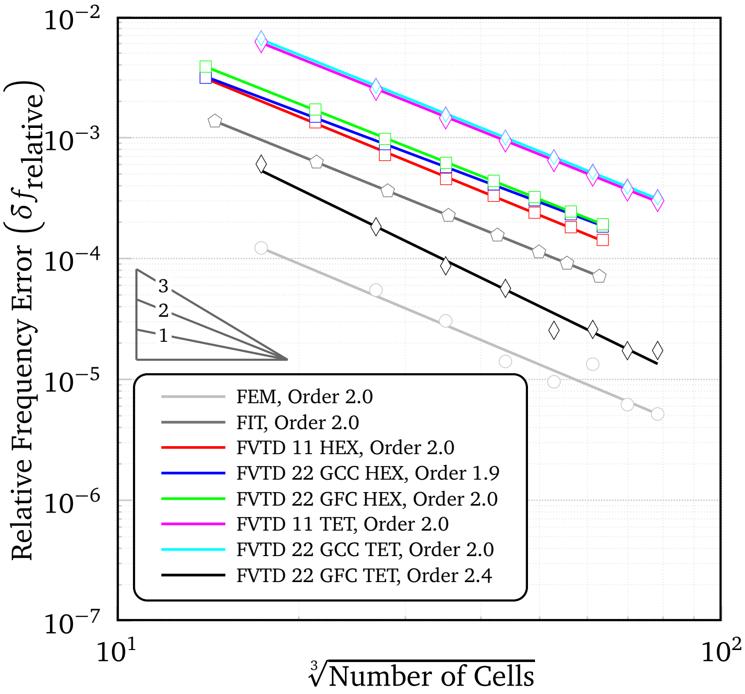

Figure 3.4: Convergence of error in the resonant frequency of the fundamental mode in the box resonator. FEM on tetrahedral mesh has minimum error when compared to all the rest of the methods within the specified spatial resolution range. Convergence orders are furnished in the legend. The diagonals of the right angle triangle indicate the reference orders.

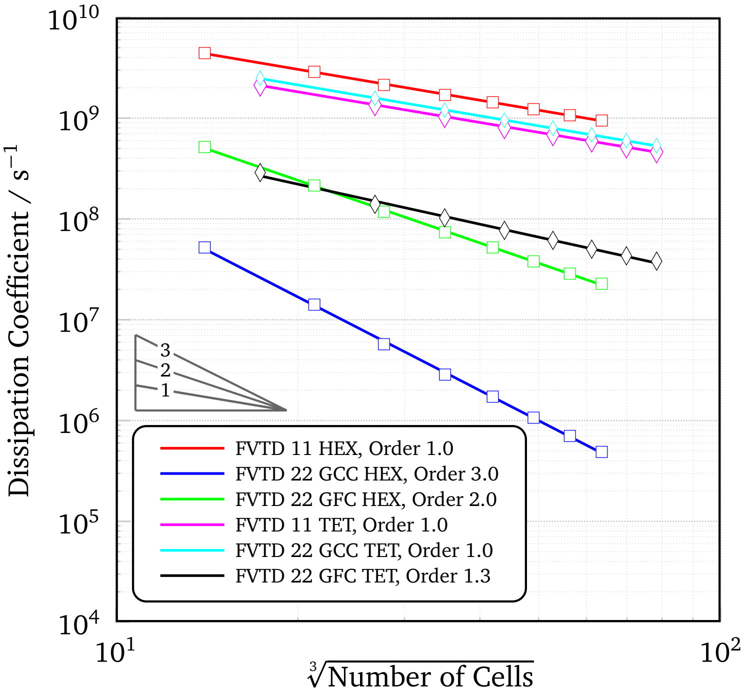

Figure 3.5: Convergence of error in the amplitude of the fundamental mode in the box resonator. FVTD methods on hexahedral mesh have minimum artificial dissipation when compared to FVTD methods on tetrahedral mesh. Convergence orders are furnished in the legend. The diagonals of the right angle triangle indicate the reference orders.

The resonant frequency is also obtained with FIT using the implementation provided in CST MWS. The discretization is changed to 20 CPW from 15 CPW, and the above mentioned procedure is repeated till the spatial resolution reaches 45 CPW in steps of 5 CPW.

The domain is discretized with tetrahedral mesh, with 10 CPW. The resonant frequency and dissipation coefficient are obtained using FVTD methods in a similar manner as previously mentioned for each spatial resolution, from 10 CPW till 45 CPW, in steps of 5 CPW. In addition, FEM is also employed to obtain the resonant frequency for each discretization.

In Figure 3.4, the relative error in frequency or relative frequency error is plotted against cubic root of cells on a loglog scale. Each diamond in red color indicates, a data point, the relative error in resonant frequency obtained using first order FVTD method for a particular discretization. The slope of the curve passing through such data points is nothing but the convergence order of the method provided a homogeneous mesh is applied. One can observe the convergence of different FVTD methods along with FIT and FEM. At the first glance, though it looks like FEM has minimum error when compared to all other methods, one has to keep in mind that this is strongly dependent on the observed mode.

The convergence behavior of the dissipation coefficient (α) is depicted in Figure 3.5. One can observe less artificial dissipation of second order FVTD methods on hexahedral mesh than that on tetrahedral mesh. This is a direct consequence of efficient calculation of gradient on hexahedral mesh when compared to tetrahedral mesh. One has to take note that neither FIT nor FEM has artificial dissipation, hence they are not depicted in Figure 3.5.

An asymmetric ellipsoidal resonator, shown in Figure 3.6(a), with PEC boundary conditions and radius 3 m, 2 m and 1 m in x, y, and z directions is considered. This is obtained from a spherical resonator of radius 1 m, stretched 3 times in x direction and 2 times in y direction. The reference solution is obtained by means of numerical simulations as mentioned before (Page 47). The resonant frequency of the fundamental mode is approximately 57 MHz.

The domain is discretized using a tetrahedral mesh with 10 CPW at 59 MHz. The resonant frequency and the mode pattern of the fundamental mode are obtained employing FEM for this discretization. This mode pattern is imposed as the initial condition for FVTD methods. The electric field component, E_z, is observed at the center of the domain for 5 cycles of oscillation. The resonant frequency and dissipation coefficient are obtained using curve fitting. The discretization is changed and the fundamental mode obtained from FEM eigenmode solver for this discretization is imposed as initial field condition. Again, the resonant frequency and dissipation coefficient are obtained. This process is repeated till 40 CPW in steps of 5 CPW. For all the simulations, the time step is chosen to be the maximum possible value. Figure 3.7 and Figure 3.8 portray the relative error in frequency and dissipation coefficient against cubic root of number of cells in the domain in the loglog scale.

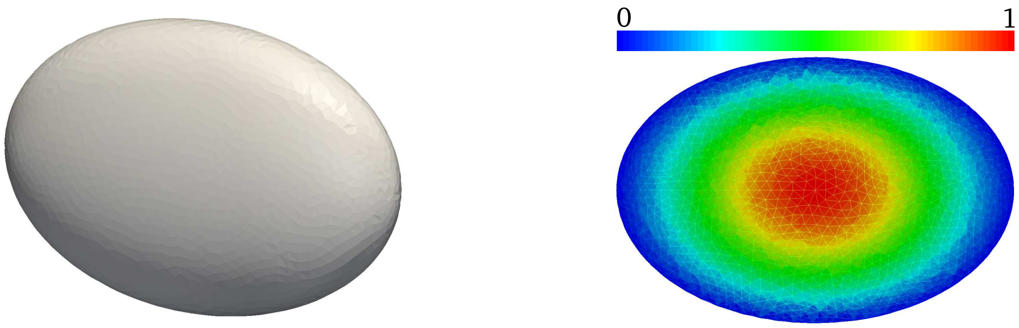

(a) Perspective view of the physical model.

(b) Imposed electric field of the fundamental mode on the plane at $z = 0.5$ m.

Figure 3.6: A Vacuum filled asymmetric ellipsoidal resonator immersed in a PEC medium discretized with tetrahedral mesh with 10 CPW. The imposed electric field pattern of the fundamental mode on the plane at $z = 0.5$ m is also illustrated. One can observe the mesh in this plane.

Figure 3.7 depict the convergence of resonant frequencies obtained using different FVTD methods, in addition to FIT and FEM. One can observe that the second order FVTD method (gradient calculated from cell center values) has minimum error when compared to the other methods, in the considered spatial resolution range. The convergence order, on the other hand, is highest for FIT, which means as the spatial resolution is increased, eventually FIT is going to have minimum error when compared to all the rest of the methods.

Figure 3.8 describes the convergence of dissipation coefficient obtained from various FVTD methods. Out of these, the second order FVTD method, where gradient is calculated from face center values, has minimum artificial dissipation. This is because the gradient calculated from face center values is precise compared to the rest of the methods.

FVTD methods on hexahedral mesh are avoided as this requires either staircase meshing or conformal meshing, there by introducing errors into the method.

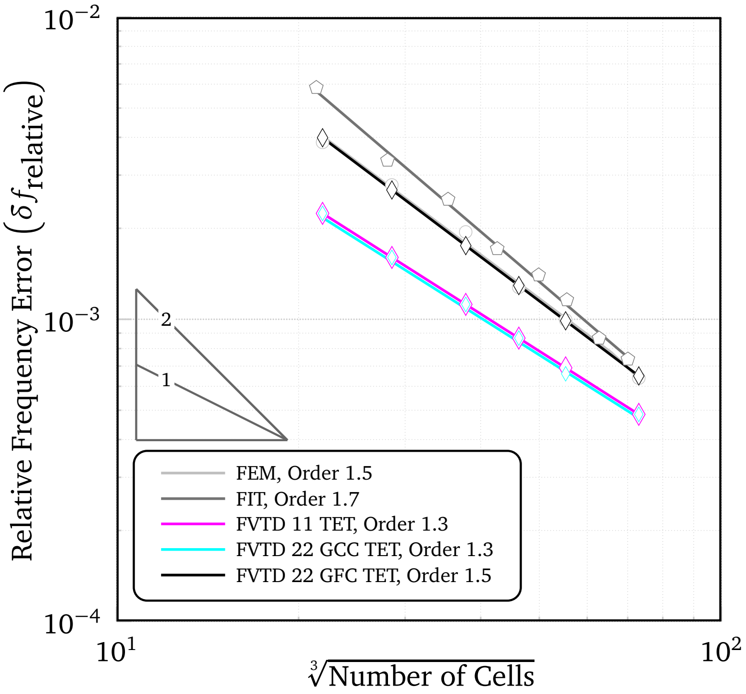

Figure 3.7: Convergence of error in the resonant frequency of the fundamental mode in the asymmetric ellipsoidal resonator. Second order FVTD method (Gradient calculated from Cell Center values) has minimum error within the spatial resolution range. Convergence orders are furnished in the legend. The diagonals of the right angle triangle indicate the reference orders.

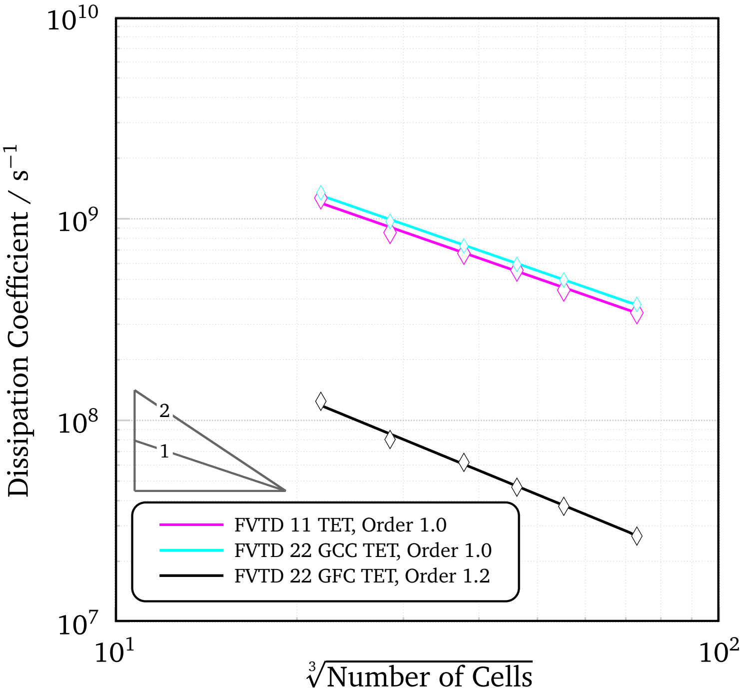

Figure 3.8: Convergence of error in the amplitude of the fundamental mode in the asymmetric ellipsoidal resonator. Second order FVTD method (Gradient calculated from Face Center values) has less artificial dissipation when compared to the rest of the methods. Convergence orders are furnished in the legend. The diagonals of the right angle triangle indicate the reference orders.

3.3 Simple Geometry with Singularity

Consider the box resonator mentioned in Section 3.1 with the origin of the coordinate system shifted to the center of the domain. From this resonator 1/8th of the domain, the portion in the first octant is removed, resulting in a resonator as depicted in Figure 3.9(a).

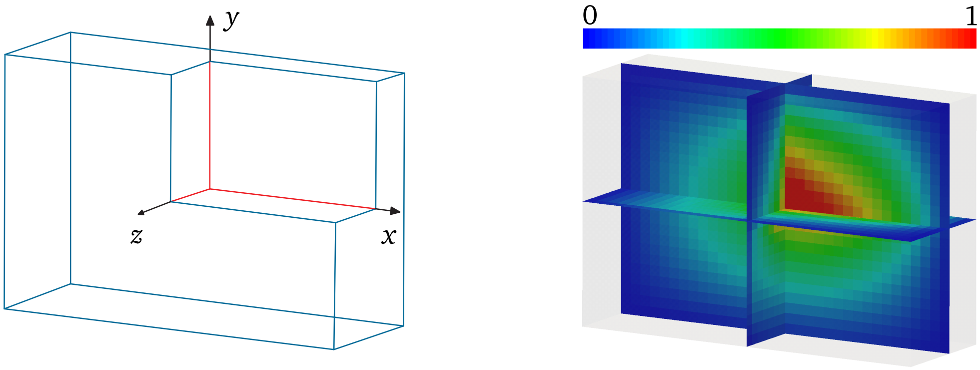

(a) Outline view of the physical model.

(b) Imposed fundamental mode electric field on the planes where discontinuity in the geometry occurs.

Figure 3.9: A Vacuum filled box resonator truncated with PEC walls on all sides highlighting the corner where the singularity in the field due to geometry occurs. The imposed electric field pattern of the fundamental mode, as the initial condition, is also depicted on the planes where the discontinuity in the geometry occurs.

One can observe the singularity, the sharp corner with its 3 edges highlighted in red color. The reference solution is obtained as mentioned in Page 47. The resonant frequency of the fundamental mode is around 85 MHz. The electric field pattern of the fundamental mode is depicted in Figure 3.9(b) on the planes where the discontinuity occurs.

This resonator is discretized with hexahedral mesh with 15 CPW at 87 MHz. The mode pattern obtained from CST MWS eigenmode solver, for this discretization, is imposed as the initial condition. The mode is allowed to oscillate freely for 5 cycles. The field components are recorded at the center of the domain in the 7th octant of the coordinate system. The observed electric field component, E_z, is used to obtain the resonant frequency and the dissipation coefficient. The discretization is changed and the procedure is repeated till the spatial resolution reaches 50 CPW, in steps of 5 CPW.

The domain is discretized with tetrahedral mesh with 10 CPW. FEM eigenmode solver is employed to obtain the mode pattern. This is imposed as the initial field condition for FVTD methods on tetrahedral mesh. The resonant frequency and dissipation coefficient are obtained from recorded electric field component, E_z, employing curve fitting as mentioned before. The spatial resolution is changed till 45 CPW, in steps of 5 CPW and the whole procedure is repeated.

For all the simulations, the Courant number is chosen to be the optimal value. Note that no special treatment to resolve the singularities is introduced for FVTD methods. The convergence of frequency error for various methods is depicted in Figure 3.10. One can observe that the error in frequency is less for FVTD methods on tetrahedral mesh than that of FVTD methods on hexahedral mesh. This is mainly due to the fact that the meshing is fine around the discontinuity in tetrahedral mesh as compared to hexahedral mesh. One can also note that FIT is the winner in resolving the singularity among these methods.

The first glance at Figure 3.11 illustrates that the error is minimum for the second order FVTD method where the gradient is calculated from cell center values, on the hexahedral mesh. But one has to keep in mind that the convergence order of this is less than that of the second order FVTD method where gradient is calculated from face center values i.e., as the spatial resolution increases the error in second order FVTD method (gradient calculated from cell center values) will be more when compared to the second order FVTD method with gradient calculated from face center values. Keeping the error and convergence order in view, one can infer that the precision of gradient is best if it is calculated from face center values on both hexahedral and tetrahedral meshes.

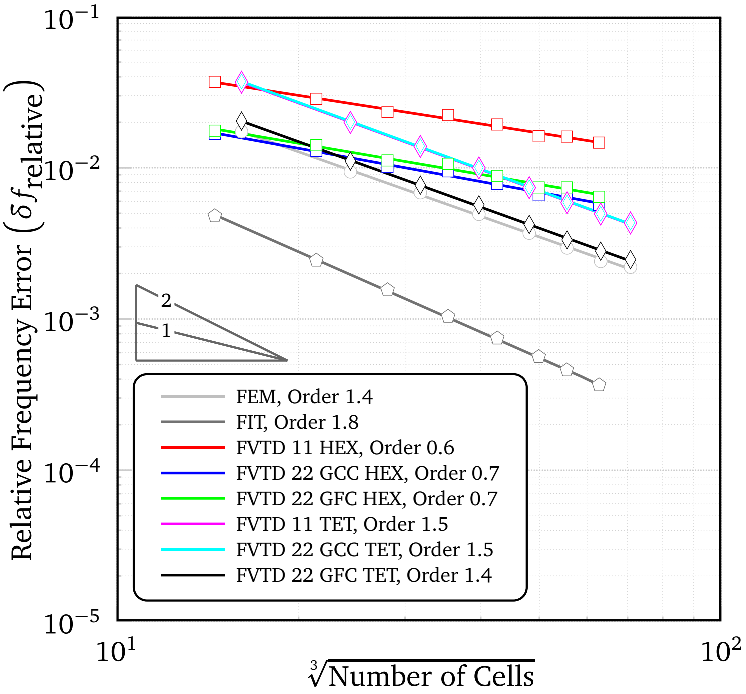

Figure 3.10: Convergence of error in the resonant frequency of the fundamental mode in the box resonator with singularity. FIT has minimum error when compared to all the rest of the methods. Convergence orders are furnished in the legend. The diagonals of the right angle triangle indicate the reference orders.

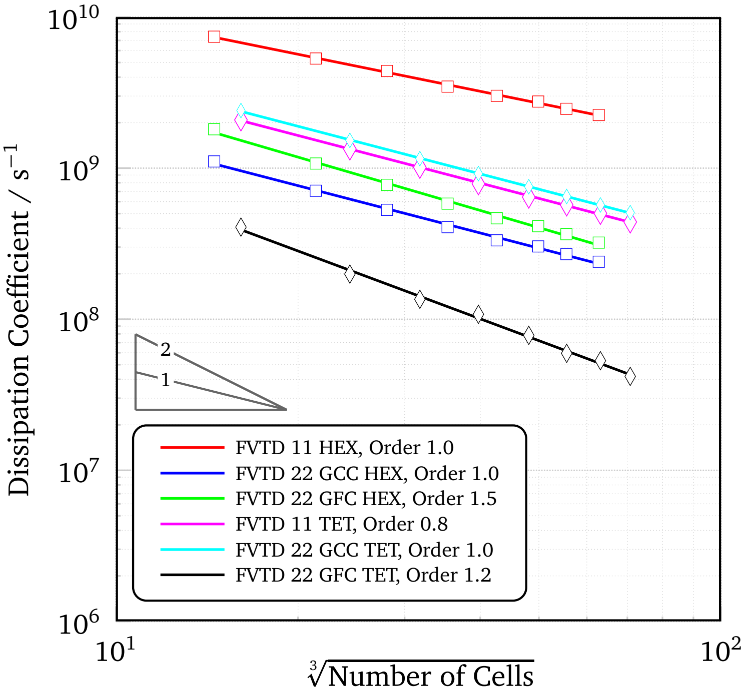

Figure 3.11: Convergence of error in the amplitude of the fundamental mode in the box resonator with singularity. The error is minimum for the second order FVTD method if the Gradient is calculated from Face Center values. Convergence orders are furnished in the legend. The diagonals of the right angle triangle indicate the reference orders.

3.4 Complex Geometry with Singularity

Consider a spherical resonator surrounded by PEC medium and radius 1 m with the center at the origin of the coordinate system. The portion in the first octant, is also filled with PEC material. Figure 3.12(a) depicts the physical model with PEC region excluded. This model has a singularity in addition to a curved surface. Reference solution is obtained as mentioned before (Page 47). The resonant frequency of the fundamental mode is approximately at 1 GHz.

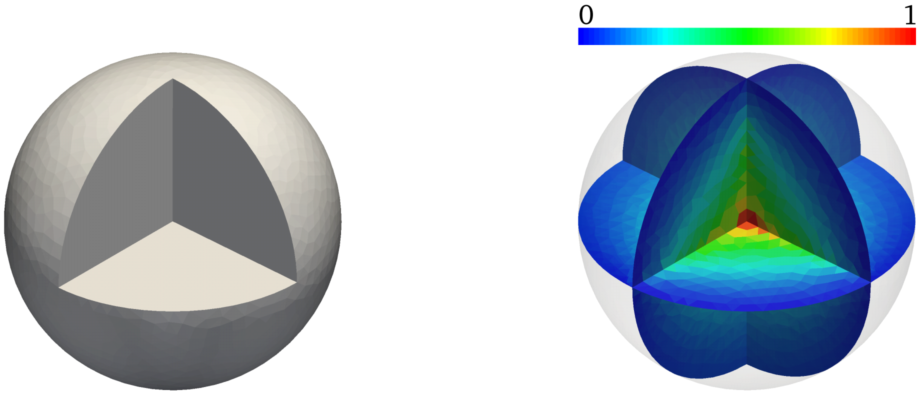

(a) Perspective view of the physical model.

(b) Imposed fundamental mode electric field on the planes where discontinuity in the geometry occurs.

Figure 3.12: A spherical resonator with a singularity surrounded by PEC medium along with the imposed electric field pattern of the fundamental mode on the planes where discontinuity in geometry occurs.

The resonator is discretized with tetrahedral mesh with 15 CPW at 1.1 GHz. The mode pattern obtained from FEM eigenmode solver, for the same discretization, is imposed as the initial condition for FVTD methods. Figure 3.12(b) shows the electric field pattern of the fundamental mode on the planes where the discontinuity in the geometry occurs. The field component, E_z, is recorded at the radial center of the domain in the 7th octant of the coordinate system for 5 cycles of oscillation and is used to obtain the resonant frequency and the dissipation coefficient. The discretization is changed and the procedure is repeated, till the spatial resolution reaches 45 CPW, in steps of 5 CPW. For all the methods, the time step is chosen to be the maximum possible value.

Figure 3.13 depicts the convergence of relative frequency error for various methods. One can notice that FIT with PBA is more successful to resolve the singularity and curved surface than any other method considered. One has to keep in mind that no special treatment to resolve the singularities is introduced for FVTD methods whereas this is not the case for FIT. From Figure 3.13, one can conclude that the second order FVTD method with gradient calculated from face center values has minimum error when compared to the second order FVTD method with gradient calculated from cell center values.

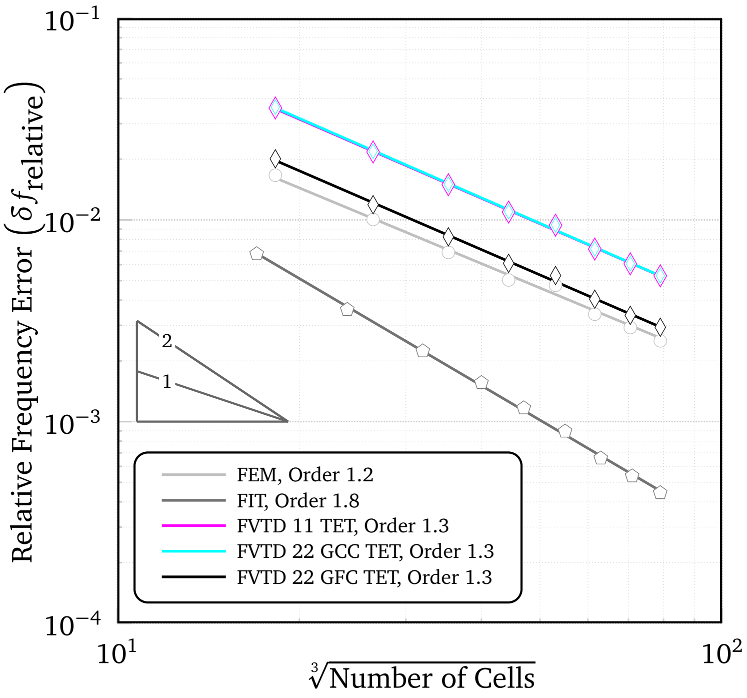

Figure 3.13: Convergence of error in the resonant frequency of the fundamental mode in the spherical resonator with singularity. FIT succeeds in resolving the curved surface and singularity more efficiently than the rest of the methods. Convergence orders are furnished in the legend. The diagonals of the right angle triangle indicate the reference orders.

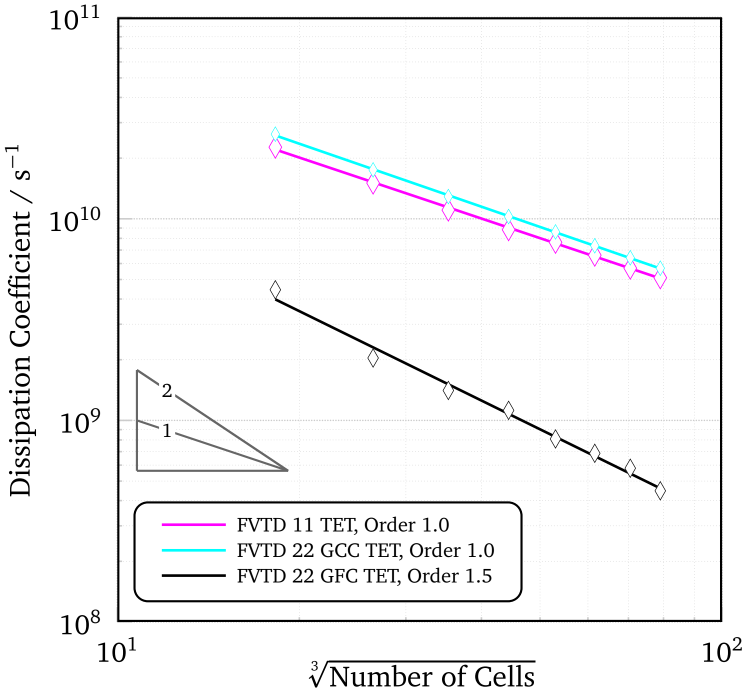

Figure 3.14: Convergence of error in the amplitude of the fundamental mode in the spherical resonator with singularity. Second order FVTD method with Gradient calculated from Face Center values has minimum artificial dissipation when compared to the rest of FVTD methods. Convergence orders are furnished in the legend. The diagonals of the right angle triangle indicate the reference orders.

4 Applications

Abstract *– This chapter inspects the capabilities of finite volume time domain methods to model real word problems. Four applications are chosen e.g., a coaxial cable with a very high contrast of materials, to demonstrate the tractability of finite volume time domain methods. The results are bidden against the solutions obtained from the finite integration technique and the finite element method.*

The first application is a simple waveguide filter with homogeneous material distribution and singularities. The second example, a coaxial filter, consists of homogeneous material distribution, singularities and curved surfaces. The coaxial cable, third application, has non–uniform material distribution (contrast of materials is so high that the velocity of light is reduced by a factor of 10) along with curved surfaces. There are no singularities present. The final application, the coaxial connector, has non–uniform material distribution, singularities and curved surfaces.

The S–parameters are extracted for all these applications using various second order upwind flux FVTD methods (first order method is avoided owing to high artificial dissipation) along with FIT TD, FIT FD and FEM FD. The convergence of the solutions (S–parameters) obtained from all these methods is presented. In order to perform a convergence study, one has to obtain the reference solution.

Obtaining the Reference Solution: The computational domain is discretized with a coarse hexahedral mesh and the S–parameters are extracted from CST MWS transient solver (FIT TD). The mesh is refined and the S–parameters are computed again. This process is repeated till the minimum absolute difference between any two consecutive solutions (S–parameters) falls below 10 per million in the complex plane. The solution found with finer mesh among these two is considered as the reference solution from FIT TD. For clarity, say, the minimum absolute difference between S_{11} acquired with 10 CPW resolution and 20 CPW resolution in the complex plane falls below 10 per million then S_{11} figured with 20 CPW resolution is chosen as the reference solution from FIT TD.

The reference solutions are also worked out using CST MWS frequency domain solver employing FIT FD (on hexahedral mesh) and FEM FD (on tetrahedral mesh) following exactly the same procedure as above.

The reference solutions from FIT TD, FIT FD and FEM FD are compared. Again, if the difference between them lies around 10 per million, then the solution from FIT TD or FIT FD is considered as the reference solution.

4.1 Waveguide Filter

The waveguide filter considered here is a concatenation of different waveguides end to end as shown in Figure 4.1. The device is located in the first octant of the coordinate system. The open ends of the waveguides are aligned along the centers, parallel to the z axis. The dimensions are depicted in Figure 4.1(b) and Figure 4.1(c). The structure is truncated with PEC boundaries in x and y directions. There are two ports located at both the ends of the device in the z direction; port 1, $p1$, in $-z$ direction and port 2, $p2$, in the $+z$ direction. Only $p2$ is depicted in Figure 4.1(a) in red color. Clearly the fundamental port mode in this structure is TE_{10} mode, cutoff frequency being approximately 1.5 GHz. The field pattern can be described as [53]:

$$E_x\left(x,y,z\right) = \frac{j\omega\mu}{\gamma^2+k^2}\frac{n\pi}{b}H_0\cos\left(\frac{m\pi}{a}x\right)\sin\left(\frac{n\pi}{b}y\right)e^{-\gamma z} \tag{4.1}$$

$$E_y\left(x,y,z\right) = \frac{-j\omega\mu}{\gamma^2+k^2}\frac{m\pi}{a}H_0\sin\left(\frac{m\pi}{a}x\right)\cos\left(\frac{n\pi}{b}y\right)e^{-\gamma z} \tag{4.2}$$

$$E_z\left(x,y,z\right) = 0 \tag{4.3}$$

$$H_x(x,y,z) = \frac{\gamma}{\gamma^2+k^2}\frac{m\pi}{a}H_0 \sin\left(\frac{m\pi}{a}x\right)\cos\left(\frac{n\pi}{b}y\right)e^{-\gamma z} \tag{4.4}$$
$$H_y(x,y,z) = \frac{\gamma}{\gamma^2+k^2}\frac{n\pi}{b}H_0 \cos\left(\frac{m\pi}{a}x\right)\sin\left(\frac{n\pi}{b}y\right)e^{-\gamma z} \tag{4.5}$$
$$H_z(x,y,z) = H_0 \cos\left(\frac{m\pi}{a}x\right)\cos\left(\frac{n\pi}{b}y\right)e^{-\gamma z} \tag{4.6}$$

where a, b are dimensions and m, n are the number of half cycles in x and y directions, respectively. The propagation constant and wave number are denoted as γ and k, ω being the angular frequency. The amplitude of magnetic field is denoted by H_0.

The structure is discretized with hexahedral mesh, with 20 CPW and stimulated with TE$_{10}$ mode at $p1$ by analytical means. In other words, the analytical TE$_{10}$ mode is imposed on the face centers of $p1$. The mode pattern is depicted in Figure 4.2.

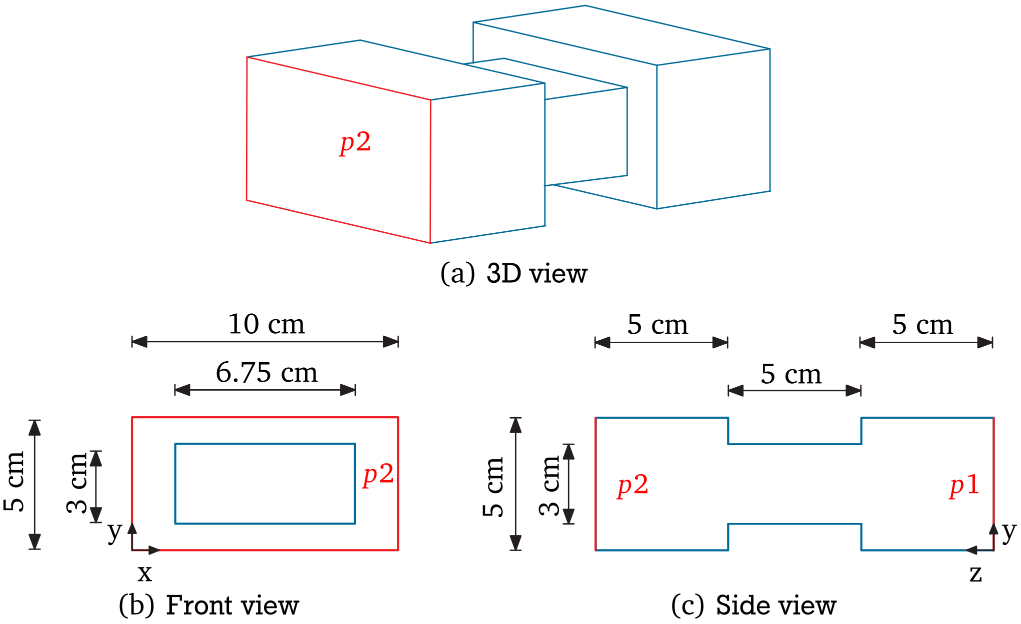

Figure 4.1: The outline view of the Vacuum filled waveguide filter truncated with PEC boundaries in x and y directions. The two ports located in z direction are highlighted in red color.

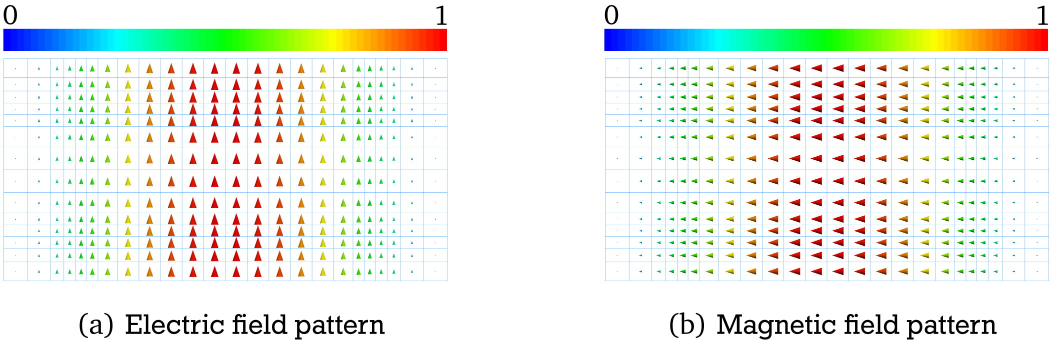

(a) Electric field pattern

(b) Magnetic field pattern

Figure 4.2: Imposed electric and magnetic field patterns of the fundamental mode (TE$_{10}$) at port 1, when the domain is discretized with hexahedral mesh at a resolution of 15 CPW at 3 GHz.

A Gaussian pulse with dominant frequency spectrum between 2–3 GHz, depicted in Figure 4.4(b) in red color, is transformed into time domain using an inverse Fourier transformation, resulting in a time signal as depicted in Figure 4.4(a) in red color. This signal is used to excite the electric field components of the imposed mode pattern. In a structure like this there is no linear relation between electric and magnetic fields. In other words, the impedance is a function of frequency. Figure 4.3 displays the impedance normalized to the free space impedance in the frequency range 2–3 GHz. This non–linear property of the impedance defines the spectrum of the magnetic field components excitation signal. The temporal pattern of this (blue color) is used to excite the magnetic field components, depicted in Figure 4.4(a). The difference between the electric and magnetic field excitations is a direct result of non–linearity of the impedance in the waveguide.

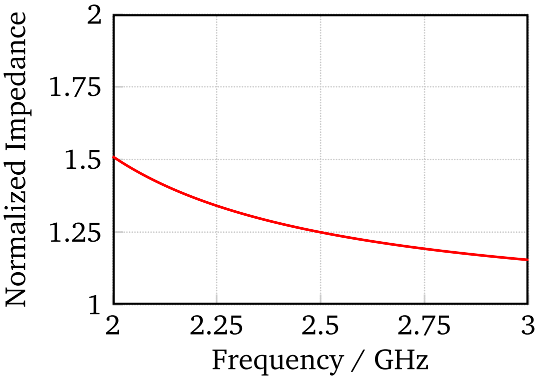

Figure 4.3: TE_{10} mode impedance normalized to free space impedance in the waveguide filter. One can observe the non-linear relation between the impedance and frequency. At extremely higher frequencies the relation is linear again. In other words, at these frequencies the mode impedance becomes free space impedance.

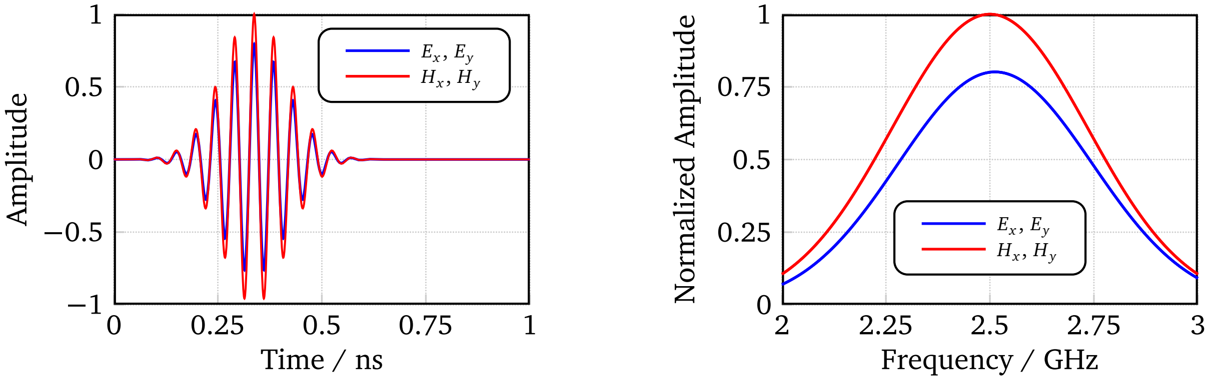

Figure 4.4: Time and frequency domain representations of the waveguide filter excitation. The difference between the excitation signals, both in amplitude and phase, used to excite the electric and magnetic field components, is a direct consequence of non-linear behavior of the mode impedance.

In order to compute the S–parameters, the ports should be truncated with absorbing boundaries. However, in order to eliminate the errors introduced by absorbing boundary conditions, the waveguide is extended on both sides such that during the simulation there are no reflections from the ports.

The mode pattern is modulated with the temporal patterns presented in Figure 4.4 and propagated through the structure. The S–parameters are extracted using both the second order FVTD methods.

The S–parameters are also obtained using FIT TD and FIT FD for the same spatial resolution. The domain is discretized with spatial resolution of 30 CPW and the procedure is repeated till the desired accuracy limit of –40 dB is reached in steps of 10 CPW. The computational domain is discretized with tetrahedral meshes (spatial resolution from 5 CPW till 11 CPW) and the S–parameters are obtained using second order FVTD methods in addition to FEM FD for each spatial resolution. The time step value is optimal for all the methods employed at all spatial resolutions.

The S–parameters obtained using second order FVTD method with gradient calculated from cell center values on hexahedral mesh (FVTD 22 GCC HEX) are depicted in Figure 4.5(a) and Figure 4.5(b) in the complex plane for various resolutions. One can also find the magnitude and phases in the subsequent plots. In all these figures, the red dotted line represents the chosen reference solution, FIT TD at a spatial resolution of 200 CPW. One can observe that FVTD solutions are converging towards the reference solution.

The minimum of the absolute difference between the S–parameters in the complex plane obtained using FVTD methods and FIT TD (both sampled at the same frequency points) is plotted against cubic root of cells in Figure 4.6 and Figure 4.7. In other words, each red square in Figure 4.6 represents the minimum absolute difference in the complex plane between the S_{11} obtained using second order FVTD method (gradient calculated from cell center values) on hexahedral mesh for some particular spatial resolution and FIT TD with spatial resolution 200. In a loglog scale, a curve passing through such points indicates the convergence of the method. The convergence of solution using various methods is depicted in Figure 4.6 and Figure 4.7. One can find the convergence order of each method in the legend.

At the first glimpse it looks like FEM FD has least error. But as the spatial resolution increases, FIT surpasses FEM in terms of minimum error. FVTD methods on tetrahedral mesh have minimum error when compared to FVTD methods on hexahedral mesh. This owes to the fact that when discretized with same resolution, a tetrahedral mesh is finer than the hexahedral mesh. Practically it is almost impossible to get the same number of mesh cells using hexahedral and tetrahedral meshes.

Another interesting feature is that second order FVTD method with gradient calculated from cell center values has more error than that of second order FVTD method with gradient calculated from face center values, even in the case of the hexahedral mesh. This is a direct consequence of inefficient calculation of gradient in the case of former method when compared to the later. In the case of S_{11}, the solution calculated using second order method using gradient calculated from cell center values seems not to be converging (denoted by “$*$” in the legend) within these spatial resolutions. The solutions from FEM also seem to be not converging within the mentioned spatial resolutions as shown in Figure 4.7.

One can conclude that FIT TD has better convergence than any other method. The error in FVTD methods is more when compared to other methods irrespective of the mesh employed. This reiterates the fact that for simple Cartesian models FIT is better suited than any other method while considering accuracy, complexity and simulation time.

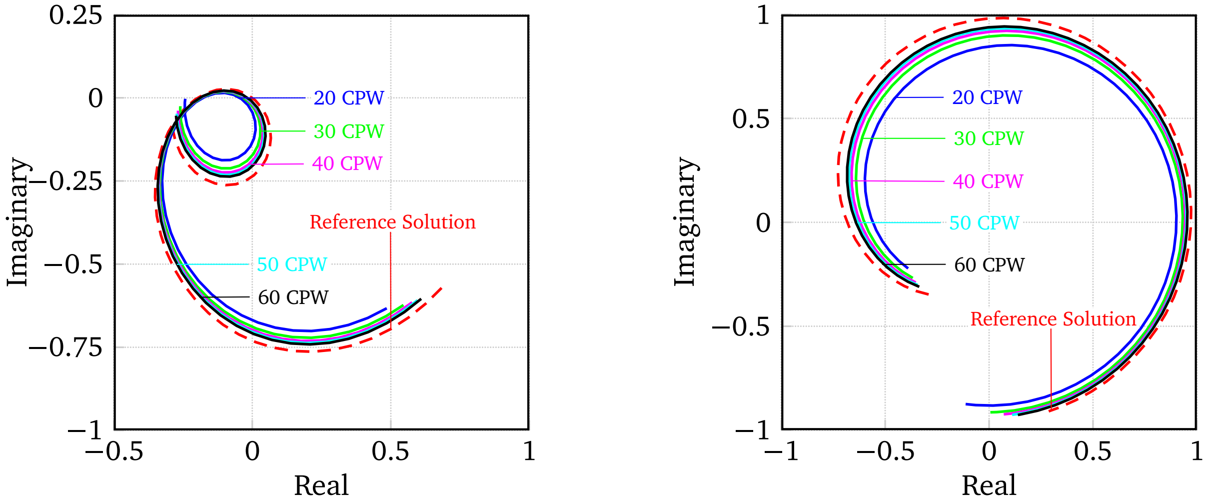

(a) S_{11} in complex plane.

(b) S_{21} in complex plane.

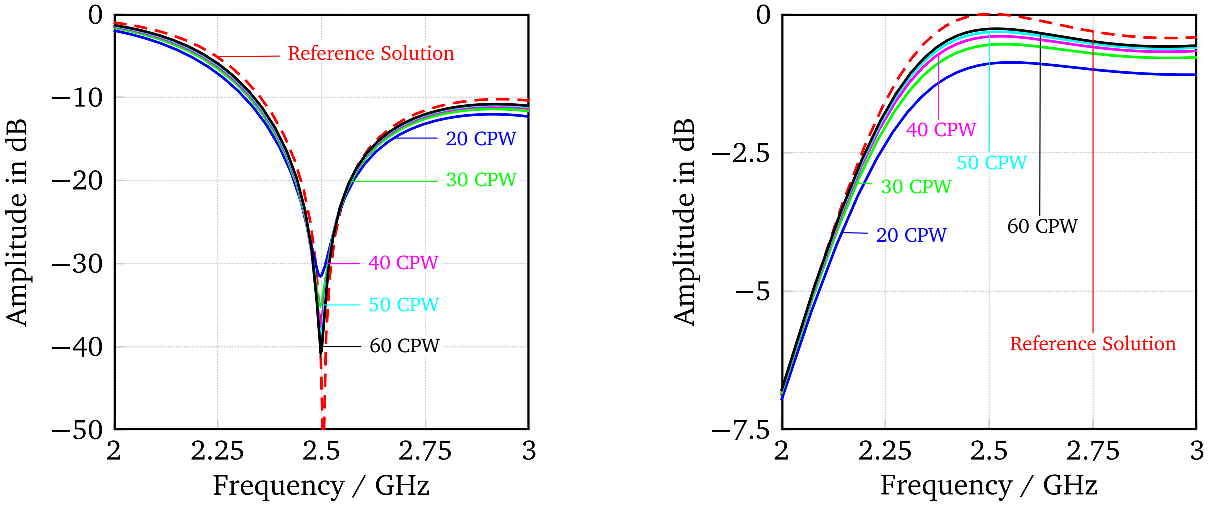

(c) S_{11} Magnitude.

(d) S_{21} Magnitude.

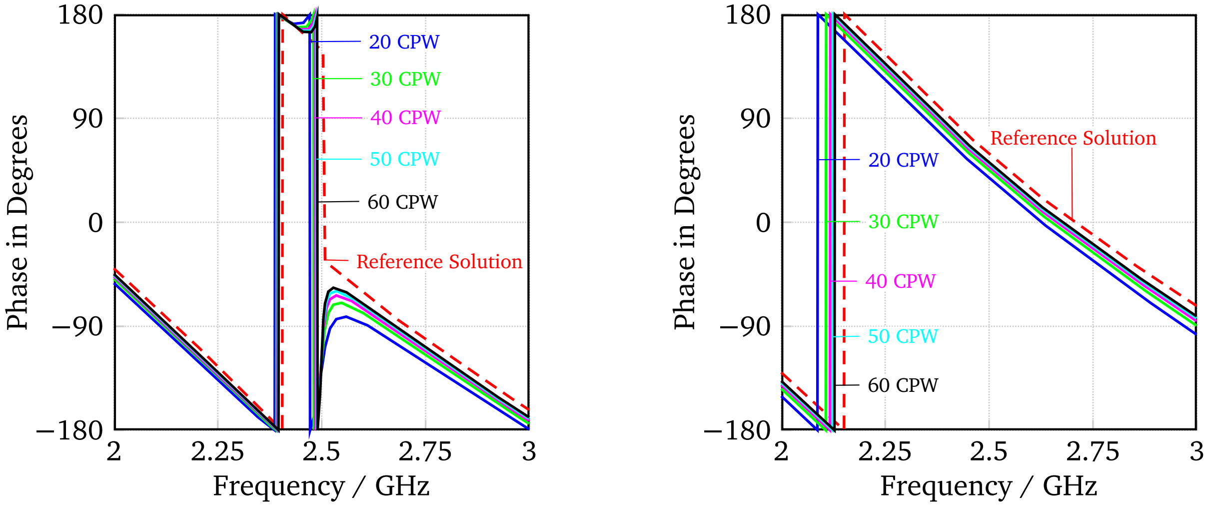

(e) S_{11} Phase.

(f) S_{21} Phase.

Figure 4.5: The S-parameters of the waveguide filter obtained using second order FVTD method (Gradient calculated from Cell Center values), for various spatial resolutions on hexahedral mesh. The set of S-parameters obtained from FIT TD on hexahedral mesh at a resolution of 200 CPW is considered as the reference solution.

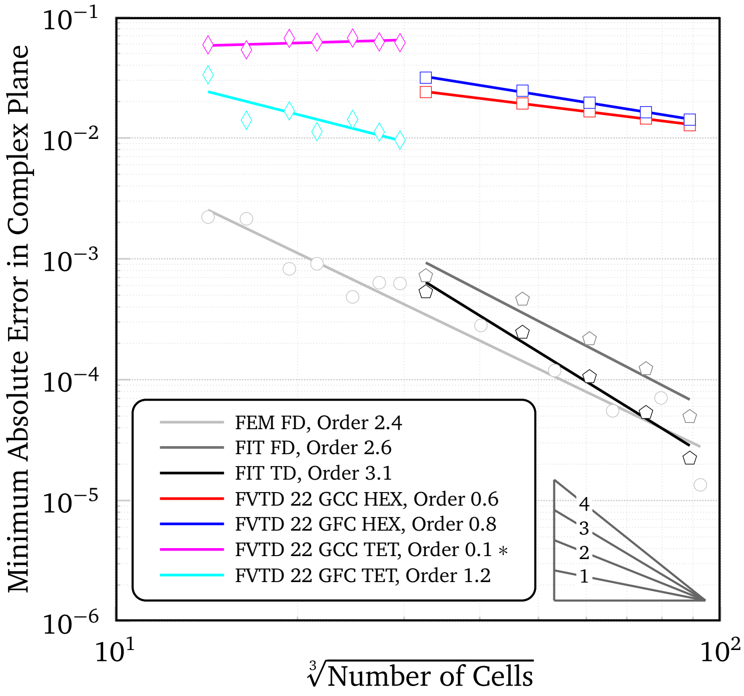

Figure 4.6: Convergence of error in S_{11} of the waveguide filter. One can observe that FIT TD has better convergence order and surpasses FEM in terms of the minimum error as spatial resolution increases. Convergence orders are furnished in the legend. The diagonals of the right angle triangle indicate the reference orders. "∗" in the legend indicates the "non-convergent" behavior in the mentioned spatial resolution range.

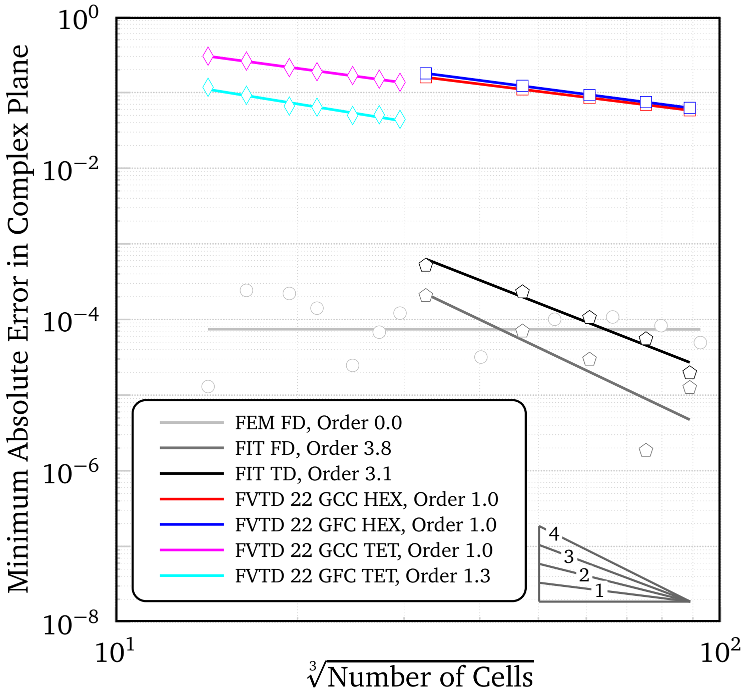

Figure 4.7: Convergence of error in S_{21} of the waveguide filter. Irrespective of the mesh employed one can notice that all FVTD methods have more error compared to FIT and FEM. Convergence orders are furnished in the legend. The diagonals of the right angle triangle indicate the reference orders.

4.2 Coaxial Filter

Three coaxial cables are joined end to end, aligned along the centers as shown in Figure 4.8. The inner radius of all the three cables is the same, the outer radius being different. The parametric information is given in Figure 4.8(b) and Figure 4.8(c). The model is centered along the z axis as shown. The space surrounding the model in x and y directions is PEC. Port 1, $p1$, is located in $-z$ direction and port 2, $p2$, is located in $+z$ direction. $p2$ is outlined in red color in Figure 4.8(a).

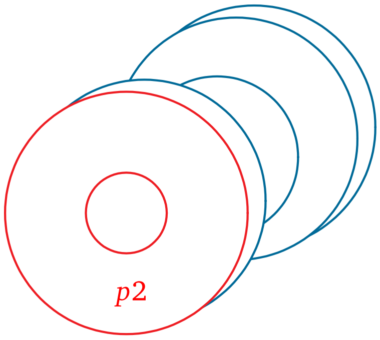

(a) 3D view

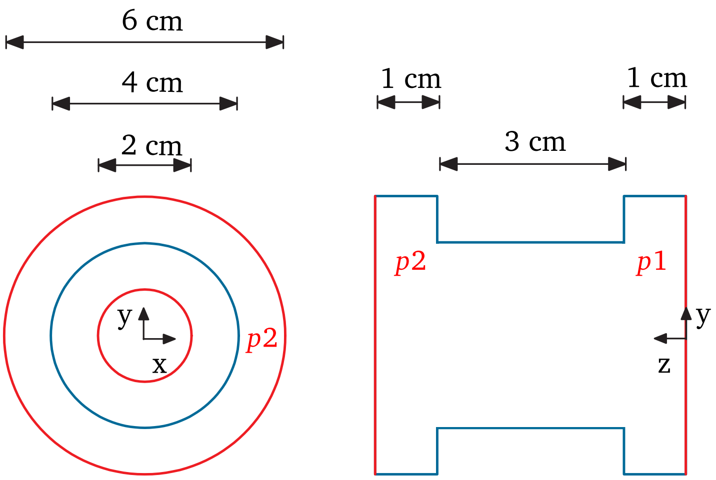

(b) Front view (c) Side view

Figure 4.8: A coaxial filter in different views along with parametric description. The domain is truncated with port planes in z direction and with PEC medium else where. The ports planes are outlined in red color.

The fundamental mode in a coaxial cable is a TEM mode. In cylindrical coordinates, this can be expressed as follows [95]:

$$E_\rho = -\frac{1}{\rho} \tag{4.7}$$

$$E_\varphi = 0 \tag{4.8}$$

$$E_z = 0 \tag{4.9}$$

$$H_\rho = 0 \tag{4.10}$$

$$H_\varphi = \frac{1}{\rho} \tag{4.11}$$

$$H_z = 0 \tag{4.12}$$

In the previous equations ρ represents the radial distance. The structure is discretized with tetrahedral mesh with 10 CPW at 5 GHz and the fundamental mode is imposed on the mesh at port 1. The absence of ω in the above equations indicates the linear relation between electric and magnetic fields. In other words, the impedance is independent of the frequency for the TEM mode. This structure is stimulated using a broadband Gaussian pulse with dominant frequency spectrum between 3–5 GHz.

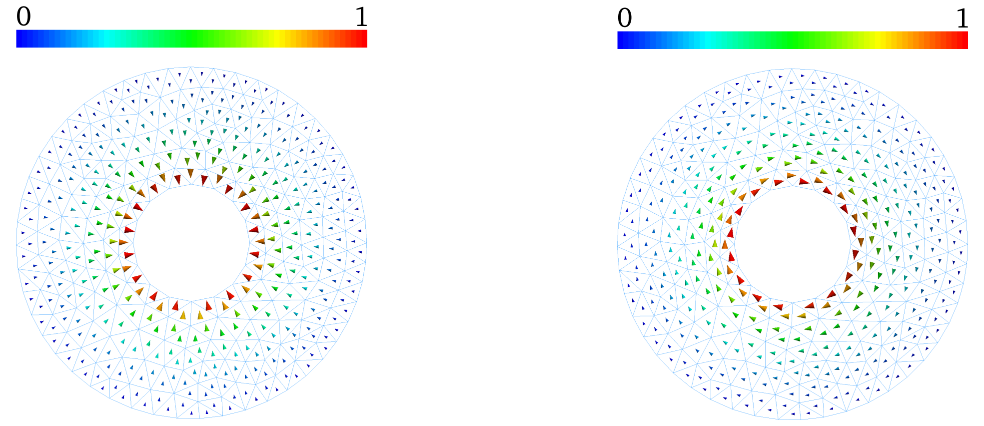

(a) Normalized electric field pattern (b) Normalized magnetic field pattern

Figure 4.9: Imposed electric and magnetic field patterns of the fundamental mode (TEM) at the excitation port when the domain is discretized with tetrahedral mesh at a resolution of 10 CPW at 5 GHz.

Figure 4.9 depicts the imposed field pattern at port 1. The temporal excitation and the corresponding frequency domain representation are depicted in Figure 4.10. Note that both electric and magnetic field components at the port are excited with the same excitation signal because of the linear relation between electric and magnetic field components for this mode.

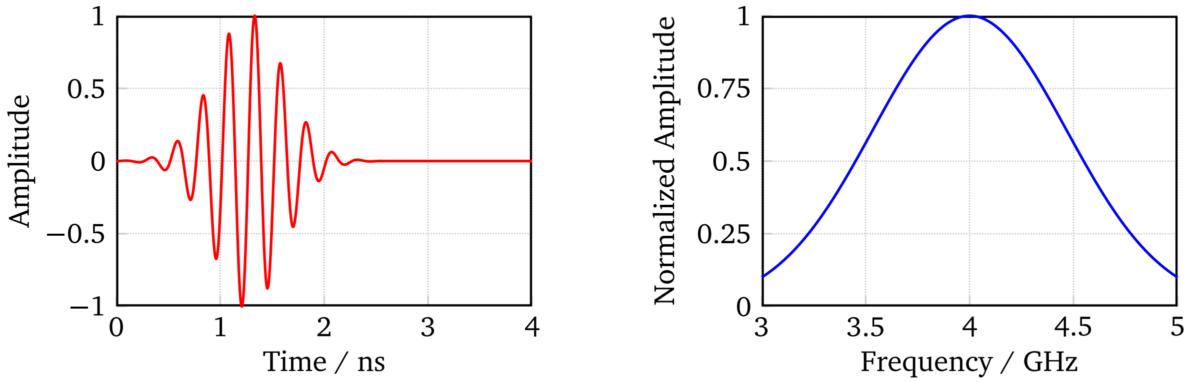

Figure 4.10: Time and frequency domain representations of coaxial filter excitation. As the TEM mode impedance is linear the same excitation signal is used for both electric and magnetic field components.

Figure 4.11(a) and Figure 4.11(b) depict the S–parameters extracted using second order FVTD method with gradient calculated from face center values, for various resolutions (10 CPW till 30 CPW, in steps of 5 CPW). The magnitude and phase plots of the S–parameters are also furnished in Figure 4.11. The S–parameters are also obtained using second order FVTD method with gradient calculated from cell center values in addition to FEM for specified spatial resolutions.

FIT TD with PBA and FIT FD with PBA are also employed to find S–parameters at various spatial resolutions (10 CPW till 30 CPW, in steps of 5 CPW). The S–parameters obtained using FIT FD at a spatial resolution of 100 CPW is considered as the reference solution. The Courant number is kept to be optimal for all the simulations. The convergence of error in the solutions obtained using various methods is depicted in Figure 4.12 and Figure 4.13. The convergence order for each method is furnished in the legend.

One can observe from these plots that FD methods have minimum error and good convergence characteristics when compared to TD methods. In TD methods, second order FVTD method with gradient calculated from face center values on tetrahedral mesh (FVTD 22 GFC TET) outperforms FIT in terms of the error. At the first glance, it seems FIT TD has lesser error than the second order FVTD method with gradient calculated from cell center values (FVTD GCC). But as the mesh resolution increases, the error of second order FVTD method with gradient calculated from cell center values also decreases than that of FIT. To conclude FVTD methods outperform FIT TD in terms of minimum error.

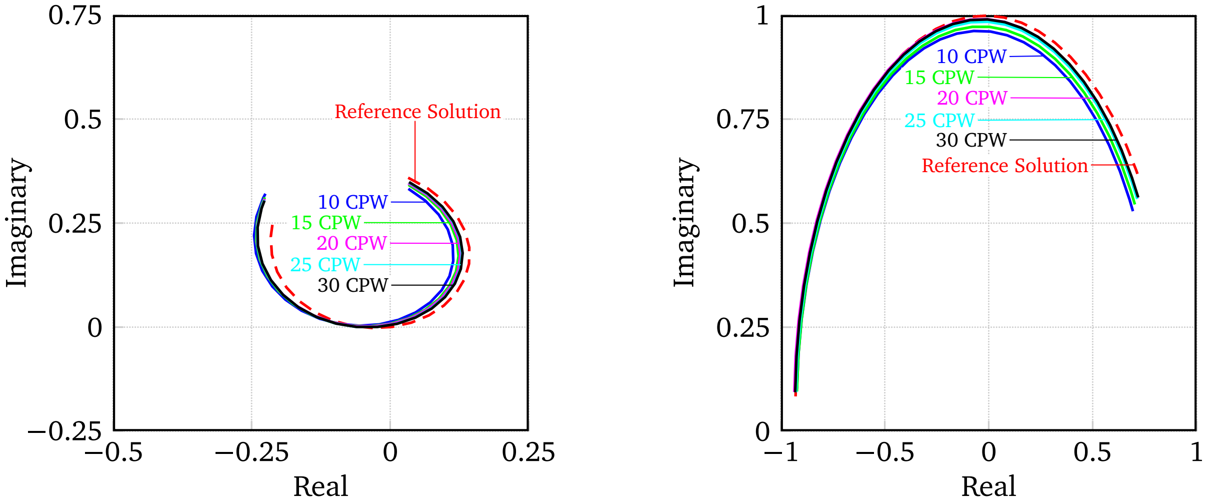

(a) S_{11} in complex plane.

(b) S_{21} in complex plane.

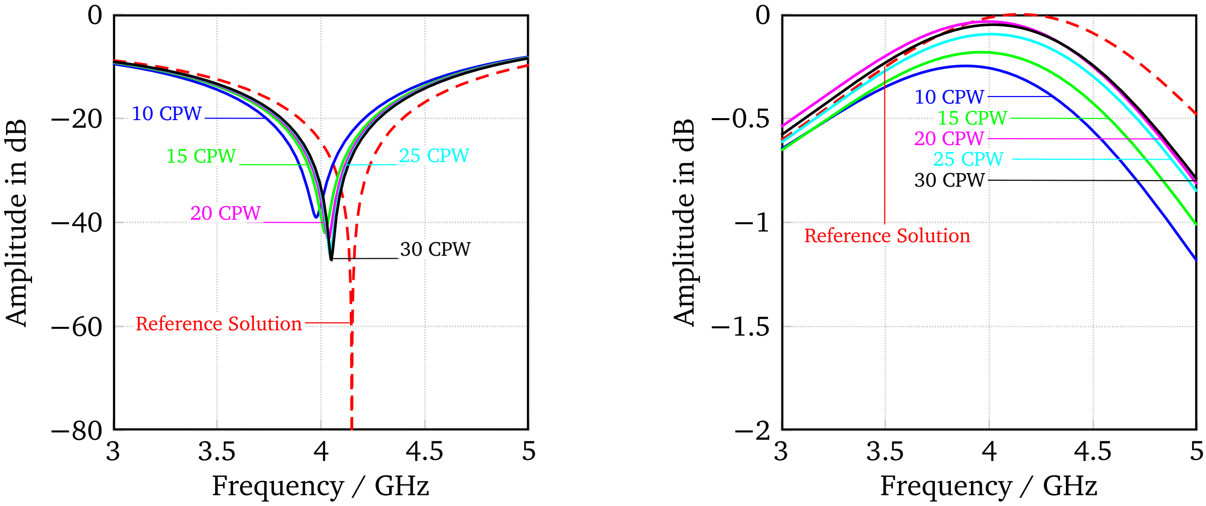

(c) S_{11} Magnitude.

(d) S_{21} Magnitude.

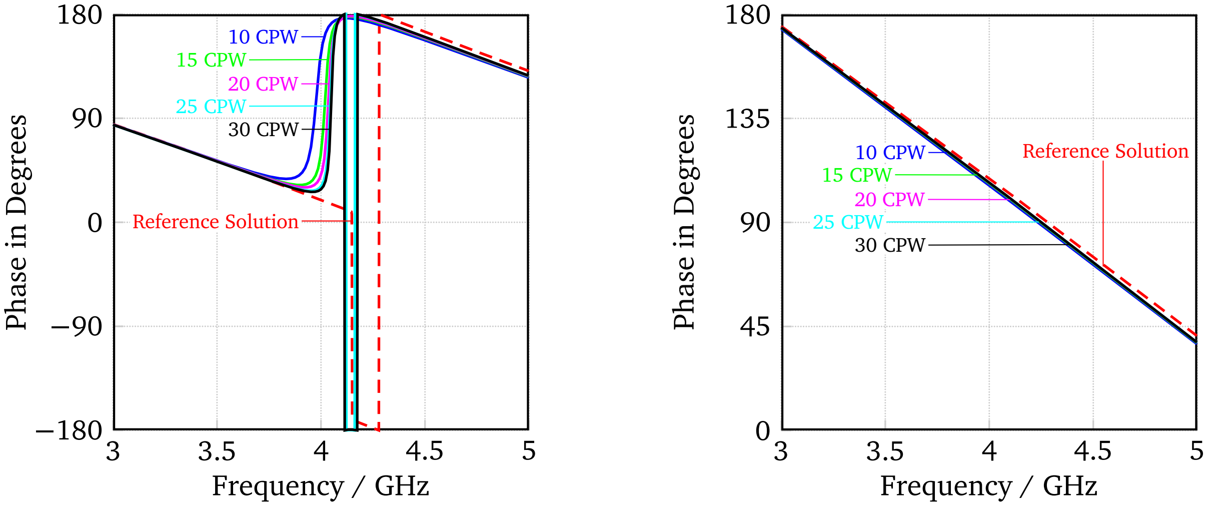

(e) S_{11} Phase.

(f) S_{21} Phase.

Figure 4.11: The S-parameters of the coaxial filter obtained using second order FVTD method (Gradient calculated from Face Center values) for various resolutions on tetrahedral mesh. The set of S-parameters obtained from FIT FD on hexahedral mesh at a resolution of 100 CPW is considered as the reference solution.

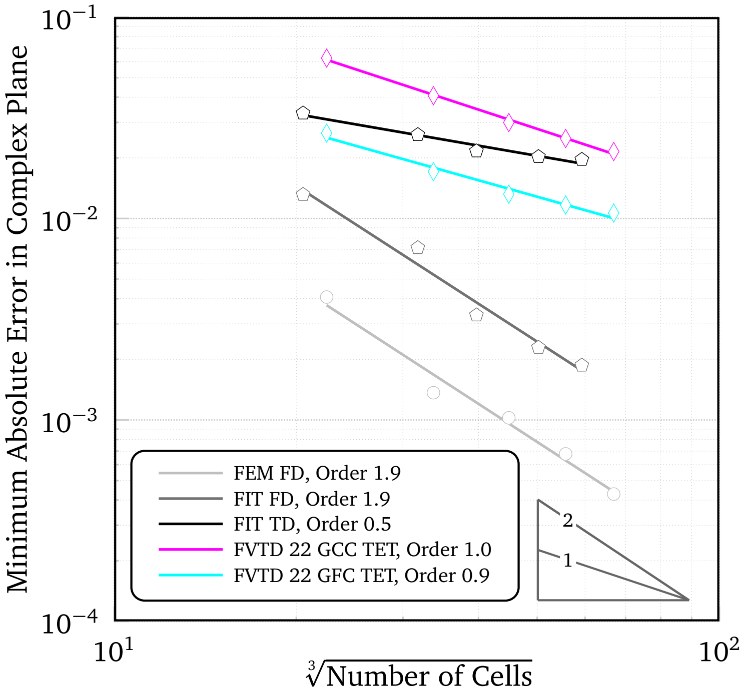

Figure 4.12: Convergence of error in S_{11} of coaxial filter. One can observe that FEM FD has minimum error compared to all the rest of the methods. FVTD methods have better convergence orders compared to FIT TD. Convergence orders are furnished in the legend. The diagonals of the right angle triangle indicate the reference orders.

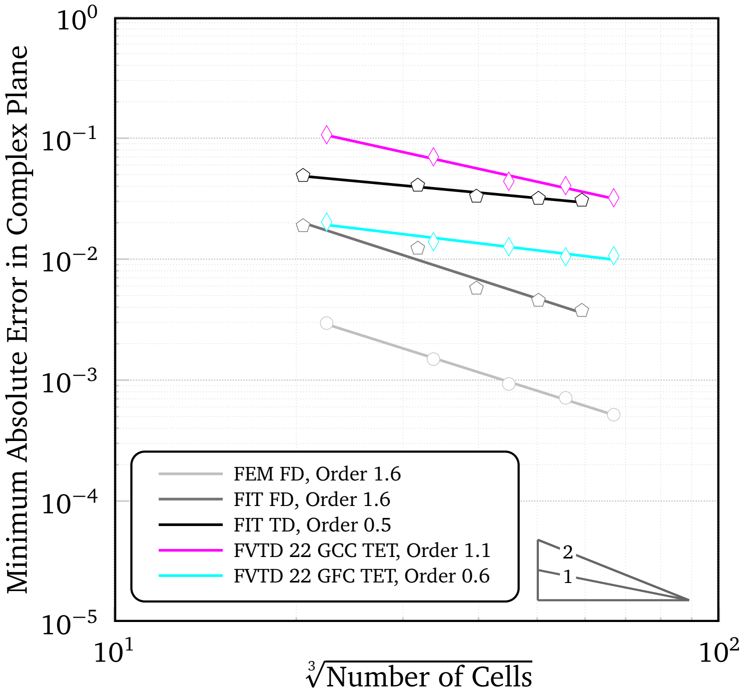

Figure 4.13: Convergence of error in S_{21} of coaxial filter. One can conclude that FEM FD and FIT FD have the same convergence order and FIT FD has minimum error. FVTD methods outperform FIT TD in terms of minimum error, keeping the convergence order in view. Convergence orders are furnished in the legend. The diagonals of the right angle triangle indicate the reference orders.

4.3 Coaxial Cable

This application demonstrates the material modeling capabilities of the FVTD methods. Five coaxial cables with varying material properties are joined end to end as shown in Figure 4.14(a), centers aligned along the z axis. The dimensions of all these cables are the same, and are given in Figure 4.14(b) and Figure 4.14(c). The material properties are also furnished Figure 4.14(c). The cable is surrounded by PEC medium except in the z direction, where ports are located.

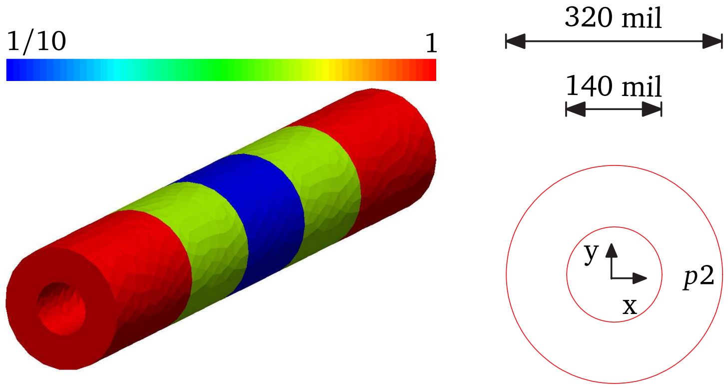

(a) 3D view along with relative velocity profile

(b) Front view

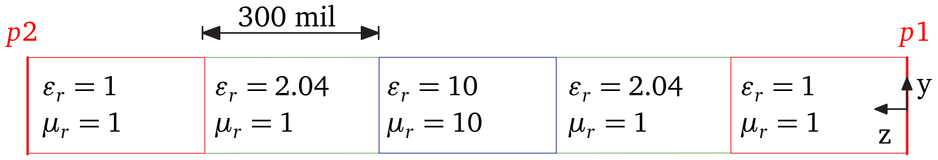

(c) Side view

Figure 4.14: An inhomogeneous coaxial cable with material and parametric description. The ports are located at the extreme ends in z direction. The cable is surrounded by PEC medium else where.

The fundamental mode in this structure is a TEM mode. The field expressions for this mode are mentioned in Page 65. The structure is discretized with tetrahedral mesh with 10 CPW at 8 GHz and the TEM mode is imposed on the mesh at port 1. The port mode is depicted in Figure 4.15.

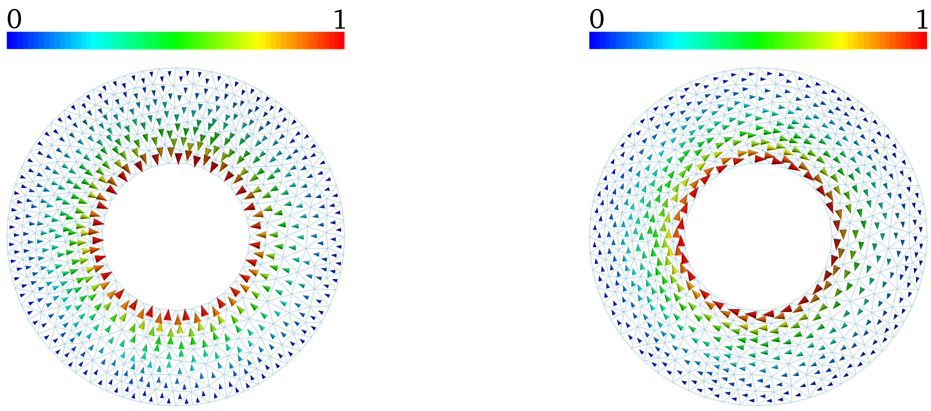

(a) Normalized electric field pattern

(b) Normalized magnetic field pattern

Figure 4.15: The fundamental mode (TEM) at port 1 when the computational domain is discretized with tetrahedral mesh at a spatial resolution of 10 CPW at 8 GHz.

Figure 4.16 depicts the signal used to excite both the electric and magnetic field components in time and frequency domains. The dominant frequency spectrum of the excitation covers 2–8 GHz.

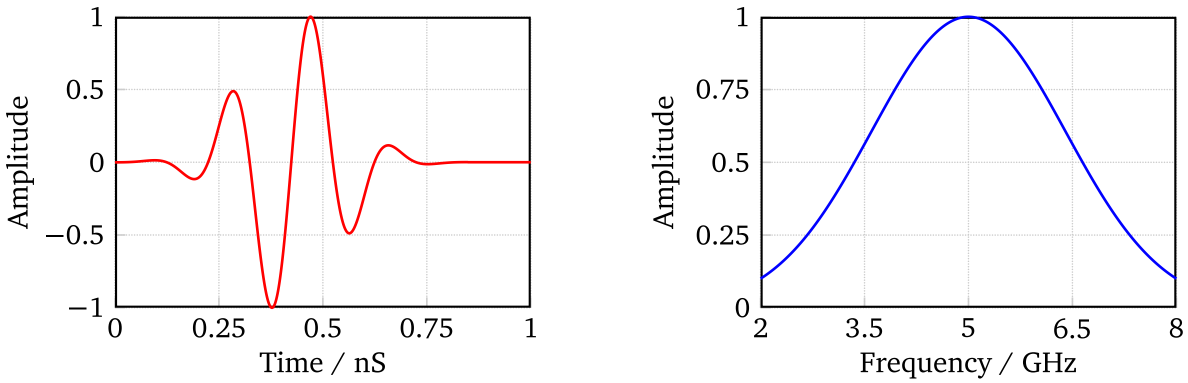

Figure 4.16: Time and frequency domain representations of coaxial cable excitation.

The S–parameters are obtained using second order FVTD method with gradient calculated from cell center values when the domain is discretized with tetrahedral mesh for various resolutions, 10 CPW till 60 CPW in steps of 10 CPW, and are depicted in Figure 4.17. The magnitude and phase of the S–parameters are also presented along with the complex plane representation in the above mentioned figure. One can observe the strong artificial dissipation present in second order FVTD method in which gradient is calculated from face center values in Figure 4.17(d).

Second order FVTD method with gradient calculated from cell center values is also employed at these resolutions to extract the S–parameters, in addition to FEM FD. The domain is also discretized with hexahedral mesh and S–parameters are also obtained with FIT TD and FIT FD, both employing PBA, for various spatial resolutions ranging from 10 CPW to 60 CPW, in steps of 10 CPW. The set of S–parameters obtained using FIT FD at a spatial resolution of 100 CPW is considered as the reference solution. All the S–parameters are extracted at the maximum possible time step for all the methods.

Figure 4.18 and Figure 4.19 depict the convergence of the minimum absolute error in the complex plane between the obtained solutions using various methods and reference solution for each of the S–parameters. FIT TD and FIT FD have less error than FVTD methods in the mentioned spatial resolution range. Note that the convergence order of second order FVTD method (gradient calculated from face center values) is very high. This means as the spatial resolution increases the error decreases, eventually to a value lower than all the methods. One can conclude that second order FVTD method with gradient calculated from face center values is able to resolve the high contrast of materials efficiently than the rest of the methods.

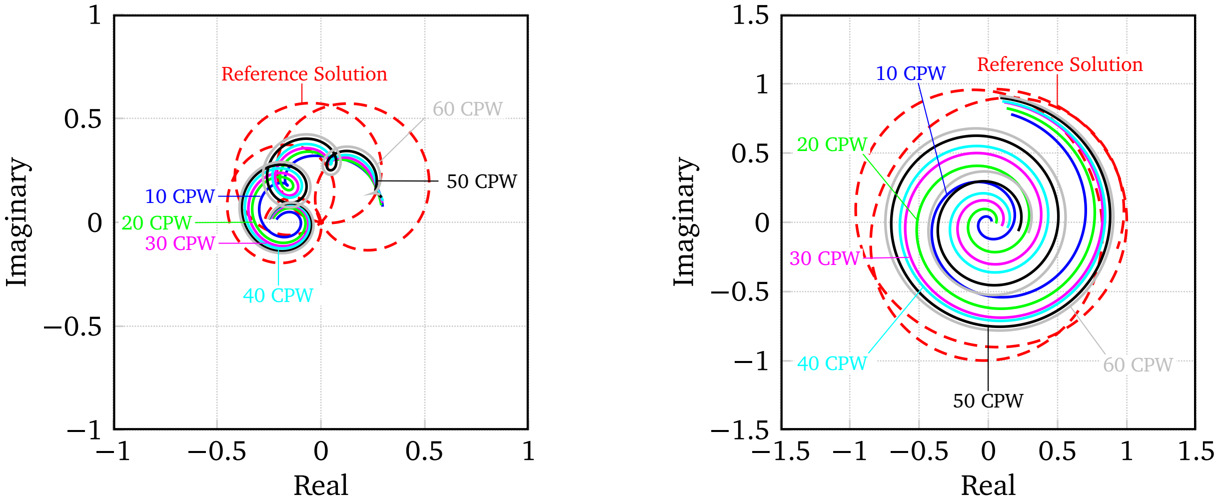

(a) S_{11} in complex plane.
(b) S_{21} in complex plane.

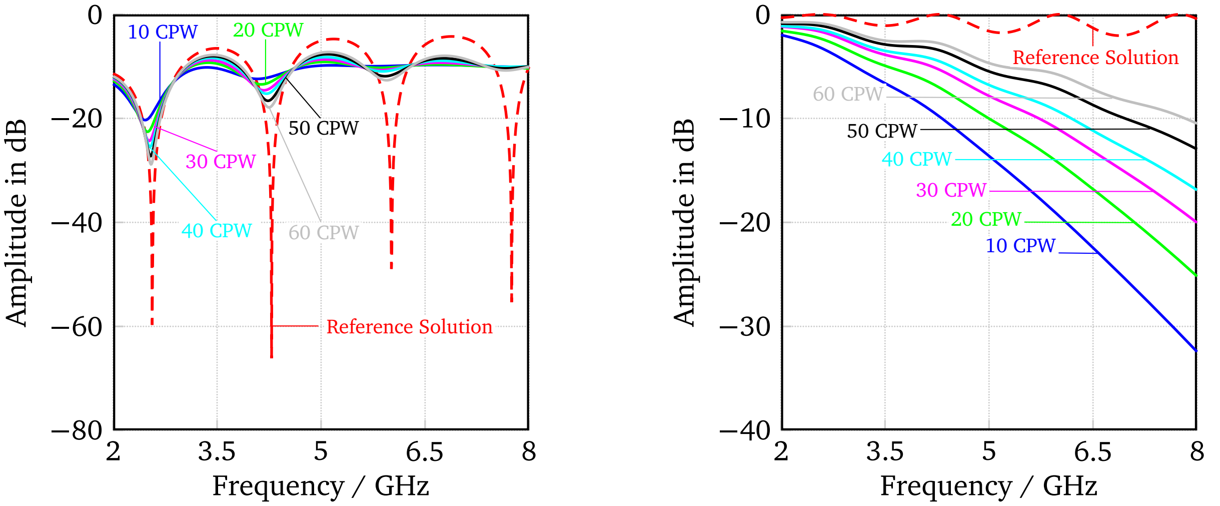

(c) S_{11} Magnitude.
(d) S_{21} Magnitude.

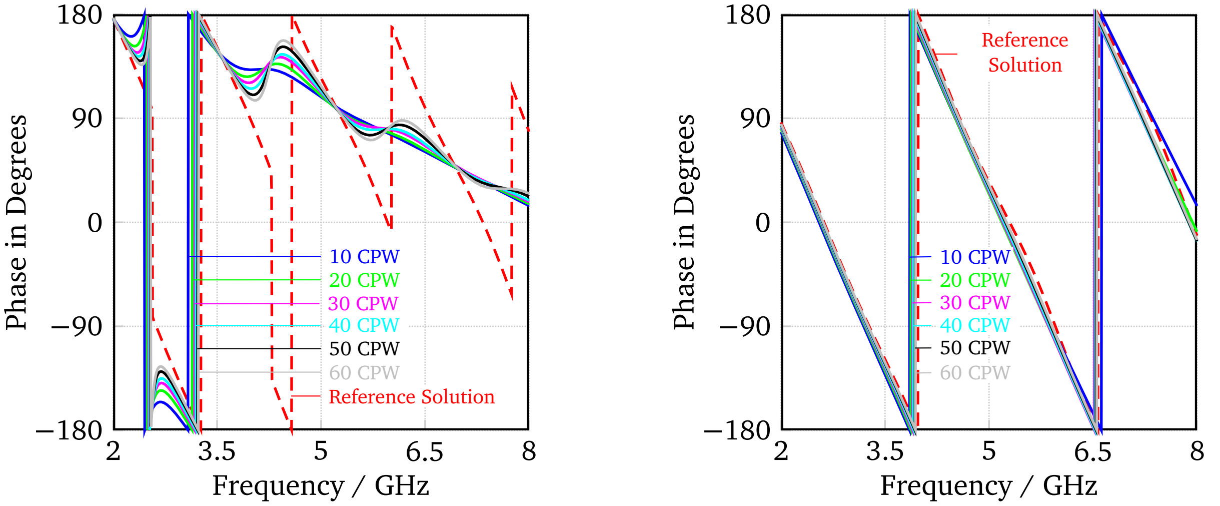

(e) S_{11} Phase.
(f) S_{21} Phase.

Figure 4.17: The S-parameters of the coaxial cable obtained using second order FVTD method (Gradient calculated from Cell Center values) for various spatial resolutions on tetrahedral mesh. The set of S-parameters obtained from FIT FD on hexahedral mesh at a resolution of 100 CPW is considered as the reference solution.

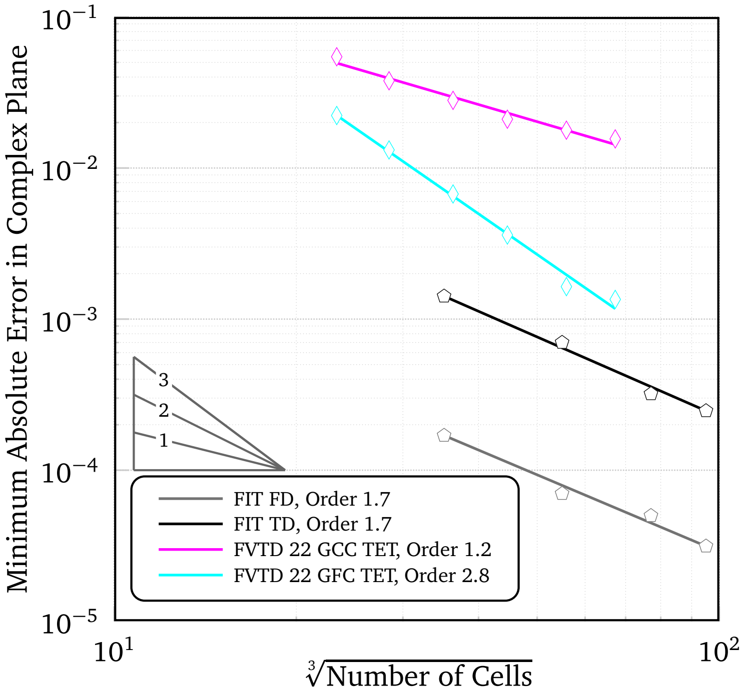

Figure 4.18: Convergence of error in S_{11} of coaxial cable. As the spatial resolution increases second order FVTD method with Gradient calculated from Face Center values outperforms the rest of the methods in terms of minimum error. Convergence orders are furnished in the legend. The diagonals of the right angle triangle indicate the reference orders.

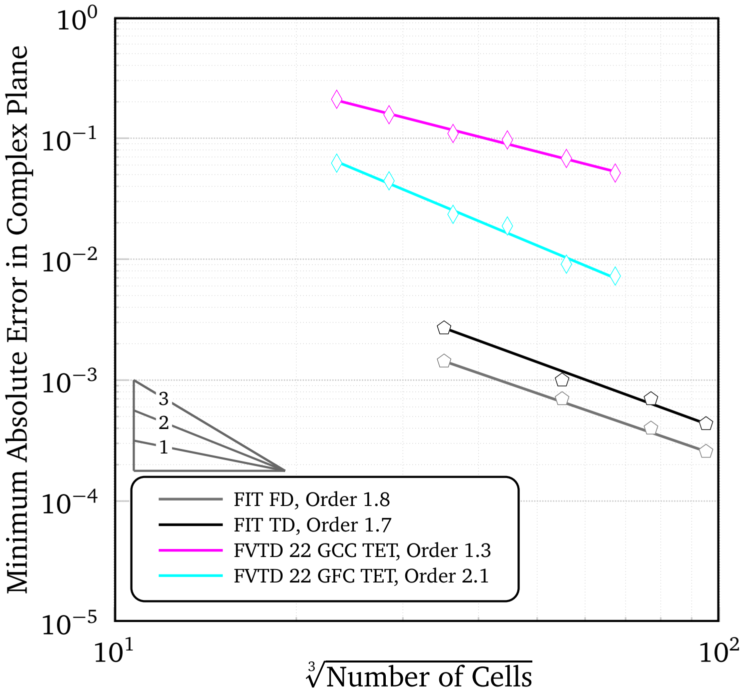

Figure 4.19: Convergence of error in S_{21} of coaxial cable. One can conclude that FIT FD and FIT TD have the same convergence order and FIT FD has minimum error within the observed spatial resolution range. Convergence orders are furnished in the legend. The diagonals of the right angle triangle indicate the reference orders.

4.4 Coaxial Connector

The coaxial connector depicted in Figure 4.20(a) is a complex structure with various materials (Vacuum, Teflon and Rubber) and components. The relative permittivity and permeability of Teflon are 2.04 and 1, respectively, where as Rubber has relative permittivity of 2.75 and relative permeability of 1. Figure 4.20(b) and Figure 4.20(c) present the same in different views. Full parametric description is furnished in Appendix 2.

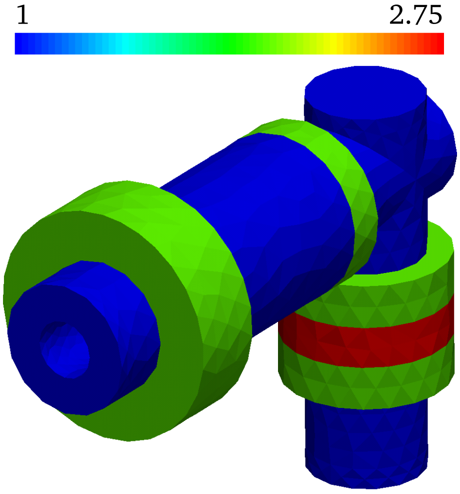

(a) 3D view along with relative permittivity profile

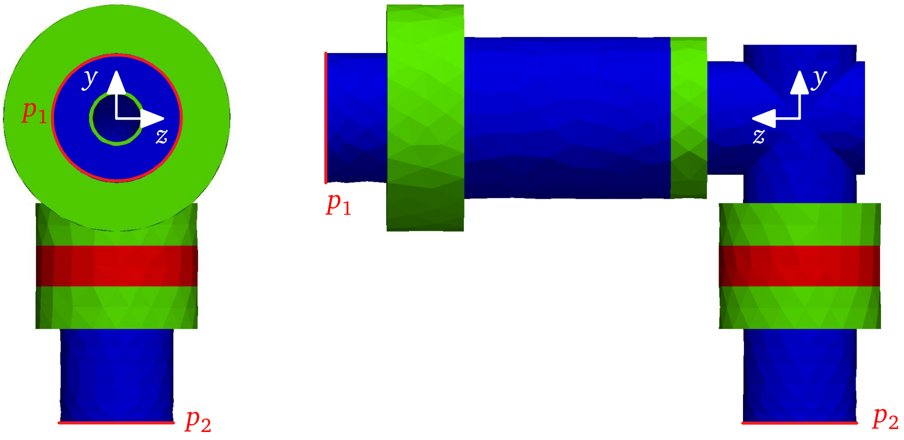

(b) Front view.

(c) Side view.

Figure 4.20: A coaxial connector with material description. The model is immersed in PEC medium. The ports are outlined in red color and are located in $+z$ and $-y$ directions. The two materials present other than Vacuum are Teflon (depicted in green color) and Rubber (represented red color).

The space surrounding the connector is PEC medium. Port 1 is located at the extreme end along the $+z$ axis and port 2 is at the extreme end in $-y$ direction. The fundamental mode is a TEM mode. Unlike in the previous applications, the wave has to propagate in the $-z$ direction after stimulation.

The field expressions for the fundamental mode are as follows [95]:

$$E_\rho = \frac{1}{\rho} \tag{4.13}$$

$$E_\varphi = 0 \tag{4.14}$$

$$E_z = 0 \tag{4.15}$$

$$H_\rho = 0 \tag{4.16}$$

$$H_\varphi = \frac{1}{\rho} \tag{4.17}$$

$$H_z = 0 \tag{4.18}$$

The domain is discretized with tetrahedral mesh with 10 CPW at 8 GHz. The TEM field pattern is imposed on the mesh at port 1. The field pattern is depicted in Figure 4.21. The excitation is depicted in Figure 4.22. The dominant frequency spectrum of the excitation signal lies between 1 GHz and 8 GHz.

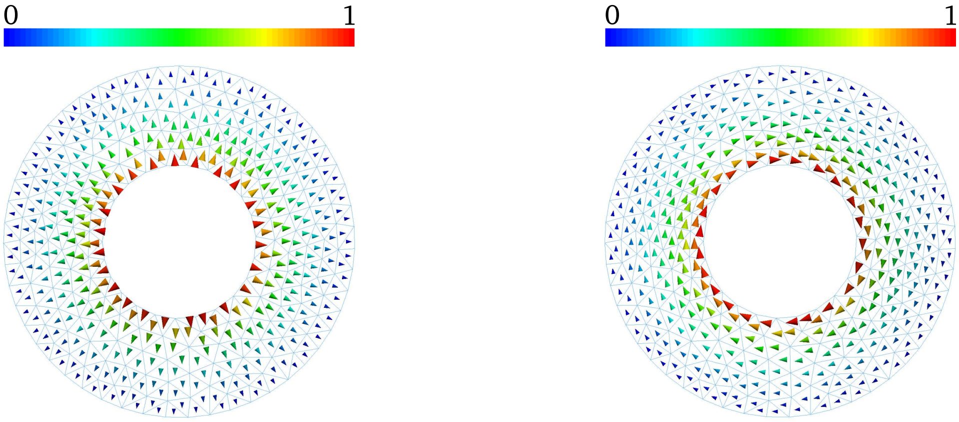

(a) Normalized electric field pattern (b) Normalized magnetic field pattern

Figure 4.21: Mode pattern used to stimulate coaxial connector at port 1, when the domain is discretized with tetrahedral mesh, at a spatial resolution of 10 CPW at 8 GHz.

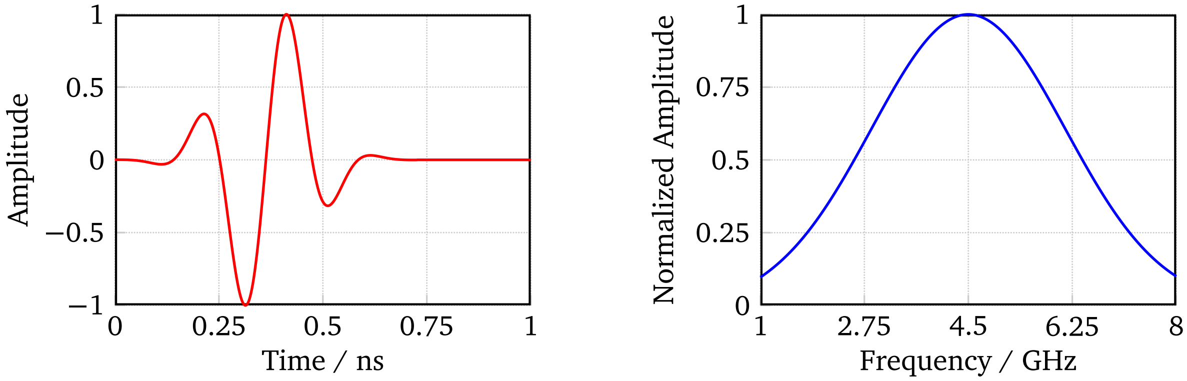

Figure 4.22: Time and frequency domain representations of coaxial connector excitation.

The S–parameters are extracted using second methods at various resolutions from 10 CPW till 50 CPW (in steps of 5 CPW till 30 CPW and later in steps of 10 CPW). FIT TD with PBA is also employed to extract the S–parameters at the same resolutions as FVTD methods but on hexahedral mesh.

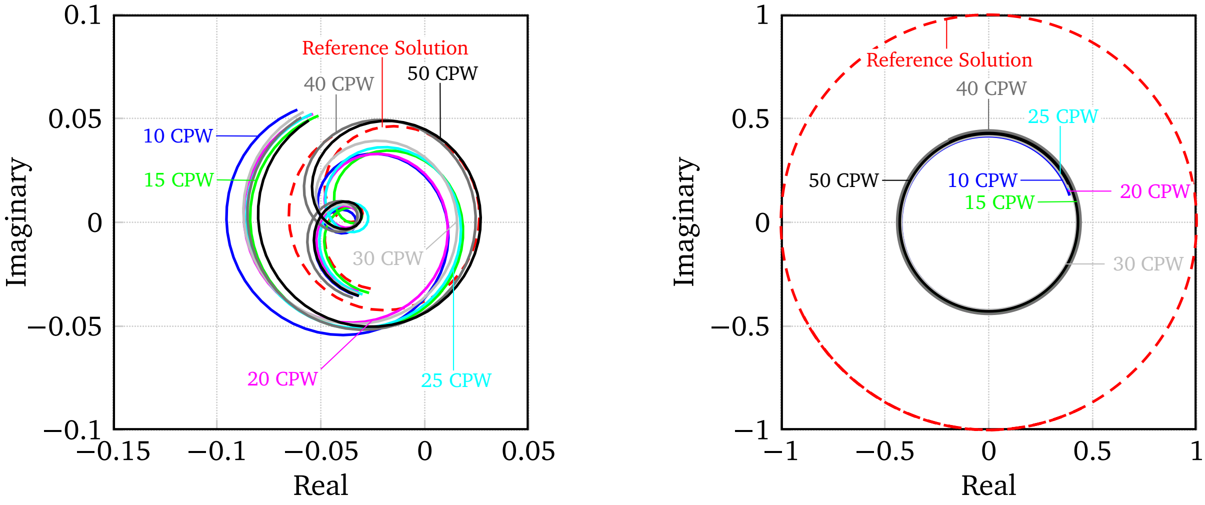

(a) S_{11} in complex plane.

(b) S_{21} in complex plane.

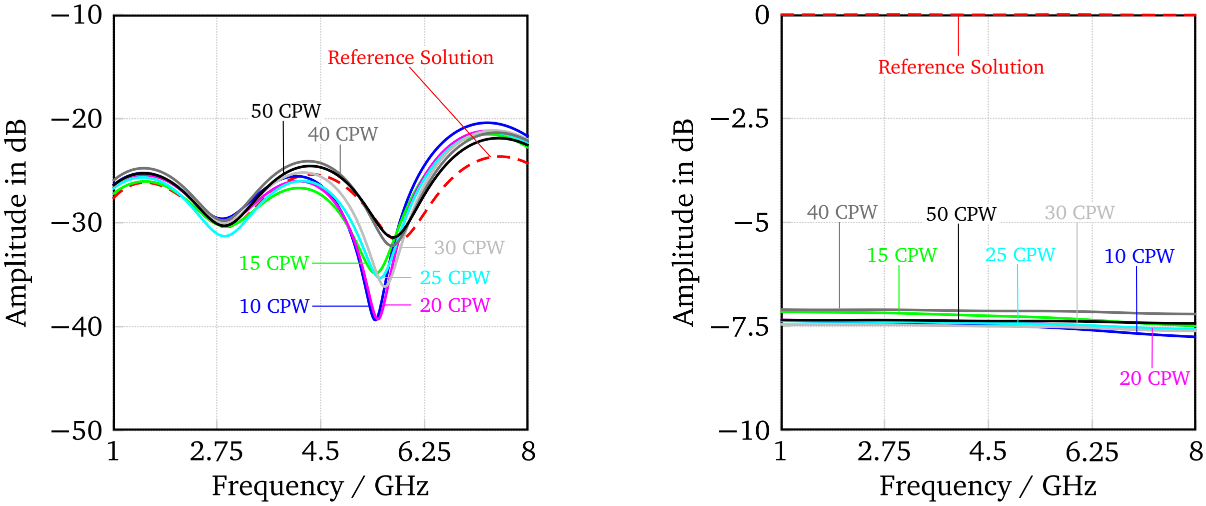

(c) S_{11} Magnitude.

(d) S_{21} Magnitude.

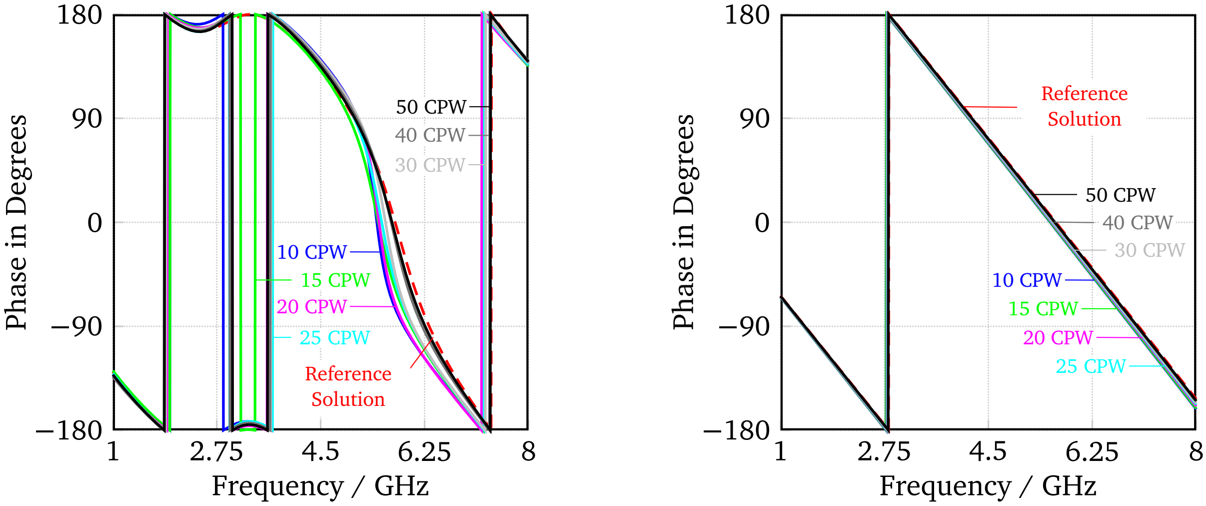

(e) S_{11} Phase.

(f) S_{21} Phase.

Figure 4.23: The S-parameters of the coaxial connector obtained using second order FVTD method (Gradient calculated from Face Center values) for various spatial resolutions on tetrahedral mesh. The S-parameters obtained from FIT TD on hexahedral mesh at a resolution of 175 CPW is considered as the reference solution.

The reference solution (FIT TD with PBA at a spatial resolution of 175 CPW) is obtained as mentioned in Page 59. Figure 4.23 depicts the S–parameters obtained using second order FVTD method with gradient calculated from face center values. One can observe in Figure 4.23(b) that the radius of the S–parameters obtained using FVTD methods is half of the reference value. This effect of artificial dissipation can also be noticed in Figure 4.23(d).

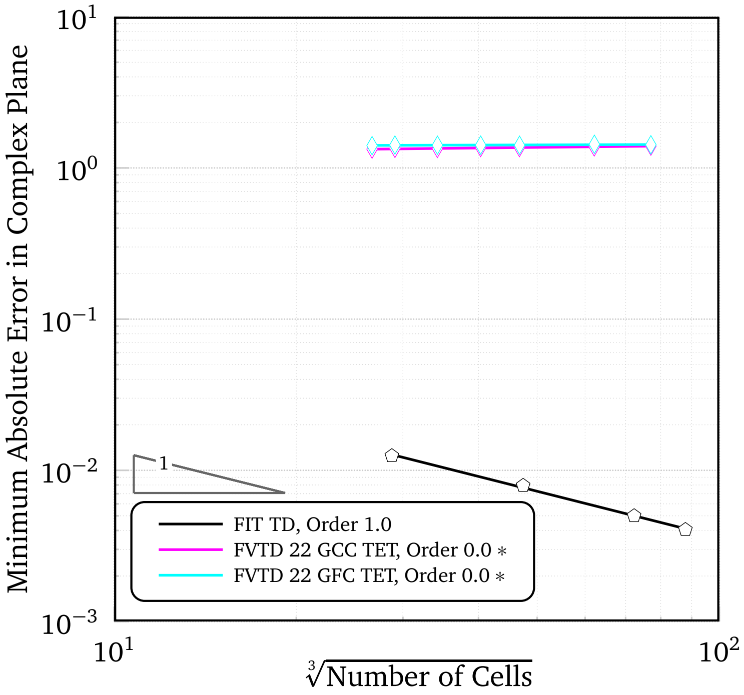

Figure 4.24: Convergence of error in S_{21} of coaxial connector. Convergence orders are furnished in the legend. The diagonal of the right angle triangle indicates the reference order. "∗" in the legend indicates the "non–convergent" behavior in the mentioned spatial resolution range.

The S–parameter, S_{11}, is very small in the complex plane and left out for the convergence study. The convergence of error in S_{21} is plotted in Figure 4.24 for various methods. One can observe the non–convergent behavior of the error in S_{21} due to strong artificial dissipation present, within the mentioned spatial resolution range.

5 Implementation

Abstract *– This chapter deals with the development of the finite volume time domain solver. Different modules of solver are furnished along with program flow at the concurrent stage. Various libraries used in the development are mentioned. The chapter notes the required floating point operations for several finite volume time domain methods.*

5.1 Code Development

The initial phase of this work is mainly carried out on 2D meshes, both hexahedral and triangular, obtained from MATLAB [96]. The 2D code written in MATLAB is standalone, meaning there is no need to leave the MATLAB environment from meshing till visualizing the results.

As the focus switched to the 3D problems NETGEN is used as tetrahedral mesher. At this stage, the preprocessing is done in MATLAB, whereas the solver is written in C [97]. MATLAB is used to visualize 1D results where as ParaView [98] is used to visualize the 2D and 3D results.

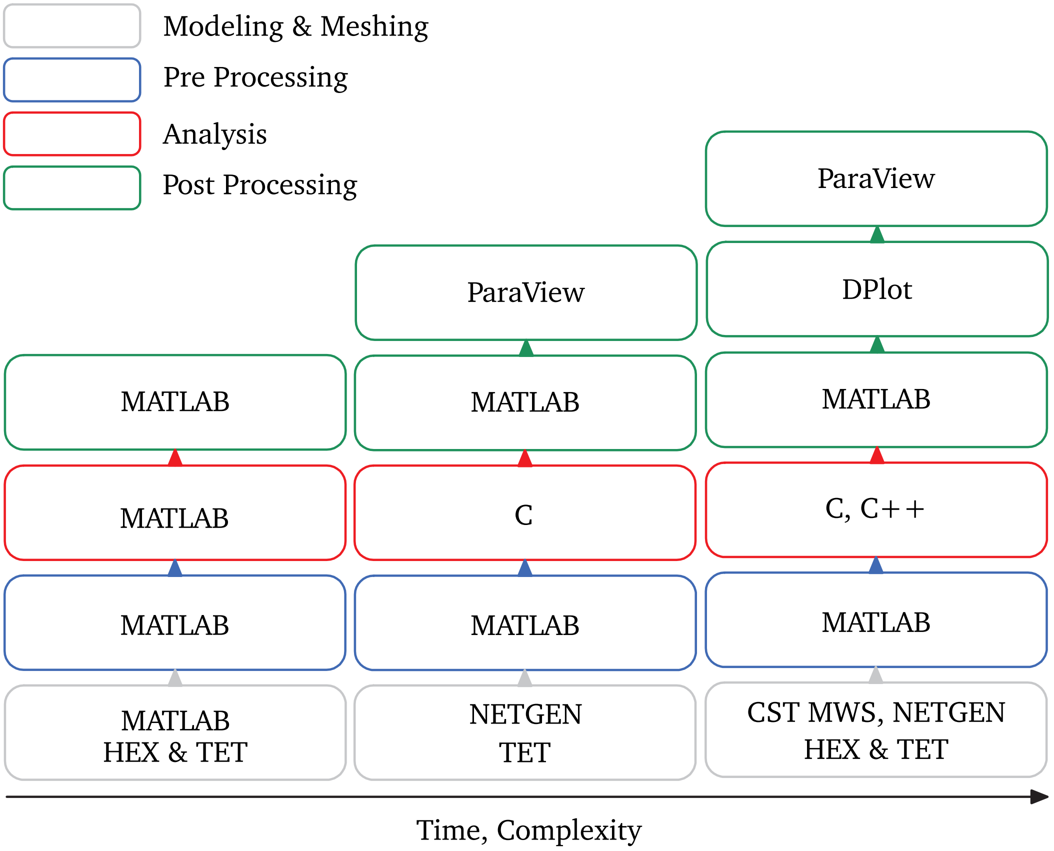

Figure 5.1: Various softwares used in the development of the FVTD 3D solver. Different modules in the code are also depicted.

Later, the hexahedral and tetrahedral meshes from CST MWS [99] are also incorporated into the solver in addition to tetrahedral mesh from NETGEN. The migration of solver from MATLAB to C, C++ [97] is achieved. In addition to MATLAB, DPlot [100] is also used to visualize 1D results.

Figure 5.1 explains the development of the solver. FVTD 3D program flow is depicted in Figure 5.2, with CST MWS as the modeler and mesher.

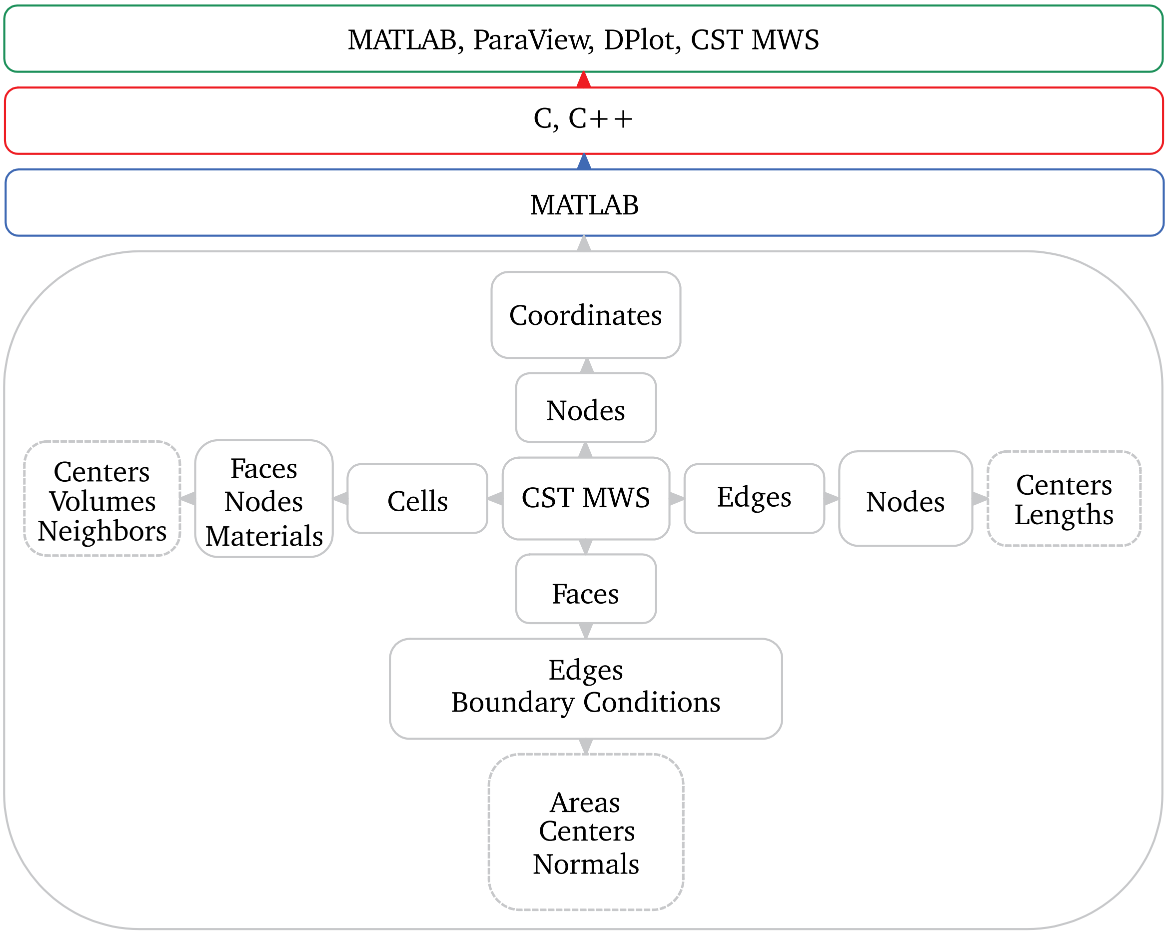

Figure 5.2: Program flow of FVTD 3D code, CST MWS being the modeler and mesher.

5.2 Code Modules

The basic modules in the solver can be categorized as meshing, preprocessing, analysis and postprocessing.

5.2.1 Meshing

Meshing is done using either NETGEN or CST MWS. NETGEN is an open source automatic tetrahedral mesher which employs Delaunay technique. It accepts input in STL, IGES and STEP formats. NETGEN contains modules for mesh optimization and hierarchical mesh refinement [101]. Figure 5.3 presents the mesh refinement feature of the NETGEN. CST MWS mesher can be interpreted as a wrapper for a wide variety of commercial meshers e.g., Ghs3d. “Ghs3d is a fully automatic tetrahedral mesh generator suitable to create volume meshes for complex domains defined by a conforming mesh of the boundary i.e., a surface triangulation. The volume mesh is governed by the properties of the surface mesh given as input. The latter governs the element density as well as the element shape quality. One of the main features of Ghs3d is that it preserves the boundary integrity of the initial surface mesh [102]”. Both NETGEN and Ghs3d provide the elements formed from nodes and coordinates of each node in ascii file format, from which all the mesh related information can be obtained. In addition, CST MWS provides information about cell to face indices, face to edge indices, etc.

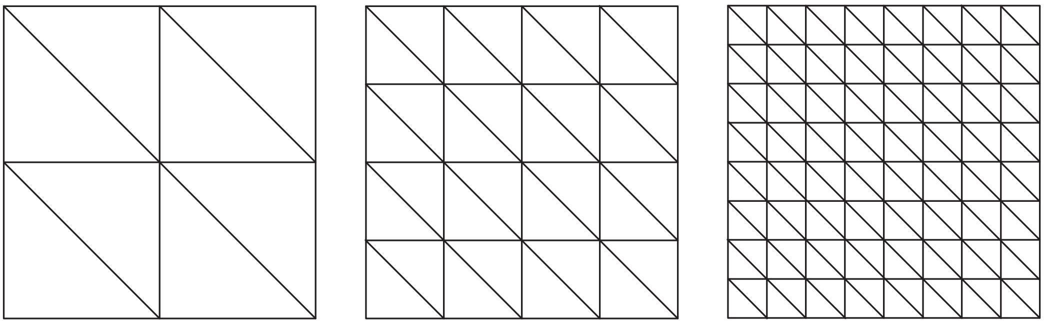
(a) Pass 1 (b) Pass 2 (c) Pass 3

Figure 5.3: Uniformly refined mesh from NETGEN. Refinement is one of the key features of the NETGEN mesher.

5.2.2 Preprocessing

MATLAB is used as a pre processor, mainly to verify various aspects of mesh and model such as the maximum possible time step, cell quality, boundary conditions, etc. All the routines are completely vectorized in MATLAB. This is a very essential step when dealing with complex geometries.

5.2.3 Analysis

The analysis part of the FVTD code is mainly written in C and C++. Different implementation strategies were tested, such as local formulation and global formulation. In the local formulation only the essential mesh information is stored, which eventually makes this scheme "low on memory". The global formulation, on the other hand, stores all the mesh related information in a matrix and is very intensive on memory. In terms of execution speed, global formulation is extremely fast when compared to the local formulation.

The GNU Scientific Library (GSL) is extensively used in order to reduce development time of the code. In addition, GSL offers brevity of syntax and numerical performance [103]. Intel Math Kernel Library (MKL) is used to implement the global formulation. It is a library of highly optimized math routines such as BLAS, LAPACK, ScaLAPACK, and Sparse Solvers [104].

One can observe from Figure 2.11(c) the presence of off diagonal entries in the system matrix. This makes parallelization difficult. Nevertheless, FVTD 22 GCC, FVTD 22 GFC on hexahedral mesh is easy to parallelize as the gradient is localized. On the other hand, FVTD 22 GCC on tetrahedral mesh is much more complicated to parallelize due to the fact that the gradient information is not localized. One can use METIS and ParMETIS [105] to gain efficiency and scalability. "METIS is a family of programs for partitioning unstructured graphs and hyper graphs and computing fill reducing orderings of sparse matrices. The underlying algorithms used by METIS are based on multilevel paradigm that has been shown to produce high quality results and scale up to very large problems. ParMETIS extends the functionality provided by METIS and includes routines that are especially suited for parallel computations and large scale numerical simulations. The algorithms implemented in ParMETIS are based on the parallel multilevel k–way graph–partitioning, adaptive repartitioning, and parallel multi–constrained partitioning schemes".

5.2.4 Postprocessing

MATLAB, DPlot and ParaView are used to analyze the results. More specifically, 1D results are visualized with MATLAB and DPlot, whereas 2D and 3D results are visualized with ParaView. DPlot provides the "drag and drop" facility of the data.

5.3 Computing Environment

All simulations in this work are performed on Intel Xeon CPU (X5472) 3.00 GHz with 64 GB RAM with Microsoft Windows Server 2003 Enterprise Edition.

5.4 Floating Point Operations

This section investigates the required FLoating point OPerationS (FLOPS) for various FVTD methods in semidiscrete form on both hexahedral and tetrahedral meshes. If a computational domain is discretized with volume mesh, the number of non–boundary cells far exceeds the number of boundary cells. Keeping this in view, the FLOPS are presented only for a single non–boundary cell.

As the focus is more on the number of entries and FLOPS than the actual values, the matrices and vectors have only two possible values, namely, "·" which indicates a zero entry and "1" which indicates the presence of a non–zero entry.

5.4.1 First Order Upwind Flux FVTD on Hexahedral Mesh

To start with consider the non–boundary cell i, depicted in Section 2.6, Page 26. For such a cell the first order upwind flux system mentioned in Equation 2.73 can be written as:

$$\frac{\partial u_i}{\partial t} = \sum_{k=1}^{6} \varphi^{+}_{ki} u_i + \varphi^{-}_{1i} u_{j1} + \varphi^{-}_{2i} u_{j2} + \varphi^{-}_{3i} u_{j3} + \varphi^{-}_{4i} u_{j4} + \varphi^{-}_{5i} u_{j5} + \varphi^{-}_{6i} u_{j6} \tag{5.1}$$

The coefficient matrices can be represented as:

$$\varphi^{\pm}_{ki}\Big|_{k=1}^{2} = \begin{pmatrix} \cdot & \cdot & \cdot & \cdot & \cdot & \cdot \\ \cdot & 1 & \cdot & \cdot & \cdot & 1 \\ \cdot & \cdot & 1 & \cdot & 1 & \cdot \\ \cdot & \cdot & \cdot & \cdot & \cdot & \cdot \\ \cdot & \cdot & 1 & \cdot & 1 & \cdot \\ \cdot & 1 & \cdot & \cdot & \cdot & 1 \end{pmatrix} \tag{5.2}$$

$$\varphi^{\pm}_{ki}\Big|_{k=3}^{4} = \begin{pmatrix} 1 & \cdot & \cdot & \cdot & \cdot & 1 \\ \cdot & \cdot & \cdot & \cdot & \cdot & \cdot \\ \cdot & \cdot & 1 & 1 & \cdot & \cdot \\ \cdot & \cdot & 1 & 1 & \cdot & \cdot \\ \cdot & \cdot & \cdot & \cdot & \cdot & \cdot \\ 1 & \cdot & \cdot & \cdot & \cdot & 1 \end{pmatrix} \tag{5.3}$$

$$\varphi^{\pm}_{ki}\Big|_{k=5}^{6} = \begin{pmatrix} 1 & \cdot & \cdot & \cdot & 1 & \cdot \\ \cdot & 1 & \cdot & 1 & \cdot & \cdot \\ \cdot & \cdot & \cdot & \cdot & \cdot & \cdot \\ \cdot & 1 & \cdot & 1 & \cdot & \cdot \\ 1 & \cdot & \cdot & \cdot & 1 & \cdot \\ \cdot & \cdot & \cdot & \cdot & \cdot & \cdot \end{pmatrix} \tag{5.4}$$

One can write net outgoing flux from the cell i, ϕ^{+}_{i}, as:

$$\phi^{+}_{i} = \sum_{k=1}^{6} \varphi^{+}_{ki} u_i \tag{5.5}$$

The number of FLOPS required for net outgoing flux is presented below. Note that "A" represents an "Addition" and "M" represents a "Multiplication".

$$\phi_i^+ \quad = \quad \begin{pmatrix} 1 & \cdot & \cdot & \cdot & 1 & 1 \\ \cdot & 1 & \cdot & 1 & \cdot & 1 \\ \cdot & \cdot & 1 & 1 & 1 & \cdot \\ \cdot & 1 & 1 & 1 & \cdot & \cdot \\ 1 & \cdot & 1 & \cdot & 1 & \cdot \\ 1 & 1 & \cdot & \cdot & \cdot & 1 \end{pmatrix} \cdot \begin{pmatrix} e_{xi} \\ e_{yi} \\ e_{zi} \\ h_{xi} \\ h_{yi} \\ h_{zi} \end{pmatrix} \mapsto 18\text{M} + 12\text{A} \tag{5.6}$$

The incoming flux through face f_{1i} is

$$\varphi_{1i}^- u_{j1} = \begin{pmatrix} \cdot & \cdot & \cdot & \cdot & \cdot & \cdot \\ \cdot & 1 & \cdot & \cdot & \cdot & 1 \\ \cdot & \cdot & 1 & \cdot & 1 & \cdot \\ \cdot & \cdot & \cdot & \cdot & \cdot & \cdot \\ \cdot & \cdot & 1 & \cdot & 1 & \cdot \\ \cdot & 1 & \cdot & \cdot & \cdot & 1 \end{pmatrix} \cdot \begin{pmatrix} e_{xj1} \\ e_{yj1} \\ e_{zj1} \\ h_{xj1} \\ h_{yj1} \\ h_{zj1} \end{pmatrix} \mapsto 8\text{M} + 4\text{A} \tag{5.7}$$

Similar expressions for the incoming fluxes through the rest of the faces can also be written. The semidiscrete formulation mentioned in Equation 5.1 is altered as below:

$$\frac{\partial u_i}{\partial t} \quad = \quad \underbrace{\phi_i^+}_{\text{18M+12A}} + \underbrace{\varphi_{1i}^- u_{j1}}_{\text{8M+4A}} + \underbrace{\varphi_{2i}^- u_{j2}}_{\text{8M+4A}} + \underbrace{\varphi_{3i}^- u_{j3}}_{\text{8M+4A}} + \underbrace{\varphi_{4i}^- u_{j4}}_{\text{8M+4A}} + \underbrace{\varphi_{5i}^- u_{j5}}_{\text{8M+4A}} + \underbrace{\varphi_{6i}^- u_{j6}}_{\text{8M+4A}} \tag{5.8}$$

$$\mapsto \quad \begin{pmatrix} 1 \\ 1 \\ 1 \\ 1 \\ 1 \\ 1 \end{pmatrix} \underbrace{+}_{\text{4A}} \begin{pmatrix} \cdot \\ 1 \\ 1 \\ \cdot \\ 1 \\ 1 \end{pmatrix} \underbrace{+}_{\text{4A}} \begin{pmatrix} \cdot \\ 1 \\ 1 \\ \cdot \\ 1 \\ 1 \end{pmatrix} \underbrace{+}_{\text{4A}} \begin{pmatrix} 1 \\ \cdot \\ 1 \\ 1 \\ \cdot \\ 1 \end{pmatrix} \underbrace{+}_{\text{4A}} \begin{pmatrix} 1 \\ \cdot \\ 1 \\ 1 \\ \cdot \\ 1 \end{pmatrix} \underbrace{+}_{\text{4A}} \begin{pmatrix} 1 \\ 1 \\ \cdot \\ 1 \\ 1 \\ \cdot \end{pmatrix} \underbrace{+}_{\text{4A}} \begin{pmatrix} 1 \\ 1 \\ \cdot \\ 1 \\ 1 \\ \cdot \end{pmatrix} \tag{5.9}$$

$$\mapsto \quad 18\text{M} + 12\text{A} + 6\,(8\text{M} + 4\text{A}) + 6\,(4\text{A}) \tag{5.10}$$

$$\frac{\partial u_i}{\partial t} \quad \mapsto \quad 66\text{M} + 60\text{A} \tag{5.11}$$

Thus, the FLOPS required for first order upwind flux finite volume system on hexahedral mesh is 66 multiplications along with 60 additions.

5.4.2 First Order Upwind Flux FVTD on Tetrahedral Mesh

Consider a non–boundary cell i in a computational domain discretized with tetrahedral mesh. Assume that none of the faces of this cell are parallel to the cartesian planes i.e., the normal to any face of this cell is not oriented along coordinate axis. This ensures that the number and position of entries in each coefficient matrix remain the same.

Let $j1$, $j2$, $j3$, and $j4$ be the neighbors of this cell. The semidiscrete form of upwind flux first order finite volume system can be expressed as:

$$\frac{\partial u_i}{\partial t} \quad = \quad \sum_{k=1}^{4} \varphi_{ki}^+ u_i + \varphi_{1i}^- u_{j1} + \varphi_{2i}^- u_{j2} + \varphi_{3i}^- u_{j3} + \varphi_{4i}^- u_{j4} \tag{5.12}$$

The flux matrices are more populated compared to the flux matrices on hexahedral mesh. The position of entries in all the flux matrices is identical. One can express the net outgoing flux as:

$$\phi_i^+ = \sum_{k=1}^{4} \varphi_{ki}^+ u_i = \begin{pmatrix} 1 & 1 & 1 & \cdot & 1 & 1 \\ 1 & 1 & 1 & 1 & \cdot & 1 \\ 1 & 1 & 1 & 1 & 1 & \cdot \\ \cdot & 1 & 1 & 1 & 1 & 1 \\ 1 & \cdot & 1 & 1 & 1 & 1 \\ 1 & 1 & \cdot & 1 & 1 & 1 \end{pmatrix} \cdot \begin{pmatrix} e_{xi} \\ e_{yi} \\ e_{zi} \\ h_{xi} \\ h_{yi} \\ h_{zi} \end{pmatrix} \mapsto 30\text{M} + 24\text{A} \tag{5.13}$$

The position of entries in the coefficient matrices of the incoming fluxes through each face is the same as above. The incoming flux through face f_{1i} can be written as:

$$\varphi_{1i}^- u_{j1} = \begin{pmatrix} 1 & 1 & 1 & \cdot & 1 & 1 \\ 1 & 1 & 1 & 1 & \cdot & 1 \\ 1 & 1 & 1 & 1 & 1 & \cdot \\ \cdot & 1 & 1 & 1 & 1 & 1 \\ 1 & \cdot & 1 & 1 & 1 & 1 \\ 1 & 1 & \cdot & 1 & 1 & 1 \end{pmatrix} \cdot \begin{pmatrix} e_{xj1} \\ e_{yj1} \\ e_{zj1} \\ h_{xj1} \\ h_{yj1} \\ h_{zj1} \end{pmatrix} \mapsto 30\text{M} + 24\text{A} \tag{5.14}$$

The semidiscrete formulation mentioned in Equation 5.12 can be represented as below:

$$\frac{\partial u_i}{\partial t} = \underbrace{\phi_i^+}_{\text{30M+24A}} + \underbrace{\varphi_{1i}^- u_{j1}}_{\text{30M+24A}} + \underbrace{\varphi_{2i}^- u_{j2}}_{\text{30M+24A}} + \underbrace{\varphi_{3i}^- u_{j3}}_{\text{30M+24A}} + \underbrace{\varphi_{4i}^- u_{j4}}_{\text{30M+24A}} \tag{5.15}$$

$$\mapsto \begin{pmatrix} 1 \\ 1 \\ 1 \\ 1 \\ 1 \\ 1 \end{pmatrix} \underbrace{+}_{\text{6A}} \begin{pmatrix} 1 \\ 1 \\ 1 \\ 1 \\ 1 \\ 1 \end{pmatrix} \underbrace{+}_{\text{6A}} \begin{pmatrix} 1 \\ 1 \\ 1 \\ 1 \\ 1 \\ 1 \end{pmatrix} \underbrace{+}_{\text{6A}} \begin{pmatrix} 1 \\ 1 \\ 1 \\ 1 \\ 1 \\ 1 \end{pmatrix} \underbrace{+}_{\text{6A}} \begin{pmatrix} 1 \\ 1 \\ 1 \\ 1 \\ 1 \\ 1 \end{pmatrix} \tag{5.16}$$

$$\mapsto 5(30\text{M} + 24\text{A}) + 4(6\text{A}) \tag{5.17}$$

$$\frac{\partial u_i}{\partial t} \mapsto 150\text{M} + 144\text{A} \tag{5.18}$$

The FLOPS required for first order upwind flux finite volume system on tetrahedral mesh is 150 multiplications along with 144 additions.

5.4.3 Second Order Upwind Flux FVTD on Hexahedral Mesh

In second order schemes, the field values on face centers are obtained using piecewise linear interpolation. This necessitates the calculation of gradient. On a hexahedral mesh gradient can be calculated using immediate neighbors. The semidiscrete formulation of second order upwind flux system mentioned in Equation 2.59 is reproduced here.

$$\frac{\partial u_i}{\partial t} = \phi_i^+ + \phi_i^- \tag{5.19}$$

The net outgoing flux from cell i, ϕ_i^+, employing second order upwind flux method can be expressed as, from Equation 2.89:

$$
\begin{aligned}
\phi_i^+ = \quad & \left[\varphi^+_{ki}\beta_{ki}\right]\Big|_{k=1}^{k=6} u_i + \\
& \left[\varphi^+_{ki}\beta_{j1}\right]\Big|_{k=1}^{k=2} u_{j1} + \left[\varphi^+_{ki}\beta_{j2}\right]\Big|_{k=1}^{k=2} u_{j2} + \left[\varphi^+_{ki}\beta_{j3}\right]\Big|_{k=3}^{k=4} u_{j3} + \\
& \left[\varphi^+_{ki}\beta_{j4}\right]\Big|_{k=3}^{k=4} u_{j4} + \left[\varphi^+_{ki}\beta_{j5}\right]\Big|_{k=5}^{k=6} u_{j5} + \left[\varphi^+_{ki}\beta_{j6}\right]\Big|_{k=5}^{k=6} u_{j6}
\end{aligned}
\tag{5.20}
$$

where

$$
\left[\varphi^+_{ki}\beta_{ki}\right]\Big|_{k=1}^{k=6} u_i = \begin{pmatrix} 1 & \cdot & \cdot & \cdot & 1 & 1 \\ \cdot & 1 & \cdot & 1 & \cdot & 1 \\ \cdot & \cdot & 1 & 1 & 1 & \cdot \\ \cdot & 1 & 1 & 1 & \cdot & \cdot \\ 1 & \cdot & 1 & \cdot & 1 & \cdot \\ 1 & 1 & \cdot & \cdot & \cdot & 1 \end{pmatrix} \cdot \begin{pmatrix} e_{xi} \\ e_{yi} \\ e_{zi} \\ h_{xi} \\ h_{yi} \\ h_{zi} \end{pmatrix} \mapsto 18\text{M} + 12\text{A} \tag{5.21}
$$

$$
\left[\varphi^+_{ki}\beta_{j1}\right]\Big|_{k=1}^{k=2} u_{j1} = \begin{pmatrix} \cdot & \cdot & \cdot & \cdot & \cdot & \cdot \\ \cdot & 1 & \cdot & \cdot & \cdot & 1 \\ \cdot & \cdot & 1 & \cdot & 1 & \cdot \\ \cdot & \cdot & \cdot & \cdot & \cdot & \cdot \\ \cdot & \cdot & 1 & \cdot & 1 & \cdot \\ \cdot & 1 & \cdot & \cdot & \cdot & 1 \end{pmatrix} \cdot \begin{pmatrix} e_{xj1} \\ e_{yj1} \\ e_{zj1} \\ h_{xj1} \\ h_{yj1} \\ h_{zj1} \end{pmatrix} \mapsto 8\text{M} + 4\text{A} \tag{5.22}
$$

Though not mentioned here similar expressions for the rest of the terms in the Equation 5.20 can be written. The net outgoing flux from cell i, ϕ_i^+ is furnished below:

$$
\begin{aligned}
\phi_i^+ \quad = \quad & \underbrace{\left[\varphi^+_{ki}\beta_{ki}\right]\Big|_{k=1}^{k=6} u_i +}_{\text{18M+12A}} \\
& \underbrace{\left[\varphi^+_{ki}\beta_{j1}\right]\Big|_{k=1}^{k=2} u_{j1} +}_{\text{8M+4A}} \underbrace{\left[\varphi^+_{ki}\beta_{j2}\right]\Big|_{k=1}^{k=2} u_{j2} +}_{\text{8M+4A}} \underbrace{\left[\varphi^+_{ki}\beta_{j1}\right]\Big|_{k=3}^{k=4} u_{j3} +}_{\text{8M+4A}} \\
& \underbrace{\left[\varphi^+_{ki}\beta_{j2}\right]\Big|_{k=3}^{k=4} u_{j4} +}_{\text{8M+4A}} \underbrace{\left[\varphi^+_{ki}\beta_{j1}\right]\Big|_{k=5}^{k=6} u_{j5} +}_{\text{8M+4A}} \underbrace{\left[\varphi^+_{ki}\beta_{j2}\right]\Big|_{k=5}^{k=6} u_{j6}}_{\text{8M+4A}}
\end{aligned}
\tag{5.23}
$$

$$
\mapsto \quad \begin{pmatrix} 1 \\ 1 \\ 1 \\ 1 \\ 1 \\ 1 \end{pmatrix} \underbrace{+}_{\text{4A}} \begin{pmatrix} \cdot \\ 1 \\ 1 \\ \cdot \\ 1 \\ 1 \end{pmatrix} \underbrace{+}_{\text{4A}} \begin{pmatrix} \cdot \\ 1 \\ 1 \\ \cdot \\ 1 \\ 1 \end{pmatrix} \underbrace{+}_{\text{4A}} \begin{pmatrix} 1 \\ \cdot \\ 1 \\ 1 \\ \cdot \\ 1 \end{pmatrix} \underbrace{+}_{\text{4A}} \begin{pmatrix} 1 \\ \cdot \\ 1 \\ 1 \\ \cdot \\ 1 \end{pmatrix} \underbrace{+}_{\text{4A}} \begin{pmatrix} 1 \\ 1 \\ \cdot \\ 1 \\ 1 \\ \cdot \end{pmatrix} \underbrace{+}_{\text{4A}} \begin{pmatrix} 1 \\ 1 \\ \cdot \\ 1 \\ 1 \\ \cdot \end{pmatrix} \tag{5.24}
$$

$$
\mapsto \quad 18\text{M} + 12\text{A} + 6\,(8\text{M} + 4\text{A}) + 6\,(4\text{A}) \tag{5.25}
$$

$$
\mapsto \quad 66\text{M} + 60\text{A} \tag{5.26}
$$

The net incoming flux into cell i, ϕ_i^- can be expressed as the sum of incoming fluxes through all the faces of cell i.

$$\begin{aligned} \phi_i^- &= \sum_{k=1}^{6} \varphi_{ki}^- u_{ki}^+ \qquad (5.27) \\ &= \chi_{1i}^- + \chi_{2i}^- + \chi_{3i}^- + \chi_{4i}^- + \chi_{5i}^- + \chi_{6i}^- \qquad (5.28) \end{aligned}$$

In order to calculate the incoming flux through a face, say f_{1i}, one has to calculate the field values on the outside of face, u_{1i}^+. These field values are nothing but weighted functions of gradient in the cell $j1$. On a hexahedral mesh, the field values on face f_{1i} can be obtained from the x directional gradient alone.

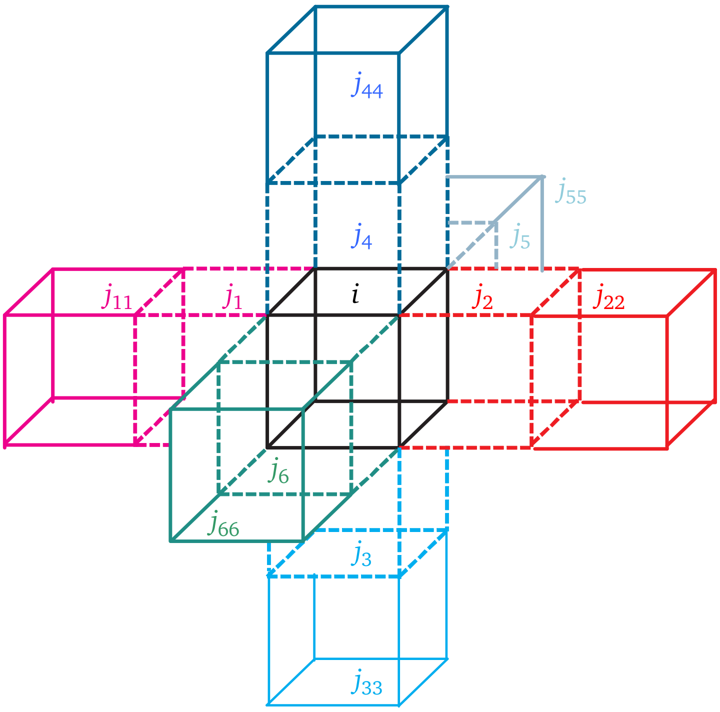

Figure 5.4: A unit cell in the hexahedral mesh, with neighbors of neighbors. The directional gradient of field values in each cell is dependent on immediate neighbors in that direction.

Figure 5.4 portrays the neighbors of neighbors of cell i. The gradient in x direction in cell j_1 can be calculated from barycenter field values of cells i, j_1 and j_{11}. In other words, the net incoming flux, χ_{1i}^-, through f_{1i} is dependent on the field values of cells i, j_1 and j_{11}. Mathematically this can be expressed as:

$$\chi_{1i}^- = \left[\varphi_{1i}^- \beta_{j1}\right] u_{j1} + \left[\varphi_{1i}^- \beta_{j11}\right] u_{j11} + \left[\varphi_{1i}^- \beta_{i}\right] u_{i} \qquad (5.29)$$

One can write

$$\left[\varphi_{1i}^- \beta_{j1}\right] u_{j1} = \begin{pmatrix} \cdot & \cdot & \cdot & \cdot & \cdot & \cdot \\ \cdot & 1 & \cdot & \cdot & \cdot & 1 \\ \cdot & \cdot & 1 & \cdot & 1 & \cdot \\ \cdot & \cdot & \cdot & \cdot & \cdot & \cdot \\ \cdot & \cdot & 1 & \cdot & 1 & \cdot \\ \cdot & 1 & \cdot & \cdot & \cdot & 1 \end{pmatrix} \cdot \begin{pmatrix} e_{xj1} \\ e_{yj1} \\ e_{zj1} \\ h_{xj1} \\ h_{yj1} \\ h_{zj1} \end{pmatrix} \mapsto 0\text{M} + 0\text{A} \qquad (5.30)$$

$$\left[\varphi_{1i}^{-}\beta_{j11}\right]u_{j11} = \begin{pmatrix} \cdot & \cdot & \cdot & \cdot & \cdot & \cdot \\ \cdot & 1 & \cdot & \cdot & \cdot & 1 \\ \cdot & \cdot & 1 & \cdot & 1 & \cdot \\ \cdot & \cdot & \cdot & \cdot & \cdot & \cdot \\ \cdot & \cdot & 1 & \cdot & 1 & \cdot \\ \cdot & 1 & \cdot & \cdot & \cdot & 1 \end{pmatrix} \cdot \begin{pmatrix} e_{xj11} \\ e_{yj11} \\ e_{zj11} \\ h_{xj11} \\ h_{yj11} \\ h_{zj11} \end{pmatrix} \mapsto 8\text{M} + 4\text{A} \tag{5.31}$$

$$\left[\varphi_{1i}^{-}\beta_{i}\right]u_{i} = \begin{pmatrix} \cdot & \cdot & \cdot & \cdot & \cdot & \cdot \\ \cdot & 1 & \cdot & \cdot & \cdot & 1 \\ \cdot & \cdot & 1 & \cdot & 1 & \cdot \\ \cdot & \cdot & \cdot & \cdot & \cdot & \cdot \\ \cdot & \cdot & 1 & \cdot & 1 & \cdot \\ \cdot & 1 & \cdot & \cdot & \cdot & 1 \end{pmatrix} \cdot \begin{pmatrix} e_{xi} \\ e_{yi} \\ e_{zi} \\ h_{xi} \\ h_{yi} \\ h_{zi} \end{pmatrix} \mapsto 0\text{M} + 0\text{A} \tag{5.32}$$

Observe in Equation 5.30 and Equation 5.32 the number of FLOPS are counted as 0 because the flux matrices in the above mentioned equations are acting on the same barycenter field values as in Equation 5.20. In such a case, the operands can be summed up when constructing the system matrix.

$$\chi_{1i}^{-} = \underbrace{\left[\varphi_{1i}^{-}\beta_{j1}\right]u_{j1}}_{\text{0M+0A}} + \underbrace{\left[\varphi_{1i}^{-}\beta_{j11}\right]u_{j11}}_{\text{8M+4A}} + \underbrace{\left[\varphi_{1i}^{-}\beta_{i}\right]u_{i}}_{\text{0M+0A}} \tag{5.33}$$

Similar expression for the rest of the incoming fluxes yields,

$$\phi_i^{-} = \underbrace{\chi_{1i}^{-}}_{\text{8M+4A}} + \underbrace{\chi_{2i}^{-}}_{\text{8M+4A}} + \underbrace{\chi_{3i}^{-}}_{\text{8M+4A}} + \underbrace{\chi_{4i}^{-}}_{\text{8M+4A}} + \underbrace{\chi_{5i}^{-}}_{\text{8M+4A}} + \underbrace{\chi_{6i}^{-}}_{\text{8M+4A}} \tag{5.34}$$

$$= \begin{pmatrix} \cdot \\ 1 \\ 1 \\ \cdot \\ 1 \\ 1 \end{pmatrix} \underbrace{+}_{\text{4A}} \begin{pmatrix} \cdot \\ 1 \\ 1 \\ \cdot \\ 1 \\ 1 \end{pmatrix} \underbrace{+}_{\text{4A}} \begin{pmatrix} 1 \\ \cdot \\ 1 \\ 1 \\ \cdot \\ 1 \end{pmatrix} \underbrace{+}_{\text{4A}} \begin{pmatrix} 1 \\ \cdot \\ 1 \\ 1 \\ \cdot \\ 1 \end{pmatrix} \underbrace{+}_{\text{4A}} \begin{pmatrix} 1 \\ 1 \\ \cdot \\ 1 \\ 1 \\ \cdot \end{pmatrix} \underbrace{+}_{\text{4A}} \begin{pmatrix} 1 \\ 1 \\ \cdot \\ 1 \\ 1 \\ \cdot \end{pmatrix} \tag{5.35}$$

$$\mapsto 6\,(8\text{M} + 4\text{A}) + 5\,(4\text{A}) \tag{5.36}$$

$$\mapsto 48\text{M} + 44\text{A} \tag{5.37}$$

The semidiscrete formulation of upwind flux second order finite volume system can be written as:

$$\frac{\partial u_i}{\partial t} = \underbrace{\phi_i^{+}}_{\text{66M+60A}} + \underbrace{\phi_i^{-}}_{\text{48M+44A}} \tag{5.38}$$

$$\mapsto \begin{pmatrix} 1 \\ 1 \\ 1 \\ 1 \\ 1 \\ 1 \end{pmatrix} \underbrace{+}_{\text{6A}} \begin{pmatrix} 1 \\ 1 \\ 1 \\ 1 \\ 1 \\ 1 \end{pmatrix} \tag{5.39}$$

$$\mapsto 66\text{M} + 60\text{A} + 48\text{M} + 44\text{A}{+}6\text{A} \tag{5.40}$$

$$\frac{\partial u_i}{\partial t} \mapsto 114\text{M} + 110\text{A} \tag{5.41}$$

Total FLOPS required for second order upwind flux finite volume system on hexahedral mesh maps to 114 multiplications and 110 additions.

5.4.4 Second Order Upwind Flux FVTD on Tetrahedral Mesh

Obtaining gradient information for second order methods on tetrahedral mesh is not localized as on hexahedral mesh. In other words, the gradient in cell i may not be dependent on barycenter field values of immediate neighbors, say $j1$, $j2$, $j3$, and $j4$ but on distant neighbors n_1, n_2, n_3 and n_4. These neighbors can be picked up using the geometric properties of the mesh [76]. Omitting the details of the derivation, the net outgoing flux through each face k, χ^+_{ki}, belonging to cell i can be written as:

$$\chi^+_{ki}\Big|_{k=1}^{4} = \begin{pmatrix} \varphi^+_{ki}a_{ki} & \varphi^+_{ki}b_{ki} & \varphi^+_{ki}c_{ki} & \varphi^+_{ki}d_{ki} & \varphi^+_{ki}e_{ki} \end{pmatrix} \cdot \left.\begin{pmatrix} u_i \\ u_{n1} \\ u_{n2} \\ u_{n3} \\ u_{n4} \end{pmatrix}\right|_{k=1}^{4} \tag{5.42}$$

where a_{ki}, b_{ki}, c_{ki}, d_{ki} and e_{ki} represent the weights. Note that weights are scalar quantities and can be neglected. One can write

$$\varphi^+_{ki} \cdot u_i = \begin{pmatrix} 1 & 1 & 1 & \cdot & 1 & 1 \\ 1 & 1 & 1 & 1 & \cdot & 1 \\ 1 & 1 & 1 & 1 & 1 & \cdot \\ \cdot & 1 & 1 & 1 & 1 & 1 \\ 1 & \cdot & 1 & 1 & 1 & 1 \\ 1 & 1 & \cdot & 1 & 1 & 1 \end{pmatrix} \cdot \begin{pmatrix} e_{xi} \\ e_{yi} \\ e_{zi} \\ h_{xi} \\ h_{yi} \\ h_{zi} \end{pmatrix} \mapsto 30\text{M} + 24\text{A} \tag{5.43}$$

Similar expressions for the rest of the terms in the above equations yields:

$$\chi^+_{ki}\Big|_{k=1}^{4} = \underbrace{\varphi^+_{ki}u_i}_{30\text{M}+24\text{A}} + \underbrace{\varphi^+_{ki}u_{n1}}_{30\text{M}+24\text{A}} + \underbrace{\varphi^+_{ki}u_{n2}}_{30\text{M}+24\text{A}} + \underbrace{\varphi^+_{ki}u_{n3}}_{30\text{M}+24\text{A}} + \underbrace{\varphi^+_{ki}u_{n4}}_{30\text{M}+24\text{A}} \tag{5.44}$$

$$\mapsto \begin{pmatrix} 1 \\ 1 \\ 1 \\ 1 \\ 1 \\ 1 \end{pmatrix} \underbrace{+}_{6\text{A}} \begin{pmatrix} 1 \\ 1 \\ 1 \\ 1 \\ 1 \\ 1 \end{pmatrix} \underbrace{+}_{6\text{A}} \begin{pmatrix} 1 \\ 1 \\ 1 \\ 1 \\ 1 \\ 1 \end{pmatrix} \underbrace{+}_{6\text{A}} \begin{pmatrix} 1 \\ 1 \\ 1 \\ 1 \\ 1 \\ 1 \end{pmatrix} \underbrace{+}_{6\text{A}} \begin{pmatrix} 1 \\ 1 \\ 1 \\ 1 \\ 1 \\ 1 \end{pmatrix} \tag{5.45}$$

$$\mapsto 5\,(30\text{M} + 24\text{A}) + 4\,(6\text{A}) \tag{5.46}$$

$$\mapsto 150\text{M} + 144\text{A} \tag{5.47}$$

Thus the number of FLOPS required for net outgoing flux through each face is 150 multiplications and 144 additions. The net incoming flux through face k of cell i, χ^-_{ki}, can be written as:

$$\chi^-_{ki}\Big|_{k=1}^{4} = \begin{pmatrix} \varphi^-_{ki}a_{ki} & \varphi^-_{ki}b_{ki} & \varphi^-_{ki}c_{ki} & \varphi^-_{ki}d_{ki} & \varphi^-_{ki}e_{ki} \end{pmatrix} \cdot \left.\begin{pmatrix} u_j \\ u_{t1} \\ u_{t2} \\ u_{t3} \\ u_{t4} \end{pmatrix}\right|_{k=1}^{k=4} \tag{5.48}$$

$$\mapsto 150\text{M} + 144\text{A} \tag{5.49}$$

In the above expression, $t1$, $t2$, $t3$, $t4$ denote the cells which contribute to the gradient in cell j. Observe that the same barycenter field values are used to obtain the net outgoing flux through each face though the weights are changing. This means that the corresponding operands can be summed up when setting up the system matrix. Keeping this in view, the semidiscrete formulation can be written as:

$$
\begin{aligned}
\frac{\partial u_i}{\partial t} &= \chi^{+}_{ki}\Big|_{k=1}^{4} + \chi^{-}_{ki}\Big|_{k=1}^{4} && (5.50)\\
&= \underbrace{\chi^{+}_{ki}\Big|_{k=1}^{4}}_{150\mathrm{M}+144\mathrm{A}} + \underbrace{\chi^{-}_{1i}}_{150\mathrm{M}+144\mathrm{A}} + \underbrace{\chi^{-}_{2i}}_{150\mathrm{M}+144\mathrm{A}} + \underbrace{\chi^{-}_{3i}}_{150\mathrm{M}+144\mathrm{A}} + \underbrace{\chi^{-}_{4i}}_{150\mathrm{M}+144\mathrm{A}} && (5.51)\\
&\mapsto \begin{pmatrix}1\\1\\1\\1\\1\\1\end{pmatrix} \underbrace{+}_{6\mathrm{A}} \begin{pmatrix}1\\1\\1\\1\\1\\1\end{pmatrix} \underbrace{+}_{6\mathrm{A}} \begin{pmatrix}1\\1\\1\\1\\1\\1\end{pmatrix} \underbrace{+}_{6\mathrm{A}} \begin{pmatrix}1\\1\\1\\1\\1\\1\end{pmatrix} \underbrace{+}_{6\mathrm{A}} \begin{pmatrix}1\\1\\1\\1\\1\\1\end{pmatrix} && (5.52)\\
&\mapsto 5\,(150\mathrm{M}+144\mathrm{A})+24\mathrm{A} && (5.53)\\
\frac{\partial u_i}{\partial t} &\mapsto 750\mathrm{M}+744\mathrm{A} && (5.54)
\end{aligned}
$$

Thus the number of flops required is 750 multiplications and 744 additions.

5.4.5 FIT TD on Hexahedral Mesh

The number of FLOPS for FIT TD in semidiscrete form on hexahedral mesh maps to 6 multiplications and 18 additions [12].

5.4.6 Comparison

The number of FLOPS required for various methods is mentioned in Figure 5.5. The FLOPS for central flux formulations are also furnished (keeping Section 2.5.2 in view) though they are not explicitly derived here. One can observe the huge number of FLOPS required for all finite volume methods, irrespective of the mesh and the order, when compared to FIT TD. Note that in all the second order formulations, the piecewise linear interpolation is achieved by means of the gradient calculated with barycenter field values (GCC).

All the FLOPS are furnished for semidiscrete formulations only as different time integrators can be chosen to turn these semidiscrete formulations into fully discrete systems, at least for FVTD formulations.

FVTD UF 11 HEX	↦	66 M + 60 A	↦	126
FVTD CF 11 HEX	↦	36 M + 30 A	↦	66
FVTD UF 11 TET	↦	150 M + 144 A	↦	294
FVTD CF 11 TET	↦	60 M + 54 A	↦	114
FVTD UF 22 GCC HEX	↦	114 M + 110 A	↦	224
FVTD CF 22 GCC HEX	↦	60 M + 56 A	↦	116
FVTD UF 22 GCC TET	↦	750 M + 744 A	↦	1494
FVTD CF 22 GCC TET	↦	300 M + 444 A	↦	744
FIT	↦	6 M + 18 A	↦	24

Figure 5.5: The number of floating point operations required for various finite volume semidiscrete formulations. Compared to FIT all the finite volume methods require a large number of FLOPS, irrespective of the mesh and the order.

6 Conclusions

Finite volume time domain semidiscrete formulation, discrete in the space and continuous in the time, is derived starting from the Maxwell's equations. This is used to explain variations in finite volume methods e.g., variations in spatial approximation and variations in the way fluxes (central and upwind) are calculated. The spatial approximation is achieved by piecewise constant interpolation (first order) and piecewise linear interpolation (second order), in which the calculation of gradient is mandatory. The variations in the way the gradient is calculated has great influence on the solution. In general the accuracy of gradient is higher using the hexahedral grid than the tetrahedral grid. The gradient calculated from cell center field values is sensitive to geometry and materials on the tetrahedral grid, whereas this is not true for hexahedral grid. On the other hand, the gradient obtained from face center field values is more sensitive on the hexahedral grid than on the tetrahedral grid. Keeping the complexity in view, the spatial approximations are restricted to first and second orders.

Several boundary conditions are explained, followed by exemplification of construction of the system matrix, the iteration matrix and the curl curl matrix for assorted finite volume methods. The eigenvalue distribution of the iteration matrix of a given finite volume time domain method foretells about the stability of the method for a given time step and time update scheme. Various time marching schemes in addition to Runge–Kutta 1 (first order) and Runge–Kutta 2 (second order) are examined for temporal approximation. It is found in practice that first order methods have at least one stable time marching scheme for both types of flux approximation, central flux and upwind flux, whereas this is not the case for second order finite volume methods. Second order central flux finite volume method is not stable for the time marching schemes (Runge–Kutta and Leap–Frog) under consideration, where as there are multiple time marching schemes that can be employed for second order upwind flux finite volume method. As the higher order methods induce more computational cost, only first and second order approximations in time are considered for investigation.

The eigenvalues of the curl curl matrix provide the information about eigenfrequencies and eigenvectors. The practical difficulties of using upwind flux finite volume methods as eigenmode solvers are illustrated. Extracting the scattering parameters is detailed, based on the inherent property of “flux separation” in upwind flux finite volume methods. The incoming and outgoing fluxes through a cell face are exploited for this purpose.

Any numerical method promises the convergence of the solutions towards the reference (analytical) solution as the grid is refined. This is examined for various finite volume time domain methods in different scenarios e.g., a computational domain with curved surface and a singularity in the field due to the geometry. A comparison is also made with the convergence of the solutions obtained from the finite integration technique and the finite element method.

The tractability of finite volume time domain methods to model real world applications is examined. The considered applications look simple but are deceptive in nature, as they have curved geometries or singularities or very high contrast of materials or all of the above. The scattering parameters obtained from finite volume time domain methods are bidden against that of the finite integration technique and the finite element method. In addition, the convergence of the scattering parameters is also observed using all the methods, for each application.

The span of solver development is furnished along with the various modules in the code and the program flow at the concurrent stage. Various implementation strategies are also depicted along with numerous libraries used for the development.

The number of floating point operations required for various finite volume methods are mentioned and a comparison is made with that of the finite integration technique.

Thus, various finite volume time domain methods are investigated, on hexahedral and tetrahedral grids. Keeping the accuracy, complexity, computational cost and convergence in view, one can say that the urn tilts towards the non–dissipative methods based on Cartesian grid.

Appendix 1: Finite Volume Matrices

This appendix furnishes various finite volume matrices in the same order as they are encountered in Chapter 2.

$$A(\vec{n}) = \begin{pmatrix} 0 & 0 & 0 & 0 & +n_z/\varepsilon & -n_y/\varepsilon \\ 0 & 0 & 0 & -n_z/\varepsilon & 0 & +n_x/\varepsilon \\ 0 & 0 & 0 & +n_y/\varepsilon & -n_x/\varepsilon & 0 \\ 0 & -n_z/\mu & +n_y/\mu & 0 & 0 & 0 \\ +n_z/\mu & 0 & -n_x/\mu & 0 & 0 & 0 \\ -n_y/\mu & +n_x/\mu & 0 & 0 & 0 & 0 \end{pmatrix} \tag{A1.1}$$

$$\Lambda = \begin{pmatrix} 0 & 0 & 0 & 0 & 0 & 0 \\ 0 & 0 & 0 & 0 & 0 & 0 \\ 0 & 0 & +\upsilon & 0 & 0 & 0 \\ 0 & 0 & 0 & +\upsilon & 0 & 0 \\ 0 & 0 & 0 & 0 & -\upsilon & 0 \\ 0 & 0 & 0 & 0 & 0 & -\upsilon \end{pmatrix} \tag{A1.2}$$

$$p = \begin{pmatrix} n_x & 0 & n_x n_z\Big/(\upsilon\varepsilon) & -n_x n_y\Big/(\upsilon\varepsilon) & -n_x n_z\Big/(\upsilon\varepsilon) & n_x n_y\Big/(\upsilon\varepsilon) \\ n_y & 0 & n_y n_z\Big/(\upsilon\varepsilon) & \left(n_x^2 + n_z^2\right)\Big/(\upsilon\varepsilon) & -n_y n_z\Big/(\upsilon\varepsilon) & -\left(n_x^2 + n_z^2\right)\Big/(\upsilon\varepsilon) \\ n_z & 0 & -\left(n_x^2 + n_y^2\right)\Big/(\upsilon\varepsilon) & -n_y n_z\Big/(\upsilon\varepsilon) & \left(n_x^2 + n_y^2\right)\Big/(\upsilon\varepsilon) & n_y n_z\Big/(\upsilon\varepsilon) \\ 0 & n_x & -n_y & -n_z & -n_y & -n_z \\ 0 & n_y & n_x & 0 & n_x & 0 \\ 0 & n_z & 0 & n_x & 0 & n_x \end{pmatrix} \tag{A1.3}$$

$$A^{+}(\vec{n}) = \frac{1}{2} \begin{pmatrix} a_{11} & a_{12} & a_{13} & 0 & +n_z/\varepsilon & -n_y/\varepsilon \\ a_{21} & a_{22} & a_{23} & -n_z/\varepsilon & 0 & +n_x/\varepsilon \\ a_{31} & a_{32} & a_{33} & +n_y/\varepsilon & -n_x/\varepsilon & 0 \\ 0 & -n_z/\mu & +n_y/\mu & a_{11} & a_{12} & a_{13} \\ +n_z/\mu & 0 & -n_x/\mu & a_{21} & a_{22} & a_{23} \\ -n_y/\mu & +n_x/\mu & 0 & a_{31} & a_{32} & a_{33} \end{pmatrix} \tag{A1.4}$$

$$a_{11} = \left(n_y^2 + n_z^2\right)\upsilon \tag{A1.5}$$

$$a_{12} = -n_x n_y \upsilon \tag{A1.6}$$

$$a_{13} = -n_x n_z \upsilon \tag{A1.7}$$

$$a_{21} = -n_x n_y \upsilon \tag{A1.8}$$

$$a_{22} = \left(n_z^2 + n_x^2\right)\upsilon \tag{A1.9}$$

$$a_{23} = -n_y n_z \upsilon \tag{A1.10}$$

$$a_{31} = -n_x n_z \upsilon \tag{A1.11}$$

$$a_{32} = -n_y n_z \upsilon \tag{A1.12}$$

$$a_{33} = \left(n_x^2 + n_y^2\right)\upsilon \tag{A1.13}$$

$$\alpha_i = \begin{pmatrix} \varepsilon_i & 0 & 0 & 0 & 0 & 0 \\ 0 & \varepsilon_i & 0 & 0 & 0 & 0 \\ 0 & 0 & \varepsilon_i & 0 & 0 & 0 \\ 0 & 0 & 0 & \mu_i & 0 & 0 \\ 0 & 0 & 0 & 0 & \mu_i & 0 \\ 0 & 0 & 0 & 0 & 0 & \mu_i \end{pmatrix} \tag{A1.14}$$

$$t_{ki} = \begin{pmatrix} \frac{2Z_i}{\eta_i+\eta_j} & 0 & 0 & 0 & 0 & 0 \\ 0 & \frac{2Z_i}{\eta_i+\eta_j} & 0 & 0 & 0 & 0 \\ 0 & 0 & \frac{2Z_i}{\eta_i+\eta_j} & 0 & 0 & 0 \\ 0 & 0 & 0 & \frac{2Y_i}{y_i+y_j} & 0 & 0 \\ 0 & 0 & 0 & 0 & \frac{2Y_i}{y_i+y_j} & 0 \\ 0 & 0 & 0 & 0 & 0 & \frac{2Y_i}{y_i+y_j} \end{pmatrix} \tag{A1.15}$$

$$t_{\mathrm{PEC}} = \begin{pmatrix} 2 & 0 & 0 & 0 & 0 & 0 \\ 0 & 2 & 0 & 0 & 0 & 0 \\ 0 & 0 & 2 & 0 & 0 & 0 \\ 0 & 0 & 0 & 0 & 0 & 0 \\ 0 & 0 & 0 & 0 & 0 & 0 \\ 0 & 0 & 0 & 0 & 0 & 0 \end{pmatrix} \tag{A1.16}$$

$$t_{\mathrm{PMC}} = \begin{pmatrix} 0 & 0 & 0 & 0 & 0 & 0 \\ 0 & 0 & 0 & 0 & 0 & 0 \\ 0 & 0 & 0 & 0 & 0 & 0 \\ 0 & 0 & 0 & 2 & 0 & 0 \\ 0 & 0 & 0 & 0 & 2 & 0 \\ 0 & 0 & 0 & 0 & 0 & 2 \end{pmatrix} \tag{A1.17}$$

$$t_{\mathrm{Open}} = \begin{pmatrix} 1 & 0 & 0 & 0 & 0 & 0 \\ 0 & 1 & 0 & 0 & 0 & 0 \\ 0 & 0 & 1 & 0 & 0 & 0 \\ 0 & 0 & 0 & 1 & 0 & 0 \\ 0 & 0 & 0 & 0 & 1 & 0 \\ 0 & 0 & 0 & 0 & 0 & 1 \end{pmatrix} \tag{A1.18}$$

Appendix 2: Iteration Matrices

By applying the time marching schemes mentioned in Section 2.3.3, the solution to generalized finite volume system mentioned in Equation 2.76 can be written as:

$$u^{n+1} = u^n + (\Delta t) \sum_{i=1}^{s} b_i k_i \tag{A2.1}$$

where the coefficients b_i are mentioned in Section 2.3.3 and k_i are as follows:

$$\begin{aligned}
k_1 &= Au^n && \text{(A2.2)}\\
k_2 &= A\left(u^n + (\Delta t) a_{21} k_1\right) && \text{(A2.3)}\\
&= \left(A + (\Delta t) a_{21} A^2\right) u^n && \text{(A2.4)}\\
k_3 &= A\left(u^n + (\Delta t) a_{31} k_1 + (\Delta t) a_{32} k_2\right) && \text{(A2.5)}\\
&= \left(A + (\Delta t) a_{31} A^2 + (\Delta t) a_{32} A^2 + (\Delta t)^2 a_{32} a_{21} A^3\right) u^n && \text{(A2.6)}\\
k_4 &= A\left(u^n + (\Delta t) a_{41} k_1 + (\Delta t) a_{42} k_2 + (\Delta t) a_{43} k_3\right) && \text{(A2.7)}\\
&= \left(\begin{array}{l} A + (\Delta t) a_{41} A^2 + (\Delta t) a_{42} A^2 + (\Delta t) a_{43} A^2 + (\Delta t)^2 a_{42} a_{21} A^3 + \\ (\Delta t)^2 a_{43} a_{31} A^3 + (\Delta t)^2 a_{43} a_{32} A^3 + (\Delta t)^3 a_{43} a_{32} a_{21} A^4 \end{array} \right) u^n && \text{(A2.8)}
\end{aligned}$$

For various time marching schemes, e.g., Runge–Kutta 1, Runge–Kutta 2, Equation A2.1 takes various forms as shown below.

A2.1 Runge–Kutta 1

$$\begin{aligned}
u^{n+1} &= u^n + (\Delta t)\left(b_1 k_1\right) && \text{(A2.9)}\\
&= u^n + (\Delta t)(Au^n) && \text{(A2.10)}\\
&= \left[I + (\Delta t) A\right] u^n && \text{(A2.11)}
\end{aligned}$$

A2.2 Runge–Kutta 2

$$\begin{aligned}
u^{n+1} &= u^n + (\Delta t)\left(b_1 k_1 + b_2 k_2\right) && \text{(A2.12)}\\
&= u^n + (\Delta t)\left(A + (\Delta t) a_{21} A^2\right) u^n && \text{(A2.13)}\\
&= \left[I + (\Delta t)\left(A + \frac{(\Delta t)}{2} A^2\right)\right] u^n && \text{(A2.14)}
\end{aligned}$$

A2.3 Runge–Kutta 3

$$\begin{aligned}
u^{n+1} &= u^n + (\Delta t)\left(b_1 k_1 + b_2 k_2 + b_3 k_3\right) && \text{(A2.15)}\\
&= u^n + (\Delta t)\left(\frac{1}{6} k_1 + \frac{4}{6} k_2\right) && \text{(A2.16)}\\
&= \left[I + (\Delta t)\left(A + \frac{(\Delta t)}{2} A^2 + \frac{(\Delta t)^2}{6} A^3 + \frac{(\Delta t)^3}{12} A^4\right)\right] u^n && \text{(A2.17)}
\end{aligned}$$

A2.4 Runge–Kutta 4

$$\begin{aligned}
u^{n+1} &= u^n + (\Delta t)\left(b_1 k_1 + b_2 k_2 + b_3 k_3 + b_4 k_4\right) && \text{(A2.18)}\\
&= u^n + (\Delta t)\left(\frac{1}{6} k_1 + \frac{2}{6} k_2 + \frac{2}{6} k_3 + \frac{1}{6} k_4\right) && \text{(A2.19)}
\end{aligned}$$

$$= \left[I + (\Delta t) \left(A + \frac{(\Delta t)}{2} A^2 + \frac{(\Delta t)^2}{6} A^3 + \frac{(\Delta t)^3}{24} A^4 \right) \right] u^n \tag{A2.20}$$

A2.5 Heun 3

$$u^{n+1} = u^n + (\Delta t) \left(b_1 k_1 + b_2 k_2 + b_3 k_3 \right) \tag{A2.21}$$

$$= u^n + (\Delta t) \left(\frac{1}{4} k_1 + \frac{3}{4} k_3 \right) \tag{A2.22}$$

$$= \left[I + (\Delta t) \left(A + \frac{(\Delta t)}{2} A^2 + \frac{(\Delta t)^2}{6} A^3 \right) \right] u^n \tag{A2.23}$$

A2.6 Leap Frog

$$u^{n+1} = \left[I + \frac{1}{2} (\Delta t)^2 A^2 \pm \sqrt{\left(1 + \frac{1}{2} (\Delta t)^2 A^2 \right)^2 - 1} \right] u^n \tag{A2.24}$$

Appendix 3: Parametric Description of the Coaxial Connector

This appendix furnishes parametric description of the coaxial connector mentioned in Section 4.4.

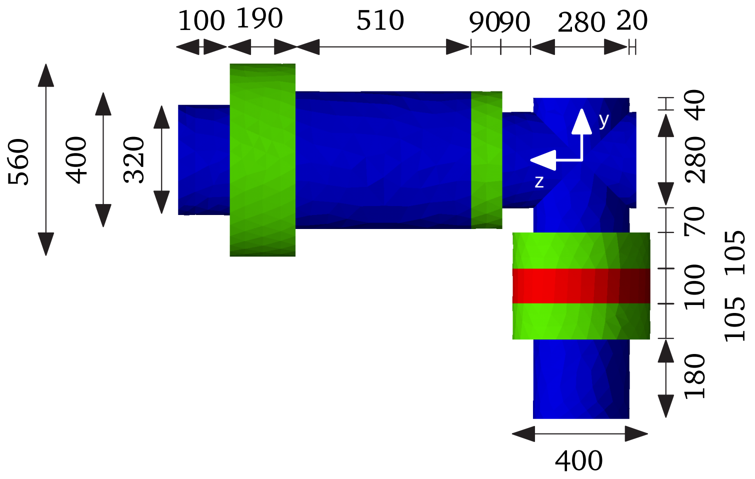

(a) The Coaxial connector observed from $+x$ direction.

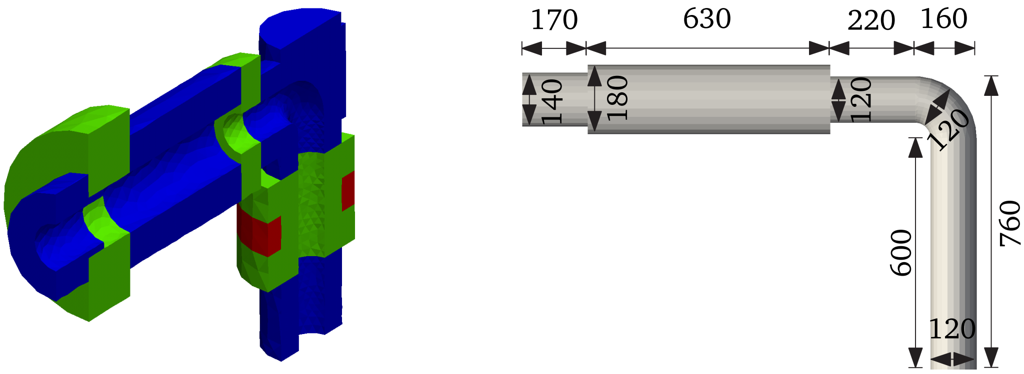

(b) Sliced at the center along the yz plane. The groove for the inner conductor is visible.

(c) Perfect electric conductor observed from $+x$ direction. This conductor fits in the groove visible in the left figure.

Figure A3.1: Parametric description of the coaxial connector.

Bibliography

[1] O. C. Zienkiewicz, A. K. Bahrani, and P. L. Arlett, "Numerical solution of 3-dimensional field problems," *Proc. IEE (London)*, vol. 115, pp. 367–369, Feb. 1968. (Cited on page 11.)

[2] K. S. Yee, "Numerical solution of initial boundary value problems involving Maxwell's equations in isotropic media," *IEEE Transactions on Antennas and Propagation*, vol. 14, no. 3, pp. 302–307, Mar. 1966. (Cited on page 11.)

[3] T. Weiland, "A discretization method for the solution of Maxwell's equations for six-component fields," *Electronics and Communication*, vol. 31, no. 3, pp. 116–120, 1977. (Cited on pages 11 and 37.)

[4] P. Silvester, "High-order finite element waveguide analysis (program descriptions)," *IEEE Transactions on Microwave Theory and Techniques*, vol. 17, no. 8, pp. 651–652, Aug. 1969. (Cited on page 11.)

[5] B. H. McDonald and A. Wexler, "Finite-element solution of unbounded field problems," *IEEE Transactions on Microwave Theory and Techniques*, vol. 20, no. 12, pp. 841–847, Dec. 1972. (Cited on page 11.)

[6] S. M. Rao, *Time Domain Electromagnetics*. Academic Press, 1999. (Cited on pages 11, 15, 16, 20, 24 and 34.)

[7] M. Dohlus, "Ein Beitrag zur numerischen Berechnung elecktromagnetischer Felder im Zeitbereich," Ph.D. dissertation, Technische Universität Darmstadt, Darmstadt, 1992. (Cited on page 11.)

[8] M. Dehler, "Numerische Lösung der Maxwellschen Gleichungen auf kreizylindrischen Gittern," Ph.D. dissertation, Technische Universität Darmstadt, Darmstadt, 1993. (Cited on page 11.)

[9] D. Schmitt, "Zur numerischen Berechnung von Resonatoren und Wellenleitern," Ph.D. dissertation, Technische Universität Darmstadt, Darmstadt, 1994. (Cited on page 11.)

[10] R. Marklein, "Numerische Verfahren zur Modellierung von akustischen, elektromagnetischen, elastischen und piezoelektrischen Wellenausbreitungsproblemen im Zeitbereich basierend auf der Finiten Integrationstechnik," Ph.D. dissertation, Universität Gesamthochschule Kassel, Kassel, 1997. (Cited on page 11.)

[11] R. Schuhmann, "Die Nichtorthogonale Finite-Integrations-Methode zur Simulation elektromagnetischer Felder," Ph.D. dissertation, Technische Universität Darmstadt, Darmstadt, 1999. (Cited on page 11.)

[12] M. Clemens and T. Weiland, "Discrete electromagnetism with the finite integration technique," *Progress in Electromagnetic Research (PIER) Monograph Series SPECial Issue on*. (Cited on pages 11 and 89.)

[13] L. Codecasa, V. Minerva, and M. Politi, "Use of barycentric dual grids for the solution of frequency domain problems by FIT," *IEEE Trans. Magn.*, vol. 40, pp. 1414–1419, Mar. 2004. (Cited on page 11.)

[14] L. Codecasa and M. Politi, "Explicit, consistent, and conditionally stable extension of FD-TD to tetrahedral grids by FIT," *IEEE Trans. Magn.*, vol. 44, no. 6, pp. 1258–1261, Jun. 2008. (Cited on page 11.)

[15] A. Taflove and S. Hagness, *Computational Electrodynamics: The Finite-Difference Time-Domain Method, Second Edition*. Artech House, 1995. (Cited on page 11.)

[16] A. Taflove, *Advances in Computational Electrodynamics: The Finite-Difference Time-Domain Method*. Artech House, 1998. (Cited on pages 11 and 12.)

[17] W. H. Reed and T. R. Hill, “Triangular mesh methods for the neutron transport equation,” Los Alamos Scientific Laboratory, Tech. Rep. LA–UR–73–479, 1973. (Cited on page 11.)

[18] V. Shankar and W. F. Hall, “A time domain differential solver for electromagnetic scattering,” in *URSI Meeting*, University of Colorado, Boulder, U.S.A., Jan. 1988. (Cited on page 11.)

[19] B. T. Nguyen, “Investigation of Three-Level Finite-Difference Time-Domain Methods for Multidimensional Acoustics and Electromagnetics,” Ph.D. dissertation, University of Michigan, Ann Arbor, 1996. (Cited on page 11.)

[20] V. Shankar, W. F. Hall, and A. Mohammadian, “A time-domain differential solver for electromagnetic scattering problems,” *Proceedings of the IEEE*, vol. 77, no. 5, pp. 709–721, 1989. (Cited on page 11.)

[21] V. Shankar, W. Hall, and A. H. Mohammadian, “A three-dimensional Maxwell’s equation solver for computation of scattering from layered media,” *IEEE Trans. Magn.*, vol. 25, no. 4, pp. 3098–3103, Jul. 1989. (Cited on page 11.)

[22] V. Shankar, W. F. Hall, and A. H. Mohammadian, “Development of computational fluid dynamics (CFD) based time-domain algorithms for Maxwell’s equations,” in *Antennas and Propagation Society International Symposium, 1990. AP-S. ’Merging Technologies for the 90’s’. Digest.*, Dallas, TX, May 7–11, 1990, pp. 1632–1635. (Cited on page 11.)

[23] A. H. Mohammadian, V. Shankar, and W. F. Hall, “Application of time-domain finite-volume method to antenna and array problems,” in *Antennas and Propagation Society International Symposium, 1990. AP-S. ’Merging Technologies for the 90’s’. Digest.*, Dallas, TX, May 7–11, 1990, pp. 997–1000. (Cited on page 11.)

[24] ——, “Application of time-domain finite-volume method to some radiation problems in two and three dimensions,” *IEEE Trans. Magn.*, vol. 27, no. 5, pp. 3841–3844, Sep. 1991. (Cited on pages 11 and 18.)

[25] P. Bonnet, X. Ferrieres, J. Grando, and J. C. Alliot, “FVTD applied to dielectric or wire structures,” in *Antennas and Propagation Society International Symposium, 1996. AP-S. Digest*, vol. 3, Baltimore, MD, Jul. 21–26, 1996, pp. 2126–2129. (Cited on page 11.)

[26] M. A. Jensen and Y. R. Samii, “Finite-difference and finite-volume time-domain techniques: Comparison and hybridization,” in *Antennas and Propagation Society International Symposium, 1996. AP-S. Digest*, vol. 1, Baltimore, MD, Jul. 21–26, 1996, pp. 108–111. (Cited on page 11.)

[27] P. Bonnet, X. Ferrieres, F. Paladian, J. Grando, J. C. Alliot, and J. Fontaine, “Electromagnetic wave diffraction using a finite volume method,” *Electronics Letters*, vol. 33, pp. 31–32, Jan. 2, 1997. (Cited on page 11.)

[28] C. Fumeaux, D. Baumann, P. Leuchtmann, and R. Vahldieck, “A generalized local time-step scheme for the FVTD method for efficient simulation of microwave antennas,” in *Microwave Conference, 2003. 33rd European*, vol. 1, Oct. 7–9, 2003, pp. 467–470. (Cited on page 12.)

[29] ——, “A generalized local time-step scheme for efficient FVTD simulations in strongly inhomogeneous meshes,” *IEEE Trans. Microwave Theory Tech.*, vol. 52, no. 3, pp. 1067–1076, Mar. 2004. (Cited on page 12.)

[30] D. Baumann, “A 3-D Numerical Field Solver Based On The Finite-Volume Time-Domain Method,” Ph.D. dissertation, ETH Zurich, Zurich, 2006. (Cited on page 12.)

[31] D. Baumann, C. Fumeaux, P. Leuchtmann, and R. Vahldieck, “Finite-volume time-domain (FVTD) method and its application to the analysis of hemispherical dielectric-resonator antennas,” *2003 IEEE MTT-S International Microwave Symposium Digest*, vol. 2, pp. 985–988, Jun. 8–13, 2003. (Cited on page 12.)

[32] C. Fumeaux, D. Baumann, and R. Vahldieck, “FVTD simulations of archimedean spiral antennas on thin substrates in planar and conformal configurations,” in *Wireless Communications and Applied Computational Electromagnetics, 2005. IEEE/ACES International Conference on*, Apr. 3–7, 2005, pp. 277–280. (Cited on page 12.)

[33] ——, “Finite-volume time-domain analysis of a cavity-backed archimedean spiral antenna,” *IEEE Trans. Antennas Propagat.*, vol. 54, no. 3, pp. 844–851, Mar. 2006. (Cited on page 12.)

[34] K. Sankaran, C. Fumeaux, and R. Vahldieck, “Uniaxial and radial anisotropy models for finite-volume maxwellian absorber,” *IEEE Trans. Microwave Theory Tech.*, vol. 54, pp. 4297–4304, Dec. 2006. (Cited on page 12.)

[35] ——, “Cell-centered finite-volume-based perfectly matched layer for time-domain maxwell system,” *IEEE Trans. Microwave Theory Tech.*, vol. 54, no. 3, pp. 1269–1276, Mar. 2006. (Cited on page 12.)

[36] ——, “Finite-volume maxwellian absorber on unstructured grid,” in *Microwave Symposium Digest, 2006. IEEE MTT-S International*, San Francisco, CA, Jun. 11–16, 2006, pp. 169–172. (Cited on page 12.)

[37] ——, “Hybrid pml-abc truncation techniques for finite-volume time-domain simulations,” in *Microwave Conference, 2006. APMC 2006. Asia-Pacific*, Yokohama, Dec. 12–15, 2006, pp. 949–952. (Cited on page 12.)

[38] ——, “Split and unsplit finite-volume absorbers: Formulation and performance comparison,” in *Microwave Conference, 2006. 36th European*, Manchester, Sep. 10–15, 2006, pp. 17–20. (Cited on page 12.)

[39] ——, “An investigation of the accuracy of finite-volume radial domain truncation technique,” in *Computational Electromagnetics in Time-Domain, 2007. CEM-TD 2007. Workshop on*, Perugia, Oct. 15–17, 2007, pp. 1–4. (Cited on page 12.)

[40] ——, “Radial absorbers for conformal time-domain methods: A solution to corner problems in mesh truncation,” in *Microwave Symposium, 2007. IEEE/MTT-S International*, Honolulu, HI, Jun. 3–8, 2007, pp. 709–712. (Cited on page 12.)

[41] K. Sankaran, “Accurate Domain Truncation Techniques for Time-Domain Conformal Methods,” Ph.D. dissertation, ETH Zurich, Zurich, 2007. (Cited on pages 12 and 25.)

[42] K. Krohne, D. Baumann, C. Fumeaux, and R. Vahldieck, “Reduced order finite volume models,” in *Microwave Conference, 2004. 34th European*, vol. 2, Oct. 13, 2004, pp. 581–584. (Cited on page 12.)

[43] K. Krohne, D. Baumann, and R. Vahldieck, “A state-space formulation for field-averaging finite-volume models,” in *Electromagnetic Compatibility, 2006. EMC-Zurich 2006. 17th International Zurich Symposium on*, Singapore, Feb. 27–Mar. 2006, 2006, pp. 22–25. (Cited on page 12.)

[44] ——, “Model order reduction for a field averaging finite-volume scheme,” in *Microwave Symposium Digest, 2006. IEEE MTT-S International*, San Francisco, CA, Jun. 11–16, 2006, pp. 60–63. (Cited on page 12.)

[45] K. Krohne, R. Vahldieck, and E. P. Li, “A non-disjoint hexahedral space discretization for the finite-volume technique,” in *Microwave Symposium, 2007. IEEE/MTT-S International*, Honolulu, HI, Jun. 3–8, 2007, pp. 281–284. (Cited on page 12.)

[46] K. Krohne, D. Baumann, C. Fumeaux, E.-P. Li, and R. Vahldieck, “Frequency-domain finite-volume simulations,” in *Microwave Conference, 2007. European*, Munich, Oct. 9–12, 2007, pp. 158–161. (Cited on page 12.)

[47] K. Krohne, “Order Reduction of Finite-Volume Models and Its Application to Microwave Device Optimization,” Ph.D. dissertation, ETH Zurich, Zurich, 2007. (Cited on pages 12 and 17.)

[48] C.-D. Munz, R. Schneider, and U. Voss, “A finite-volume method for the Maxwell equations in the time domain,” in *SIAM J. Sci. Comput*, Feb. 2000, pp. 449–475. (Cited on pages 12, 18 and 37.)

[49] C.-D. Munz, P. Ommes, and R. Schneider, “A three-dimensional finite-volume solver for the Maxwell equations with divergence cleaning on unstructured meshes,” in *Computer Physics Commications*, Jul. 2000, pp. 83–117. (Cited on pages 12, 18 and 37.)

[50] C.-D. Munz, F. Kemm, R. Schneider, and E. Sonnendrücker, “Divergence corrections in the numerical simulation of electromagnetic wave propagation,” in *8th International Conference on Hyperbolic Problems*, Magdeburg, 2000. (Cited on pages 12 and 37.)

[51] T. Weiland, M. Timm, and I. Munteanu, “A practical guide to 3-d simulation,” *IEEE Microwave*, vol. 9, no. 6, pp. 62–75, Dec. 2008. (Cited on page 12.)

[52] J. D. Jackson, *Classical Electrodynamics, Third Edition*. Wiley, 1998. (Cited on page 13.)

[53] N. Ida, *Engineering Electromagnetics, Second Edition*. Springer, 2004. (Cited on pages 13, 47 and 59.)

[54] E. J. Rothwell and M. J. Cloud, *Electromagnetics*. CRC Press, 2001. (Cited on page 14.)

[55] M. Remaki, “A new finite volume scheme for solving Maxwell’s system,” in *COMPEL*, 2000, pp. 913–931. (Cited on pages 17 and 18.)

[56] E. Stein, R. de Borst, and T. J. Hughes, *Encyclopedia of Computational Mechanics*. Wiley, 2004. (Cited on pages 18 and 37.)

[57] E. Gjonaj, *Lectures on computational electromagnetics*. TEMF, Technische Universität Darmstadt. (Cited on page 19.)

[58] E. Hairer, S. P. Norsett, and G. Wanner, *Solving Ordinary Differential Equations I, Second Edition*. Springer, 1993. (Cited on page 21.)

[59] E. Hairer and G. Wanner, *Solving Ordinary Differential Equations II, Second Edition*. Springer, 1996. (Cited on page 21.)

[60] E. Hairer, C. Lubich, and G. Wanner, *Geometric Numerical Integration, Second Edition*. Springer, 2006. (Cited on page 21.)

[61] J.-P. Berenger, “A perfectly matched layer for the absorption of electromagnetic waves,” *Journal of Computational Physics*, vol. 114, no. 2, pp. 185–200, 1994. (Cited on page 25.)

[62] J.-P. Bérenger, “Perfectly matched layer for the FDTD solution of wave-structure interaction problems,” *IEEE Transactions on Antennas and Propagation*, vol. 44, no. 1, pp. 110–117, Jan. 1996. (Cited on page 25.)

[63] ——, “A perfectly matched layer for free-space simulations in finite-difference computer codes,” *Annales des Télécommunications*, vol. 51, no. 1–2, pp. 39–46, 1996. (Cited on page 25.)

[64] J.-P. Berenger, “Three-dimensional perfectly matched layer for the absorption of electromagnetic waves,” *Journal of Computational Physics*, vol. 127, pp. 363–379, 1996. (Cited on page 25.)

[65] J.-P. Bérenger, “Improved PML for the FDTD solution of wave-structure interaction problems,” *IEEE Transactions on Antennas and Propagation*, vol. 45, no. 3, pp. 466–473, Mar. 1997. (Cited on page 25.)

[66] J.-P. Berenger, “Numerical reflection of evanescent waves from perfectly matched layers,” in *IEEE Antennas and Propagat. Soc. Int. Symp.*, vol. 3, Montréal, Canada, Jul. 1997, pp. 1888–1891. (Cited on page 25.)

[67] J.-P. Bérenger, “An effective PML for the absorption of evanescent waves in waveguides,” *IEEE Microwave Guided Wave Letters*, vol. 8, no. 5, pp. 188–190, May 1998. (Cited on page 25.)

[68] ——, “Evanescent waves in PML’s: Origin of the numerical reflection in wave-structure interaction problems,” *IEEE Transactions on Antennas and Propagation*, vol. 47, no. 10, pp. 1497–1503, Oct. 1999. (Cited on page 25.)

[69] J.-P. Berenger, “Numerical reflection of evanescent waves by PMLs: Origin and interpretation in the FDTD case. Expected consequences to other finite methods,” *International Journal of Numerical Modelling: Electronic Networks, Devices and Field*, vol. 13, no. 2–3, pp. 103–114, Mar.–Jun. 2000. (Cited on page 25.)

[70] J.-P. Bérenger, “Numerical reflection from FDTD-PMLs: A comparison of the split PML with the unsplit and CFS PML,” *IEEE Transactions on Antennas and Propagation*, vol. 50, no. 3, pp. 258–265, Mar. 2002. (Cited on page 25.)

[71] ——, “On the reflection from Cummer’s nearly perfectly matched layer,” *IEEE Microwave and Wireless Components Letters*, vol. 14, no. 7, pp. 334–336, Jul. 2004. (Cited on page 25.)

[72] S. Abarbanel and D. Gottlieb, “A mathematical analysis of the PML method,” *Journal of Computational Physics*, vol. 134, pp. 357–363, 1997. (Cited on page 25.)

[73] D. S. Katz, E. T. Thiele, and A. Taflove, “Validation and extension to three dimensions of the Berenger PML absorbing boundary condition for FD-TD meshes,” *IEEE Microwave Guided Wave Letters*, vol. 4, no. 8, pp. 268–270, Aug. 1994. (Cited on page 25.)

[74] Y. C. Lau, M. S. Leong, and P. S. Kooi, “Extension of Berenger’s PML boundary condition in matching lossy medium and evanescent waves,” *Electronics Letters*, vol. 32, no. 11, pp. 974–976, 1996. (Cited on page 25.)

[75] G. Lazzi and O. P. Gandhi, “On the optimal design of the PML absorbing boundary condition for the FDTD code,” *IEEE Transactions on Antennas and Propagation*, vol. 45, no. 5, pp. 914–916, May 1997. (Cited on page 25.)

[76] W. Ackermann, *Private communication*. TEMF, Technische Universität Darmstadt. (Cited on pages 31 and 88.)

[77] R. Courant, K. Friedrichs, and H. Lewy, “Über die partiellen Differenzengleichungen der mathematischen Physik,” *Mathematische Annalen*, vol. 100, no. 1, pp. 32–74, 1928. (Cited on page 34.)

[78] ——, “On the partial difference equations of mathematical physics,” *IBM Journal*, pp. 215–234, Mar. 1967. (Cited on page 34.)

[79] R. J. Leveque, *Finite Volume Methods for Hyperbolic Problems*. Cambridge University Press, 2002. (Cited on pages 34 and 37.)

[80] T. Weiland, “A numerical method for the solution of the eigenwave problem of longitudinally homogeneous waveguides,” *Electronics and Communication*, vol. 31, no. 7, pp. 308–314, 1977. (Cited on page 37.)

[81] ——, “Zur numerischen lösung des eigenwellenproblems längshomogener wellenleiter beliebiger randkontur und transversal inhomogener materialbelegung,” Ph.D. dissertation, Technische Universität Darmstadt, 1977. (Cited on page 37.)

[82] B. Cockburn, G. E. Karniadakis, and C.-W. Shu, *Discontinuous Galerkin Methods: Theory, Computation and Applications*. Springer, 2000. (Cited on page 37.)

[83] D. M. Pozar, *Microwave Engineering, Third Edition*. Wiley, 2004. (Cited on page 39.)

[84] J. Choma and W.-K. Chen, *Feedback Networks: Theory and Circuit Applications*. World Scientific, 2007. (Cited on page 39.)

[85] *S-Parameter Design – Application Note AN 154*. Agilent Technologies, 2006. (Cited on page 39.)

[86] M. Dohlus and T. Weiland, “Die gitter-Maxwell gleichungen für offene strukturen,” in *ITG-Fachbericht 111: Antennen, Vorträge der ITG-Fachtagung 20.-23.3.1990 in Wiesbaden*, Mar. 1990, pp. 19–24. (Cited on page 40.)

[87] M. Dehler, M. Dohlus, and T. Weiland, “Calculation of frequency domain parameters by time domain methods,” *IEEE Transactions on Magnetics*, vol. 28, no. 2, pp. 1797–1800, Mar. 1992. (Cited on page 40.)

[88] ——, “Calculating frequency-domain data by time-domain methods,” *International Journal of Numerical Modelling: Electronic Networks, Devices and Fields*, vol. 6, no. 1, pp. 19–27, Feb. 1993. (Cited on page 40.)

[89] M. Dohlus, P. Thoma, and T. Weiland, “Broadband simulation of open waveguide boundaries within large frequency ranges,” in *Proceedings of the 2nd International Workshop on Discrete Time Domain Modelling of Electromagnetic Fields and Networks*, 1993, pp. 1–8. (Cited on page 40.)

[90] B. Geib, M. Dohlus, and T. Weiland, “Calculation of scattering parameters by orthogonal expansion and finite integration method,” *International Journal of Numerical Modelling: Electronic Networks, Devices and Fields*, vol. 7, pp. 377–398, 1994. (Cited on page 40.)

[91] H. Wolter, M. Dohlus, and T. Weiland, “Broadband calculation of scattering parameters in the time domain,” *IEEE Transactions on Magnetics*, vol. 30, no. 5, pp. 3164–3167, Sep. 1994. (Cited on page 40.)

[92] M. Dohlus, P. Thoma, and T. Weiland, “Stability of finite difference time domain methods related to space and time discretization,” *IEEE Transactions on Microwave Theory and Techniques*, 1995. (Cited on page 40.)

[93] M. Dohlus, R. Schuhmann, and T. Weiland, “Calculation of frequency domain parameters using 3D eigensolutions,” *International Journal of Numerical Modelling: Electronic Networks, Devices and Fields*, vol. 12, no. 2, pp. 41–68, 1999. (Cited on page 40.)

[94] E. Gjonaj, *Private communication*. TEMF, Technische Universität Darmstadt. (Cited on page 41.)

[95] K. Zhang and D. Li, *Electromagnetic Theory for Microwaves and Optoelectronics*. Springer, 2008. (Cited on pages 65 and 75.)

[96] [Online]. Available: http://www.mathworks.com (Cited on page 79.)

[97] [Online]. Available: http://msdn.microsoft.com (Cited on page 79.)

[98] [Online]. Available: http://www.paraview.org (Cited on page 79.)

[99] [Online]. Available: http://www.cst.com (Cited on page 79.)

[100] [Online]. Available: http://www.dplot.com (Cited on page 79.)

[101] [Online]. Available: http://www.hpfem.jku.at/netgen (Cited on page 80.)

[102] [Online]. Available: http://www-c.inria.fr/gamma (Cited on page 80.)

[103] [Online]. Available: http://www.gnu.org/software/gsl (Cited on page 81.)

[104] [Online]. Available: http://software.intel.com/en-us/intel-mkl (Cited on page 81.)

[105] [Online]. Available: http://glaros.dtc.umn.edu (Cited on page 81.)

Acronyms

ABC	Absorbing Boundary Condition(s)
CF	Central Flux
CPW	Cells Per Wavelength
DGFEM	Discontinuous Galerkin Finite Element Method
FD	Frequency Domain
FDTD	Finite Difference Time Domain
FEM	Finite Element Method
FIT	Finite Integration Technique
FVFD	Finite Volume Frequency Domain
FVTD	Finite Volume Time Domain
PBA	Perfect Boundary Approximation
PEC	Perfect Electric Conductor
PMC	Perfect Magnetic Conductor
TD	Time Domain
UF	Upwind Flux
e.g.	Exempli Gratia, For Example
i.e.	Id Est, That Is

L.H.S	Left Hand Side
R.H.S	Right Hand Side

1D	One Dimension(al)
2D	Two Dimensions(al)
3D	Three Dimensions(al)

Continuous Field Theory

$\vec{B}$	Magnetic flux density
$\vec{D}$	Electric flux density
$\vec{E}$	Electric field strength
$\vec{H}$	Magnetic field strength
$\vec{J}$	Electric current density
$\vec{M}$	Magnetization
$\vec{P}$	Polarization
ε	Permittivity
μ	Permeability
ρ	Electric charge density

E_0	Amplitude of electric field strength
H_0	Amplitude of magnetic field strength
$\vec{E}_a$	Electric field pattern of mode a
$\vec{E}_b$	Electric field pattern of mode b
U	Column vector with concatenated electric and magnetic field strength magnitudes

$\mathrm{d}S$	Differential surface
S	Surface
$\mathrm{d}V$	Differential volume
V	Volume

Discrete Field Theory

f_{ki}	k^{th} face belonging to i^{th} cell
m_i	Number of faces of i^{th} cell
$\vec{n}_{ki}$	Outward unit normal of k^{th} face belonging to i^{th} cell
s_{ki}	Area of k^{th} face belonging to i^{th} cell
u_i	Field values at center of i^{th} cell
u_{ki}	Field values at center of k^{th} face belonging to i^{th} cell
$u_{ki}^{\pm}$	Outside and inside field values at center of k^{th} face belonging to i^{th} cell
v_i	Volume of i^{th} cell

n_g	Number of neighbors considered to construct the gradient
x_i	x coordinate of barycenter of i^{th} cell
y_i	y coordinate of barycenter of i^{th} cell
z_i	z coordinate of barycenter of i^{th} cell
x_{ki}	x coordinate of center of k^{th} face of i^{th} cell
y_{ki}	y coordinate of center of k^{th} face of i^{th} cell
z_{ki}	z coordinate of center of k^{th} face of i^{th} cell

ε_i	Permittivity of material in i^{th} cell
μ_i	Permeability of material in i^{th} cell
υ_i	Velocity of electromagnetic wave in i^{th} cell
η_i	Impedance in i^{th} cell
y_i	Admittance in i^{th} cell

α_i	Material matrix of i^{th} cell
t_{ki}	Transmission matrix of k^{th} face of i^{th} cell
$A^{+}\left(\vec{n}_{ki}\right)$	Matrix with outgoing flux related mesh information of k^{th} face of i^{th} cell
$A^{-}\left(-\vec{n}_{ki}\right)$	Matrix with incoming flux related mesh information of k^{th} face of i^{th} cell

$\varphi_{ki}^{\pm}$	Coefficient matrices for outgoing and incoming fluxes through k^{th} face belonging to i^{th} cell
$\phi_i^{\pm}$	Outgoing and incoming fluxes in i^{th} cell

A	System matrix
A^{+}	System matrix with outgoing flux related mesh information
A^{-}	System matrix with incoming flux related mesh information
Δt	Timestep
G	Iteration matrix
I	Identity matrix
A_{cc}	Curl curl matrix

List of Figures

Publications

1 C. Bommaraju and R. Marklein, “Optimally accurate second-order time-domain finite-difference scheme for acoustic, electromagnetic, and elastodynamic wave modeling: one-dimensional case,” in *Antennas and Propagation Society International Symposium, 2004. IEEE*, Jun. 2004, pp. 1499–1502.

2 R. Marklein and C. Bommaraju, “Optimally accurate second-order time-domain finite-difference scheme for electromagnetic wave modeling: two-dimensional case,” in *Antennas and Propagation Society International Symposium, 2005. IEEE*, Jun. 2005, pp. 166–169.

3 C. Bommaraju, R. Schuhmann, and T. Weiland, “A novel low-dispersive (2,2) finite difference method,” in *Computational Electromagnetics in Time-Domain, 2005. CEM-TD 2005. Workshop on*, Sep. 2005, pp. 20–23.

4 C. Bommaraju, R. Marklein, W. Ackermann, R. Schuhmann, and T. Weiland, “A novel low-dispersive collocated FDTD method: 3-d case,” in *Antennas and Propagation Society International Symposium 2006, IEEE*, Jul. 2006, pp. 3789–3792.

5 C. Bommaraju, R. Marklein, R. Schuhmann, and T. Weiland, “A novel low-dispersive (2,2) collocated FDTD scheme,” *International Journal of Numerical Modelling: Electronic Networks, Devices and Fields*, vol. 20, pp. 17–33, Nov. 2006.

6 C. Bommaraju and R. Marklein, “A novel low-dispersive (2,2) finite difference method: 3-d case,” in *Computational Electromagnetics in Time-Domain, 2007. CEM-TD 2007. Workshop on*, Oct. 2007, pp. 1–4.

7 C. Bommaraju, W. Ackermann, and T. Weiland, “Finite volume time domain method on TET & HEX meshes,” in *Computational Electromagnetics in Time-Domain, 2007. CEM-TD 2007. Workshop on*, Oct. 2007, pp. 10–14.

Curriculum Vitae

Chakrapani Bommaraju
Born 30 August 1980 in Machilipatnam, India

1985–1990	Primary School Saint Francis School, Machilipatnam, India
1990–1995	Secondary School Annie Besant Sisuvidya Mandiram, Machilipatnam, India
1995–1997	Intermediate Noble College, Machilipatnam, India
1997–2001	Bachelor of Technology Electronics and Communication Engineering Nagarjuna University, India
2002–2004	Master of Science Electrical Communication Engineering Universität Kassel, Germany
2004–2009	Doctor of Engineering Electrical Engineering and Information Technology Technische Universität Darmstadt, Germany